INFRARED SPECTROELECTROCHEMICAL STUDIES OF REDOX-ACTIVE SELF ASSEMBLED MONOLAYERS: STRUCTURE AND KINETICS

A dissertation submitted to the
College of Graduate and Postdoctoral Studies
in partial fulfillment of the requirements
for the degree of Doctor of Philosophy
in the Department of Department of Chemistry
University of Saskatchewan
Saskatoon

By
Bipinlal Unni

©Bipinlal Unni, February 2023. All rights reserved.
Unless otherwise noted, copyright of the material in this thesis belongs to the author.

Permission to Use

In presenting this dissertation in partial fulfillment of the requirements for a Postgraduate degree from the University of Saskatchewan, I agree that the Libraries of this University may make it freely available for inspection. I further agree that permission for copying of this dissertation in any manner, in whole or in part, for scholarly purposes may be granted by the professor or professors who supervised my dissertation work or, in their absence, by the Head of the Department or the Dean of the College in which my dissertation work was done. It is understood that any copying or publication or use of this dissertation or parts thereof for financial gain shall not be allowed without my written permission. It is also understood that due recognition shall be given to me and to the University of Saskatchewan in any scholarly use which may be made of any material in my dissertation.

Disclaimer

Reference in this dissertation to any specific commercial products, process, or service by trade name, trademark, manufacturer, or otherwise, does not constitute or imply its endorsement, recommendation, or favoring by the University of Saskatchewan. The views and opinions of the author expressed herein do not state or reflect those of the University of Saskatchewan, and shall not be used for advertising or product endorsement purposes.

Requests for permission to copy or to make other uses of materials in this dissertation in whole or part should be addressed to:

Head of the Department of Chemistry
170 Thorvaldson Building
110 Science Place
University of Saskatchewan
Saskatoon, Saskatchewan
Canada
S7N 5C9

OR

Dean
College of Graduate and Postdoctoral Studies
University of Saskatchewan
116 Thorvaldson Building, 110 Science Place
Saskatoon, Saskatchewan S7N 5C9 Canada

Abstract

Long-range bridge-mediated electron transfer proceeding through outer-sphere pathways attracts scientific interest beyond fundamental studies due to its relevance in technological systems like molecular electronics and biosensors. Deep knowledge of the structure and dynamics of these molecular interfaces and the kinetics of the electron transfer processes are critical to improving the performance of such technological systems. Interfacial charge transfer between the electrode and redox molecules can be manipulated as an outer-sphere electron transfer process by employing organic molecules as bridging moieties between the electron donor and acceptor. Electrode surfaces can be made suitable for charge transfer studies via the self assembled monolayers (SAMs) of redox-substituted alkanethiols. Alternatively, redox species can be covalently tethered to the terminals of preformed monolayers of alkane chains. Electroactive surfaces prepared via both methodologies are explored for studying heterogeneous electron transfer (ET) processes using conventional electrochemical techniques such as cyclic voltammetry and chronocoulometry. Butler-Volmer (BV) formalism and Marcus-Hush-Chidsey (MHC) theory are some of the widely accepted models to predict the kinetic parameters of electron transfer processes. In-situ surface characterization techniques such as surface-enhanced infrared absorption spectroscopy (SEIRAS) offer the potential to provide deeper insights into molecular processes occurring in organized systems during electron transfer. Time-resolved SEIRAS technique is an advanced method capable of correlating structural changes in both the redox-active moiety and the scaffold supporting the redox centre preceding/during/following the electron transfer process. This thesis reports a combination of time-resolved SEIRAS with conventional electrochemistry techniques to study the electron transfer process across different electroactive layers. The time-resolved SEIRAS technique is applied here to follow the molecular restructuring of alkane-bridging moieties during the electron transfer process in ferrocene-SAM systems. The behaviour of surrounding SAM structures to the redox moieties during the electron transfer process is also explored using deuterated alkanethiols as diluents. An amide-coupling reaction is explored to link electroactive moieties to prefabricated alkanethiol SAM terminals. Studying the reaction mechanism of the amide-coupling process offers an opportunity to improve the reaction efficiency. Therefore, the potential of electrochemical-SEIRAS has been leveraged to monitor the amide-coupling process on the monolayers under various reaction conditions. SEIRAS analysis identified that the reaction intermediates change their rate of formation under the electrode potential control, which establishes proof for potential-dependent reaction pathways for amide-coupling reactions. Another redox species studied in this body of research is 2,2,6,6- tetramethylpiperidine-1-oxyl (TEMPȮ), a prominent organic free radical used as a catalyst in various industrial-scale processes. Electron transfer studies of TEMPȮ tethered to various lengths of alkanethiols are reported in this thesis using conventional electrochemical techniques. Time-resolved SEIRAS studies of TEMPȮ-alkanethiol monolayers for structural and kinetic analysis are reported here for the first time. The SEIRAS analysis provides a molecular model showing the conformational change of TEMPȮ moieties along with structural reorientation of the alkane chain adlayers during the electron transfer process.

Acknowledgements

I am sincerely grateful to my PhD supervisor, Dr. Ian J. Burgess, for his invaluable guidance, steadfast support, and insightful feedback throughout my research journey. His expertise and encouragement have been instrumental in shaping my ideas and refining my arguments, and I am deeply grateful for his mentorship.

I am much obliged to the external examiner, Dr. Julianne M. Gibbs from the University of Alberta, and the members of my academic committee, Dr. Robert W.J. Scott, Dr. Amy L. Stevens and Dr. Kenneth E. Wilson, for their valuable feedback, constructive criticism, and thoughtful suggestions, which have helped me improve the quality of my research and the clarity of my writing.

I am grateful to past and present members of the Burgess group and my colleagues in Environmental Material Science for their friendship, encouragement, and intellectual engagement. Their support and camaraderie have made the journey more enjoyable and rewarding. I thank the undergraduate lab managers, Dr. Alexandra Bartole-Scott, Dr. Valerie MacKenzie, Dr. Pia Wennek, and Dr. Adrian Clark, for their support and training. I want to acknowledge the staff and faculty at the Department of Chemistry, who have provided me with a stimulating and supportive academic environment. I have benefited from this institution's resources, facilities, and intellectual community, and I am grateful for the opportunities it has provided during my graduate studies. I extend my gratitude to the Tri-Counsil funding agencies, Mitacs, and EMS, for their financial support, which has enabled me to pursue my research interests and complete my PhD.

I am deeply indebted to the unwavering love, patience, and encouragement of my wife, Sumy Sasidharan, for successfully completing this thesis work. And, my words are not enough to thank our family and friends for their love and support. Their belief in me and my abilities has strengthened and inspired me throughout my PhD program.

Thank you all for your support and contributions to completing this thesis and being part of this academic journey.

This thesis is dedicated to my beloved parents, with gratitude that cannot be overstated.

Contents

Permission to Use . . . . **i**

Abstract . . . . **ii**

Acknowledgements . . . . **iii**

Contents . . . . **v**

List of Tables . . . . **vii**

List of Figures . . . . **viii**

List of Abbreviations . . . . **xi**

1 Introduction **1**
1.1 General overview 1
1.2 Motivation and Thesis Objectives 3
1.3 Scope of Thesis 4

2 Background **6**
2.1 Electron transfer theories 6
2.1.1 Macroscopic theories of electron transfer 6
2.1.2 Microscopic theories of electron transfer 10
2.2 Conclusion 17

3 Literature review on self assembled monolayers for electron transfer studies **19**
3.1 Introduction 19
3.2 Literature on the structural study of SAM 20
3.3 Literature on ET studies using redox-active SAM 24
3.4 Conclusion 27

4 Experimental methods and data analysis **29**
4.1 Electrochemical methods 29
4.1.1 Potential sweep method: Cyclic voltammetry 30
4.1.2 Current transient methods: Chronoamperometry and chronocoulometry 34
4.2 IR spectroelectrochemistry 36
4.2.1 Surface enhanced IR absorption spectroscopy (SEIRAS) 38
4.2.2 Time-resolved SEIRAS 41
4.3 Conclusion 44

5 IR spectroelectrochemical analysis of ferrocene terminated alkanethiol mixed monolayers 45
5.1 Introduction 45
5.2 Experimental 47
5.3 Results and discussion 48
5.3.1 Cyclic voltammetry of $FcC_{11}SH$ / $C_{10}SH$ mixed monolayers 48
5.3.2 SEIRAS of $FcC_{11}SH$ with $C_{10}D_{21}SH$ diluents 51
5.3.3 Time-resolved SEIRAS studies of the $FcC_{11}SH$ + $C_{10}SH$ mixed monolayers with different anions 56
5.3.4 Potential dependent SEIRAS study of amide coupled ferrocene-alkanethiol SAM . . . 59
5.4 Conclusion 61

6 Surface enhanced infrared adsorption studies of amide coupling reaction 63
6.1 Introduction 63
6.2 Experimental Section 65
6.3 Results and Discussion 66
6.3.1 Real time monitoring of EDC coupling reaction using ATR-SEIRAS 66
6.3.2 Potential dependence on EDC reaction kinetics 68
6.4 Conclusion 70

7 Electrochemical analysis of the TEMPȮ coupled alkanethiol monolayers 72
7.1 Introduction 72
7.2 Experimental details 75
7.3 Result and discussions 75
7.3.1 CV analysis of TEMPȮ coupled alkanethiol SAM 75
7.3.2 Laviron analysis of TEMPȮ coupled alkanethiol SAM 79
7.3.3 Chronocoulometric analysis of TEMPȮ coupled alkanethiol SAM 81
7.3.4 Tafel analysis and reorganization energy of TEMPȮ coupled alkanethiol SAM 86
7.4 Conclusion 87

8 IR spectroelectrochemical analysis of the TEMPȮ coupled alkanethiol monolayers . . 89
8.1 Introduction 89
8.2 Experimental details 90
8.3 Result and Discussion 90
8.3.1 IR spectral peak analysis of TEMPȮ and TEMPO$^+$ 90
8.3.2 ATR-SEIRAS of TEMPȮ coupled monolayer 93
8.3.3 Time-resolved ATR-SEIRAS 96
8.3.4 Conclusions 99

9 Conclusions and outlook 101
9.1 Introduction 101
9.2 Key findings of the thesis 101
9.3 Contributions to the scientific research 103
9.4 Limitations of the study 104
9.5 Future research 105

References 106

Appendix A Derivation of the peak potential of cyclic voltammogram 117

Appendix B Synthesis of TEMPO$^+$ 118

List of Tables

5.1 Data summarized from the CVs of the mixed monolayers of $FcC_{11}SH/C_{10}SH$ shown in the Figure 5.1 . . . 50
5.2 Apparent rate constants for the various peak evolution, obtained from the step scan data of $FcC_{11}SH$ mixed monolayers given in the Figures 5.7 and 5.8 . . . 59

7.1 Data summary of TEMPȮ SAM cyclic voltammograms measured at 2 mV/s . . . 77

List of Figures

2.1 Change in the energy barrier of heterogeneous ET process with respect to applied potentials. The dashed curve corresponds to $E = E^{0'}$ and the solid curve to $E > E^{0'}$, where the electrochemical potential of the electron is raised by the amount $F(E - E^{0'})$. 7

2.2 Variation of the oxidation and reduction rate constants with applied potentials as per Butler-Volmer model. Dotted and dashed lines shows the influence of α-value on the change in rate constants 9

2.3 Two intersecting parabolas representing the quadratic variation of Gibbs energy curves in the Marcus-Hush model, along the reaction coordinate (combination of vibrational and solvent coordinates) at (a) $E = E^0$ and (b) $E - E^0 \neq 0$. The intersection point between two parabolas is the transition state ($q^\ddagger$). 11

2.4 Variation of the transfer coefficient with applied potential according to the Marcus-Hush model. Gray solid lines in both figures correspond to values predicted by the Butler-Volmer model for α=0.5 13

2.5 Schematic representation of free energy surfaces in non-adiabatic electron transfer reactions for (a) isoenergetic reaction, (b) reaction condition for maximum rate constant, and (c) inversion region 14

2.6 Marcus-Hush-Chidsey model showing change in the reduction and oxidation rate constants with the applied electrode potentials. 15

3.1 Schematic representing the structure of a self assembled monolayer 19

4.1 Cyclic voltammetry overview (a) experimental setup for electrode potential control and current measurement, (b) figure representing electrochemical cell in terms of circuit elements when the system is at open circuit potential, and (c) cyclic voltammogram of a simple RC circuit. . . 30

4.2 Cyclic voltammogram of a redox system and the Randles equivalent circuit 32

4.3 (a) Schematic representation of double-step potential applied to the working electrode, and (b) the current transients recorded at various time increments. 34

4.4 (a) Schematic representation of Kretschmann configuration of ATR-IR spectroelectrochemical set-up, (b) the evanescent field confined to the electrode surface and (c) various orientations of dipoles and the induced mirror images on the metal substrate 38

4.5 (a) Schematic representation of the IR single beam intensity at the detector of FTIR spectrometer, for the reference and sample potentials, (b) the absorbance spectrum is generated from the reference and sample signals. Peak (i) results from a situation where the vibrational mode is active in the sample single beam spectrum and inactive/not present in the reference spectrum. Peak (ii) is for the opposite case. 41

4.6 Schematic diagram of a Michelson interferometer configuration for FTIR 42

4.7 Schematic representation of (a) rapid scan FT-IR and (b) step-scan FT-IR. These figures are adapted from the PhD thesis of Kaiyang Tu (1) 43

5.1 (a) Cyclic voltammograms of ferrocene SAMs on polycrystalline Au bead at a scan rate of 20 mV/s in 0.1 M $HClO_4$. Each cyclic voltammogram corresponds to the SAM layers prepared from different fractions of $FcC_{11}SH$ to $C_{10}SH$. The multiple peaks at anodic (A, A') and cathodic (C, C') scans are marked on individual cyclic voltammograms, (b) and (c) are the schematic representation of densely packed and isolated ferrocene units in the mixed monolayers of SAM, respectively 49

5.2 Potential dependent SEIRAS spectra of the mixed monolayers of $FcC_{11}SH$ and $C_{10}D_{21}SH$ (1:1 ratio), in 0.05 M $KClO_4$ electrolyte 51

5.3 Schematic representing the transition dipole moment (μ) of the CH stretching modes in the tilted and upright orientations of alkane chains 52

5.4 Comparison of the SEIRAS peak intensities and the CV of the corresponding SEIRAS layer with the (1:1) mixed monolayers of $FcC_{11}SH$ and $C_{10}D_{21}SH$. The distinct sharp feature of the CV indicates the quasi-crystallinity of the SEIRAS film 53
5.5 Predicted model showing various stages of molecular events during the oxidation of mixed monolayers of $FcC_{11}SH$. Process 1: conversion of ferrocene to ferrocenium ion (Fc^+) during the electron transfer, Process 2: ion pairing to stabilize the charged redox moiety and the ingress of water molecules towards the electrode interface, Process 3: reordering of the bridging units and adjacent diluents to an upright position, and Process 4: rotation of the ferrocenium moiety along Fc–C bond. Time-resolved EC-SEIRAS analysis is required to identify the sequence of these molecular processes 55
5.6 Comparison of the effect of ClO_4^- and NO_3^- as counter-ions on (a) the CVs and (b) the SEIRAS spectra of $FcC_{11}SH$ + $C_{10}SH$ mixed monolayer. The potential dependent SEIRAS spectra is collected between 0.05 V as base potential and 0.45 V for ClO_4^- (0.55 V for NO_3^-) 56
5.7 Time-resolved SEIRAS spectra (step scan) of the mixed monolayers of $FcC_{11}SH$ and $C_{10}SH$ (1:1 ratio), in 0.05 M $KClO_4$. Spectra are collected between 0.45 V (sample potential) and 0.05 V (base potential) 57
5.8 Time-resolved SEIRAS spectra (step scan) of the mixed monolayers of $FcC_{11}SH$ and $C_{10}SH$ (1:1 ratio), in 0.05 M KNO_3. Spectra are collected between 0.55 V (sample potential) and 0.05 V (base potential) 58
5.9 Schematic representation of covalent bonding of amino-substituted ferrocene to the COOH-terminals of preformed alkanethiol SAM, via amide-coupling reaction 60
5.10 (a) CV and (b) the potential dependent SEIRAS spectra of amide coupled ferrocene-$NHCO_2$ $C_{16}SH$ SAM on Au-ITO layer 61

6.1 Schematic representation of the activation of carboxylic acid by carbodiimide to form *O*-acylurea and (1) its reaction with NHS to yield NHS-ester, (b) formation of anhydride in the absence of NHS and (c) showing formation of *N*-acylurea via intramolecular acyl transfer (the reaction scheme is adapted from Reference(2)) 64
6.2 ATR-SEIRAS spectra of the EDC/NHS reaction on the MUA SAM modified Au surface . . . 67
6.3 Potential dependent ATR-SEIRAS spectra of EDC/NHS reaction collected at (a) 500 mV and (b) -300mV 68
6.4 Fitted exponential functions to the plots of band intensities at 1735 cm^{-1} as a function of time, collected at various applied potentials 69
6.5 Plot showing rate constant of 1735, 1780 and 1811 cm^{-1} peaks as a function of electrode potential. The error bars are obtained from the fitting function 70

7.1 Schematic representation of covalent bonding of amino-substituted $TEMP\dot{O}$ to the COOH-terminals of preformed alkanethiol SAM, via amide-coupling reaction, and the redox structure of $TEMP\dot{O}/TEMPO^+$ redox couple. Redox formal potential of $TEMP\dot{O}$ SAM is measured as ∼0.690 V vs Ag/AgCl in 0.05 M $KClO_4$ 73
7.2 Cyclic voltammograms at 2 mV/s for C_n-$TEMP\dot{O}$ monolayers derived from a) mercapto-hexanoic acid (C_6-$TEMP\dot{O}$, MHA), b) mercapotoctanoic acid (C_8-$TEMP\dot{O}$, MOA), c) mercaptoundecanoic acid (C_{11}-$TEMP\dot{O}$, MUA) and d) mercaptododecanoic acid (C_{12}-$TEMP\dot{O}$, MDDA) 76
7.3 The current transient of C_8-$TEMP\dot{O}$ SAM on a gold bead electrode 78
7.4 Cyclic voltammetry of C_{12}-$TEMP\dot{O}$ SAM on Au electrode at various scan rate 79
7.5 The plot showing Laviron analysis of C_{12}-$TEMP\dot{O}$ SAM on Au bead. 80
7.6 (a) Potential step sequence used in chronocoulometry experiments (b) Current transients collected at each potential steps (c) Plot of total measured charge obtained from integrating the current transients as a function of t_{var} (d) integrated and normalized charge transients for the same potential step for the C_8 $TEMP\dot{O}$ monolayer (red line) and MOA SAM (black line). . . 81
7.7 (a) Potential steps modified with intermediate step applied with variable time (b) Current transients collected at modified potential steps 83

7.8 (a) Plots of the natural logarithm of the fraction of TEMPO^+ remaining on a C_{11}-$\text{TEMP}\dot{\text{O}}$ modified gold bead electrode as a function of t_{var} for different step potentials near the formal potential (b) influence of the SAM chain length on the standard rate constant. Each point is the average of a minimum of four measurements on unique SAMs. 85
7.9 Tafel plots for C_{12}-$\text{TEMP}\dot{\text{O}}$ (open black circles) and C_{16}-$\text{TEMP}\dot{\text{O}}$ (solid red circles) on a gold bead electrode. Blue lines are calculated Tafel plots assuming a reorganization energy (from bottom to top) of 0.9 eV, 1.0 eV and 1.1 eV 86

8.1 IR transmittance spectra of $\text{TEMP}\dot{\text{O}}$ and TEMPO^+ 91
8.2 Potential dependant SEIRA spectra of $\text{TEMP}\dot{\text{O}}$ coupled C_{12}-SAM with respect to the reference spectra collected at $E = +0.4$ V; inset showing the cyclic voltammetry of $\text{TEMP}\dot{\text{O}}$-$C_{12}$-SAM modified SEIRA film in the spectroelectrochemical cell. 93
8.3 Proposed redox-induced conformational change in $\text{TEMP}\dot{\text{O}}$ SAMs 95
8.4 Tafel plot showing normalized rate constants of the anodic and cathodic branches of $\text{TEMP}\dot{\text{O}}$-$C_{12}$-alkane thiol SAM redox system 95
8.5 (a) Time-resolved ATR-SEIRAS spectra of $\text{TEMP}\dot{\text{O}}$ coupled to C_{12}-alkane thiol SAM on Au-ITO measured using rapid scan method, collected from +0.40 V (base potential) to 0.69 V vs Ag/AgCl (formal potential of $\text{TEMP}\dot{\text{O}}/\text{TEMPO}^+$) (b) and (c) are the relative signal intensity plotted as a function of time at 1100 and 1624 cm^{-1}, respectively. The red trace shows the exponential fit to the data 97
8.6 The current transients on semi-logarithmic scale, measured for $\text{TEMP}\dot{\text{O}}$ C_{12}-alkane thiol SAM on Au bead (red trace) and on Au islands electrodeposited on ITO as SEIRAS substrate (black trace) 98

B.1 UV spectra of oxidation of $\text{TEMP}\dot{\text{O}}$ using hypohalous acids (HOCl) 118

List of Abbreviations

ATR	Attenuated total reflectance
BV	Butler-Volmer
CV	Cyclic voltammetry
CA	Chronoampherometry
CC	Chronocoulometry
$C_{10}SH$	Decanethiol
$C_{10}D_{21}SH$	Deuteriated decanethiol
CMO	Conductive metal oxide
Cp	Cyclopendadieneyl
DL	Double-layer
EC	Electrochemical
EDC	N -ethyl-N -(3-(dimethylamino)propyl)carbodiimide
ET	Electron transfer
Fc	Ferrocene
$FcC_{11}SH$	Ferrocene substituted undencanethiol
FDS	Fast double-step
FTIR	Fourier transformed infrared
IRE	Internal reflection element
ITO	Indium tin oxide
IZO	Indium zinc oxide
LB	Langmuir-Blodgett
MDDA	2-mercaptododecanoic acid
MHA	6-mercaptohexanoic acid
MHC	Marcus-Hush-Chidsey
MHDA	6-mercaptohexadecanoic acid
MUA	11-mercaptoundecanoic acid
MOP	4-methoxy pyridine
NHS	N-hydroxysuccinimide
OCP	Open circuit potential
SAM	Self assembled monolayer
SEC	Spectroelectrochemistry
SEIRAS	Surface enhanced infrared absorption spectroscopy
SPP	Surface plasmon polaritons

TEMPȮ	2,2,6,6-Tetramethyl-1-piperidinyloxy, free radical
TR	Time-resolved

1 Introduction

1.1 General overview

Heterogeneous electron transfer (ET) is a complex phenomenon subject to intense computational and experimental studies due to its role in fundamental biological processes and many modern technological applications such as energy conversion and storage, molecular electronics and biosensors.(3) To achieve a well-controlled and efficient ET process, it is an absolute requirement to elucidate the mechanism and the kinetic parameters associated with ET reactions. ET theories were formulated based on classical and quantum mechanical approaches and experimentally verified using conventional electrochemical methods.(4; 5) ET theories highlight that the electron donor and acceptor moieties undergo molecular rearrangement to achieve favourable energy conditions during the charge transfer process. Conventional electrochemical techniques can provide an overall view of electrode reactions. However, they cannot gather direct evidence of the macromolecular rearrangement events at the electrode interface during, after, or before the ET processes. Consider, for example, the complexities associated with electron transfer in a redox-active protein molecule. Assuming the starting molecule is in sufficient proximity to undergo electron exchange with a second species or electrode surface with reasonable probability, we can describe the timescale of various components in the overall process. Molecular vibrations that give rise to fluctuations in the nuclear positions of the electron donor/acceptor sub-units and associated solvent molecules underpin the “reorganization”energy of the system and occur on the time scale of pico to femto seconds.(3) The actual ET, typically through tunneling mechanisms, is probabilistic in nature and highly dependent on the separation (distance) between the donor/acceptor and the electronic environment connecting the two centres. This provides a means to manipulate systems and throttle the apparent rate of ET into experimentally convenient regimes. In organized systems, or complex macro-molecules such as redox-active proteins, there are additional processes that are affected by the ET event. For example, a change in redox state of a metal centre in a heme complex undoubtedly can lead to tertiary structural change in the protein.(6) Macromolecular changes and/or multimolecular relaxations are inherently slower than vibrational fluctuations of discrete, small molecules. However, on a larger time scale, the sequence of the elementary steps (ion-pairing, counter-ion ingress/egress, tertiary structural change) is often ignored or considered auxiliary to ET studies.

Coupling electrochemical systems with spectroscopy techniques are beneficial to examine interfacial processes such as redox reactions, molecular adsorption/desorption, molecular reorientation and heterogeneous charge transfer, occurring under the potential control. Spectroscopic methods such as ultraviolet-visible

(UV-Vis), infrared (IR), Raman, fluorescence, X-ray absorption and nuclear magnetic resonance (NMR) spectroscopy have been coupled with electrochemical systems to monitor electrode reactions, and such interdisciplinary techniques are classified as spectroelectrochemistry(SEC). Zhai et al.(7) published a comprehensive review of recent developments in the field of SEC. Vibrational SEC is a very powerful tool because following the vibrational transitions of adsorbed species at the electrode surface, particularly in the fingerprint region, enables the identification of electrochemical reaction intermediates and products. Interrogation of the spectral shifts and change in the peak widths can provide insights into the local interactions, such as hydrogen bonding and reorientation of the solvent molecules caused by electrode processes. Therefore, SEC methods with vibrational spectroscopies, especially Raman and mid-IR has the advantage over other spectroscopic techniques. Vibrational SEC has undergone major developments in the last few decades.(8) For example, Raman spectroscopy was initially considered as too insensitive for monitoring electrochemical processes because only a very small fraction of the incident photons are involved in inelastic scattering. However, the electronic structure of metals used as electrode materials facilitates efficient resonant excitation of surface plasmons upon incidence with light at proper wavelengths. This results in enhanced electromagnetic fields around the metal surface, which boosts the Raman scattering intensity by a factor of 10^4 to 10^{14}.(9) The electrochemical surface enhanced Raman spectroscopy (EC-SERS) was first reported for pyridine molecules electrochemically adsorbed on a rough silver surface.(10). Unfortunately, the interpretation of SERS spectra is complicated and quantitative assessment of electrochemical processes is not trivial.(9)

The concept of local electromagnetic field enhancement through the excitation of localized surface plasmon polaritons (LSPP) along the rough metal films has been extended to infrared spectroscopy, which led to the development of surface enhanced infrared absorption spectroscopy (SEIRAS).(11; 12; 13) Adsorbed molecules with an oscillating dipole alters the polarizability of the metal substrate by inducing a mirror dipole. This results in the change in absorption of the metal film at the molecular vibrational frequencies of the adsorbates. The surface enhancement factor depends on the size and shape of the metal substrate. Although the highest reported surface enhancement factor of SEIRAS (10^2 to 10^3) is much lower than that of SERS, higher IR absorption cross-sections of surface adsorbed molecules results in significant and well-detectable spectral features.(14) Moreover, SEIRAS spectral interpretation is relatively straightforward compared to SERS. As per the SEIRAS surface selection rule, those vibrational bands arising from a change in the dipole moment parallel to the surface normal are enhanced in SEIRAS spectrum. Thus, the surface orientation of adsorbed molecules can be interpreted based on the relative intensities between bands of orthogonal dipole moment vectors.(15) Efficient plasmonic coupling between the incident light and the SPP of metal surface requires specific optical set-up such as Kretchmann (attenuated total reflectance (ATR)) and Otto configuration.(16; 17). Fortunately, the above optical set-up for the SEIRAS has also been apt for electrochemical (EC) measurement, in which ATR configuration is preferred for EC-SEIRAS to avoid interference from IR absorption of solvent molecules. Interfacial water molecules play a key role in the aqueous-phase electrochemical process. EC-SEIRAS is an excellent tool to interpret the potential dependent orientation of water molecules at the electrode surface.(18; 19; 20; 21) Site-specific information can be obtained from SEIRAS spectra by assessing the vibrational frequency shift in the structural functionalities like O–H, N–H, C=O and C=N, that are involved in local interactions such as hydrogen bonding.(22; 23) The surface sensitivity of SEIRAS enables functional studies of biomolecules which is essential for both technological applications and fundamental studies of proteins and biologically relevant compounds. The functionality of the electroactive biomolecules that are adsorbed on the substrate can be triggered by applying potentials. Therefore, the application of EC-SEIRAS has been gaining attention in bio-nanotechnology, as the construct of hybrid bio-devices involves the combination of biomolecules such as nucleic acids or proteins and a solid sensing substrate such as an electrode.(24) The adsorption of biomolecules on the surface-modified SEIRAS substrate is a suitable model for biomolecular interactions. A convenient approach for surface modification is self assembled monolayers (SAMs) of cross-linking units on the SEIRAS substrates. The cross-linking units generally comprise terminals like thiols to adsorb on the metal spontaneously, a spacer group of alkane chain and the headgroup targeted to bind with the biomolecules. Specific protein-protein and protein-ligand interactions can be mimicked at the electrode surface by choosing appropriate headgroups. For example, SAMs with a negatively charged carboxyl headgroup can specifically bind with positively charged amino acids, such as lysine and histidine, on the protein surface.(25; 26)

1.2 Motivation and Thesis Objectives

Potential modulation is a general approach to control electrode processes. Acquiring the vibrational spectra of electrochemically adsorbed species at a pace comparable to the rate of potential induced ET reaction enables one to extract the dynamic nature of transient electrochemical processes.(27; 28) Time-resolved EC-SEIRAS benefits from recent advances in instrumentation and data processing and can achieve time resolution as high as micro to milliseconds. Hence, it is possible to collect SEIRAS spectra corresponding to each electrochemical datum, which continuously follows the molecular changes at the electrode interface. This spectral data can be used to obtain kinetic information of the electrochemical process. The motivation for this PhD research work arose from the desire to use time-resolved EC-SEIRAS to address the kinetics and mechanism of molecular behaviour in organized systems during the ET process. In recent years, the Burgess group has developed the technical know-how to study fast electrode processes using surface enhanced IR spectroelectrochemistry with millisecond temporal resolution. In principle, surface modified Au electrodes with electroactive SAM can be adapted to study ET process using surface enhanced IR spectroelectrochemistry.

The main research objective of this PhD thesis is to exploit the surface-sensitivity of EC-SEIRAS to obtain direct structural information of the monolayers and draw conclusive evidence of the concomitant molecular events during the charge transfer process at the electrochemical interface. This thesis specifically investigates the ET process occurring in multiple redox systems such as ferrocene and nitroxyl free radical SAMs. The studies discussed in this thesis aim to provide a detailed electrochemical evaluation of the above-mentioned redox systems using cyclic voltammetry and double-step chronocoulometry. Furthermore, it also demonstrates the potential of time-resolved SEIRAS to obtain structural details on organized molecular systems that complement the electrochemical analyses of ET kinetics.

1.3 Scope of Thesis

After this brief introduction, chapters two, three, and four cover ET theory, the relevant literature, and the experimental methodologies used in the current studies. The second chapter provides a detailed overview of electron transfer formalism, including Butler-Volmer and Marcus-Hush-Chidsey theories. The third chapter covers literature on structural studies of SAMs and the prominent reports on ET studies using redox-active SAM. The fourth chapter provides a detailed explanation of the various electrochemical and spectroelectrochemical techniques used in this project. In addition, a description of the data acquisition and analysis methods to obtain the kinetic parameters are included.

The first part of Chapter 5 includes a brief literature review on the ET studies of ferrocene-terminated alkane SAM. This chapter also covers electrochemical studies of ferrocene amide-coupled to C_{16}- alkanethiol SAM. The later part of this chapter discusses ATR-SEIRAS studies of the same system, in which potential dependent static IR and rapid scan data are analyzed. The deuterated alkanethiols are used as diluents in the SEIRAS studies of ferrocene-SAM to differentiate the structural changes associated with the diluent alkane chains from the redox linkage units. The final part of this chapter presents CV and SEIRAS measurements of amide-coupled ferrocene to the acid terminals of alkanethiol SAMs to study the redox behaviour of isolated ferrocene moieties.

Chapter 6 explores the possibility of increasing the efficacy of the amide-coupling reaction between amine-substituents and the acid-terminal alkanethiol SAM. It provides details in the literature about the molecular steps involved in the amide coupling reaction. The results from the potential dependent SEIRAS spectra of the various steps involved in the amide-coupling reaction with acid-terminated alkanethiol SAM on Au layers are discussed.

The seventh and eighth chapters deal with the electrochemical and IR spectroelectrochemical analysis of $\text{TEMP}\dot{\text{O}}$-alkanethiol SAM systems. Chapter 7 starts with a literature review on electrochemical ET studies of alkane SAMs. Kinetic measurements using different electrochemical techniques, such as CV and chronocoulometry, are analyzed in detail. Chapter 8 covers the chemical oxidation of $\text{TEMP}\dot{\text{O}}$ to TEMPO^+ and its transmission IR measurement to identify the IR fingerprint bands. Then static ATR-SEIRAS studies of C_{12}-$\text{TEMP}\dot{\text{O}}$ SAM as a function of electrode potentials are elaborated upon. The kinetic parameters obtained from rapid scan analysis of C_{12}-$\text{TEMP}\dot{\text{O}}$ SAM are discussed in this chapter.

The final chapter provides an overall thesis summary based on the findings discussed in chapters five to eight. It includes how ET rates vary with alkane chain length, reorientation energy of redox moieties, and the molecular rearrangements associated with the transfer of electrons between electrode and redox molecules. This chapter intends to compare and contrast the conventional electrochemical methods with the IR spectroelectrochemical techniques based on the ET studies discussed in this thesis. Also, a discussion on how these findings contribute to the existing knowledge gap in this research area is included. This thesis concludes with a detailed note on future research based on the findings reported in this research.

2 Background

2.1 Electron transfer theories

Mechanistic understanding of electron transfer (ET) through organized molecular layers is the primary focus of this thesis. In that context, a background discussion about the theory of electron transfer theories is required. The ET process is ubiquitous in fundamental biological systems and advanced technological applications. An ET reaction can be described as an electron transfer from a donor to the acceptor, resulting in the generation of an electric current. The exchange of electrons between an electrode surface and a redox molecule at the electrochemical interface is called heterogeneous electron transfer. The ET process is generally classified as either an "inner-sphere" or an "outer-sphere" reaction. The earlier reaction involves ET via bond breaking and formation and, the reactant/intermediate/product strongly interacts with the electrode surface. Outer-sphere reaction denotes a process in which reactant/products maintain their original coordination sphere; hence no bond breaking/formation occurs.

2.1.1 Macroscopic theories of electron transfer

Under the classical treatment of an outer-sphere ET reaction between a metal electrode and a molecule in solution, the following reaction applies

$$Oxd + e^- \underset{k_{Red}}{\overset{k_{Oxd}}{\rightleftharpoons}} Red \tag{2.1}$$

where k_{Oxd} and k_{Red} are the heterogeneous rate constants of the oxidation and reduction half-reactions, respectively.

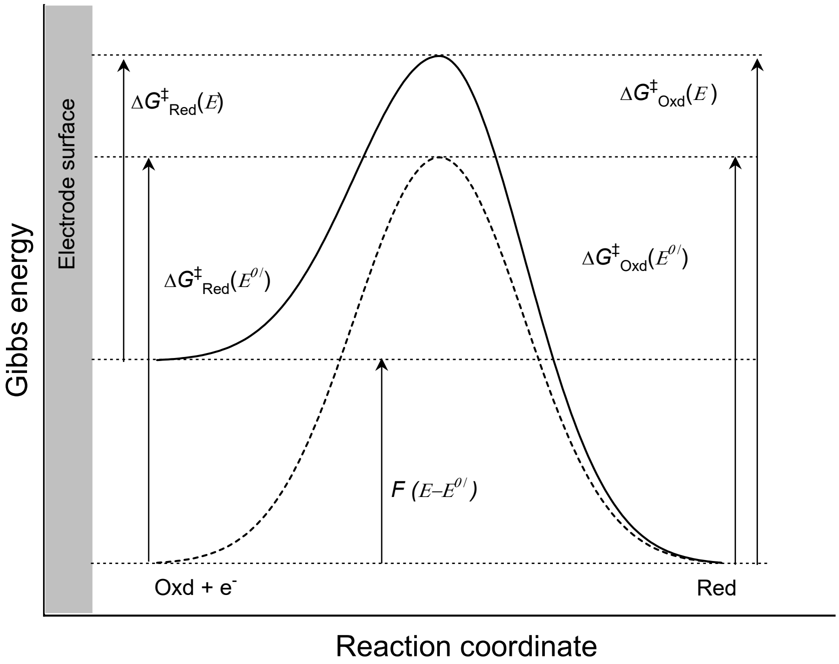
Gibbs energy
Electrode surface
$\Delta G^{\ddagger}_{\mathrm{Red}}(E)$
$\Delta G^{\ddagger}_{\mathrm{Oxd}}(E)$
$\Delta G^{\ddagger}_{\mathrm{Red}}(E^{0\prime})$
$\Delta G^{\ddagger}_{\mathrm{Oxd}}(E^{0\prime})$
$F\,(E\text{–}E^{0\prime})$
Oxd + e$^-$
Red
Reaction coordinate

Figure 2.1: Change in the energy barrier of heterogeneous ET process with respect to applied potentials. The dashed curve corresponds to $E = E^{0'}$ and the solid curve to $E > E^{0'}$, where the electrochemical potential of the electron is raised by the amount $F(E - E^{0'})$.

Since the anodic (oxidation) and cathodic (reduction) reactions follow first-order kinetics with respect to the surface concentration of adsorbed redox species,

$$\upsilon_{Red} = k_{Red} C^s_{Oxd}$$

$$\upsilon_{Oxd} = k_{Oxd} C^s_{Red}$$

and, the overall rate of the redox reaction, υ is the difference between rates of oxidation and reduction as shown below

$$\upsilon = k_{Oxd} C^s_{Red} - k_{Red} C^s_{Oxd} \tag{2.2}$$

where C^s_{Oxd}, C^s_{Red} are the surface concentrations of the oxidized and reduced species. The measured current density (j, the current i normalized by electrode area) is directly related to the overall rate of electrode reaction, therefore

$$j = F\upsilon = F\left(k_{Oxd} C^s_{Red} - k_{Red} C^s_{Oxd}\right) \tag{2.3}$$

In the classical treatment of ET processes, the above-mentioned rate constants can be expressed in Arrhenius form as,

$$k_{Oxd} = A \exp\left(\frac{-\Delta G^{\ddagger}_{Oxd}(E)}{RT}\right) \tag{2.4}$$

$$k_{Red} = A \exp\left(\frac{-\Delta G^{\ddagger}_{Red}(E)}{RT}\right) \tag{2.5}$$

in which $\Delta G^{\ddagger}_{Oxd}$ and $\Delta G^{\ddagger}_{Red}$ are the standard Gibbs energy of activation for oxidation and reduction, respectively.

The system reaches a new equilibrium upon change in the electrode potential by ΔE, such that the electron at the electrode surface experience a relative change in energy by $-F\Delta E = -F(E - E^{0'})$. Here, E and $E^{0'}$ are the applied and formal electrode potentials, respectively. The apparent change in the energy barrier for the oxidation half is a fraction $(1-\alpha)$ of the total energy change. The term α is called the transfer coefficient and its value lies between zero and one, depends on the symmetry of energy barrier. Thus,

$$\Delta G^{\ddagger}_{Oxd} = \Delta G^{\ddagger}_{Oxd}(E^{0'}) - (1-\alpha)F(E - E^{0'}) \tag{2.6}$$

The cathodic half has the complementary symmetry of energy barrier to that of anodic half reaction, therefore,

$$\Delta G^{\ddagger}_{Red} = \Delta G^{\ddagger}_{Red}(E^{0'}) + \alpha F(E - E^{0'}) \tag{2.7}$$

When the electrode potential $E = E^{0'}$, the above expression shows the Gibbs energy of activation for anodic and cathodic reactions are equivalent,

$$\Delta G^{\ddagger}_{Red}(E^{0'}) = \Delta G^{\ddagger}_{Oxd}(E^{0'}) = \Delta G^{\ddagger}(E^{0'}) \tag{2.8}$$

which indicates the oxidation and reduction curve becomes symmetrical as represented by the symmetric dotted curve in Figure 2.1 At this condition, the equations 2.4 and 2.5 can be compared as,

$$k_{Red}(E^{0'}) = k_{Oxd}(E^{0'}) = A\exp\left(\frac{-\Delta G^{\ddagger}(E^{0'})}{RT}\right) = k^{0} \tag{2.9}$$

where k^0 is called the standard heterogeneous rate constant, defined as the rate constant of a redox reaction at its formal potential. The value of k^0 determines the kinetic facility of a redox reaction, such that a system with large k^0 reaches equilibrium rapidly, whereas smaller k^0 indicates sluggish ET. The two major kinetic models developed for interfacial electron transfer is discussed in the following sections.

The Butler-Volmer model

Classical Butler-Volmer (BV) model is built on transition state theory, according to which the reactions proceed through a well-defined transition state or activated complex.(29)(30) By substituting the expression for Gibbs activation energies (equations 2.6 and 2.7) in equations 2.4 and 2.5, well-known expressions for the BV rate constants are obtained:

$$k^{BV}_{Red} = k^{0}\exp\left(-\frac{\alpha F(E - E^{0'})}{RT}\right) \tag{2.10}$$

$$k^{BV}_{Oxd} = k^{0}\exp\left(\frac{(1-\alpha)F(E - E^{0'})}{RT}\right) \tag{2.11}$$

The BV formalism predicts that the rate constant of an outer-sphere ET reaction increases without limit as an exponential function of $-\alpha(E - E^{0'})$ for reduction ($(1-\alpha)(E - E^{0'})$ for oxidation).(31) Replacing the rate

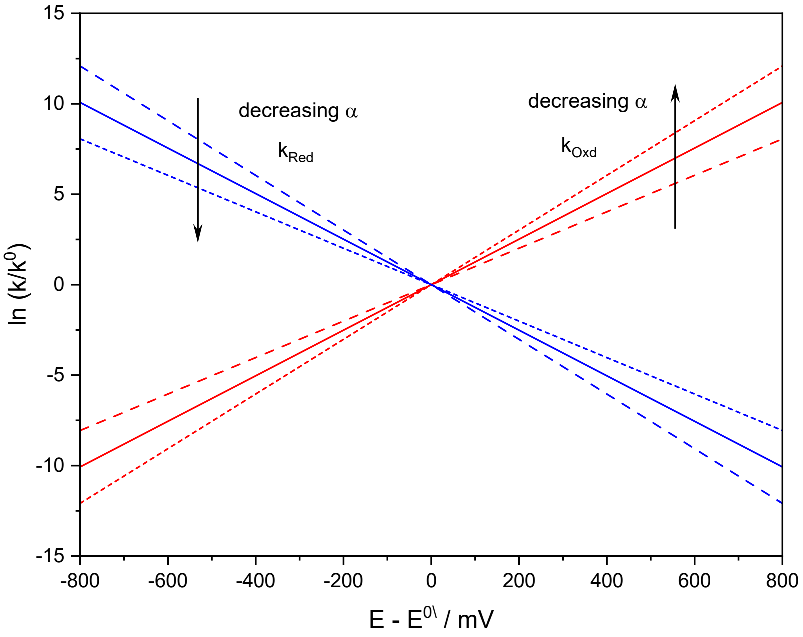

Figure 2.2: Variation of the oxidation and reduction rate constants with applied potentials as per Butler-Volmer model. Dotted and dashed lines shows the influence of α-value on the change in rate constants

constants in the equation 2.3 with the equations 2.10 and 2.11 yields the BV expression for current-potential characteristics as:

$$j = j^0 \left[\exp\left(\frac{\alpha F(E - E^{0'})}{RT} \right) - \exp\left(-\frac{(1-\alpha)F(E - E^{0'})}{RT} \right) \right] \tag{2.12}$$

where $j^0 = Fk^0(C^s_{Oxd})^{(1-\alpha)}(C^s_{Red})^{\alpha}$ is the exchange current density. The value of j^0 for unit surface concentration of the reactant equals Fk^0, which is a measure of the reaction rate at standard equilibrium potential.

According to the BV formalism, the anodic and cathodic current densities relates to the overpotential $(E - E^{0'})$ by an exponential function.[1] At conditions where $F(E - E^{0'}) \ll RT$, the exponential form of the BV equation can be linearized as,

$$j = j^0 \frac{F(E - E^{0'})}{RT} \tag{2.13}$$

Therefore, the charge transfer resistance $(R_{ct} = (E - E^{0'})/j)$ of the system can be calculated by measuring the current density at smaller overpotentials. A plot of the logarithmic value of j versus $(E - E^{0'})$, called Tafel plot, is useful to evaluate kinetic parameters. For larger overpotential values at which only one of the partial currents (anodic or cathodic) dominates, the Tafel plot generates a straight line. The value for α and j^0 of the system can be obtained from the slope and intercept of the Tafel plot. The condition for linearity in the Tafel plot holds only if the contribution from the back reaction to the net reaction current is arbitrarily less than 1% (or $\left| E - E^{0'} \right| > 118$ mV). Only highly irreversible systems (i.e. kinetically sluggish) can attain such high overpotentials before the interference of mass transfer limitations skews the measurements. Systems with facile electrode kinetics cannot observe the Tafel relationship without the absence of mass transfer effects. This is a major limitation to ET studies and provides an impetus for designing experiments that remove mass transfer effects.

---

[1] Overpotential is the measure of the extent of polarization (the departure from its equilibrium potential) of an ideally polarizable electrode, upon passage of faradaic current.

Figure 2.2 shows a simulated plot based on BV kinetics, in which the rate constant (both cathodic and anodic) increases or decreases *ad infinitum* with overpotential. It is evident in the same figure that, the slope of both oxidation and reduction plots significantly changes with respect to the value of transfer coefficient. An expression for the transfer coefficient is deduced from Equations 2.10 and 2.11,

$$\begin{aligned}\alpha &= -\frac{RT}{F}\frac{\partial \ln\left(\frac{k_{Red}^{BV}}{k^0}\right)}{\partial E} \\ &= 1 - \frac{RT}{F}\frac{\partial \ln\left(\frac{k_{Oxd}^{BV}}{k^0}\right)}{\partial E}\end{aligned} \tag{2.14}$$

which emphasizes the condition that oxidation and reduction plots (solid lines) in Figure 2.2 become symmetrical only when $\alpha = 0.5$; otherwise, the plots become asymmetrical, as shown by the dotted and dashed lines.

In summary, BV theory is based on macroscopic concepts, which predict the reaction rates are determined by three parameters, k^0, α and $E^{0'}$. This model is successfully employed to classify the kinetics of various redox systems and elucidate the reaction mechanisms. However, experimentally determined rate constants at a larger range of overpotentials deviate from the trajectory predicated in the BV model.(32) The empirical basis of the BV model also offers limited physical insight into how the ET kinetics are affected by factors such as the molecular characteristics of reacting species, solvent, electrode and adsorbed layers on an electrode. The value of α remains constant if the kinetic data is collected over a narrow range of potential near to $E^{0'}$ of the system. Since the heterogeneous ET rate constants raise exponentially with the applied potentials, the kinetically operable potential range is narrow in most electrochemical systems. At larger overpotentials, mass transfer becomes rate-limiting. Mass transfer is eliminated in surface-bound electroactive species; therefore, the kinetics can be measured over a large range of potentials.

2.1.2 Microscopic theories of electron transfer

Microscopic theories of charge transfer attempts to connect the gap between structural effects and observed ET kinetics. Microscopic electron transfer theories are developed based on *outer-sphere* reactions, hence the following discussion pertains to that class of reaction. Theoretical models of ET process are developed to explain outer-sphere ET reactions as it is the simplest possible case, and are later extended to inner-sphere ET reactions at the cost of theoretical complexities.

The Marcus-Hush model

Marcus theory was initially developed for homogeneous (solution phase) outer-sphere ET processes, and Hush contributed similar ideas during the same time.(33; 34) Marcus-Hush (MH) adapts transition state theory with the basic assumption of ET as radiationless electronic transitions between reactant/product so that electron transfer only occurs when the donor and acceptor are at same energy levels (*isoenergetic electron transfer*). In addition, the Frank-Condon principle needs to be established during the ET, according to which the reactant and product possess the same nuclear configuration at the transition state. The reactant and product will have potential energy as a function of various nuclear coordinates (including solvent coordinates), resulting in a multidimensional potential-energy surface. Transition state theory plots these potential energy curves against one reaction coordinate, q to simplify as a one dimensional profile as shown in Figure 2.3.(35) Both energy conservation and Frank-Condon principles are fulfilled only when the two parabolas intersect (transition state, $q^{\ddagger}$). The parabolic minima correspond to the most stable nuclear configuration of the reactants and products. ΔG^0 can be treated as free energy change for a homogeneous ET reaction or $F(E - E^0)$ for an electrode reaction. The energy barrier for the ET to occur is $\Delta G^{\ddagger}$.

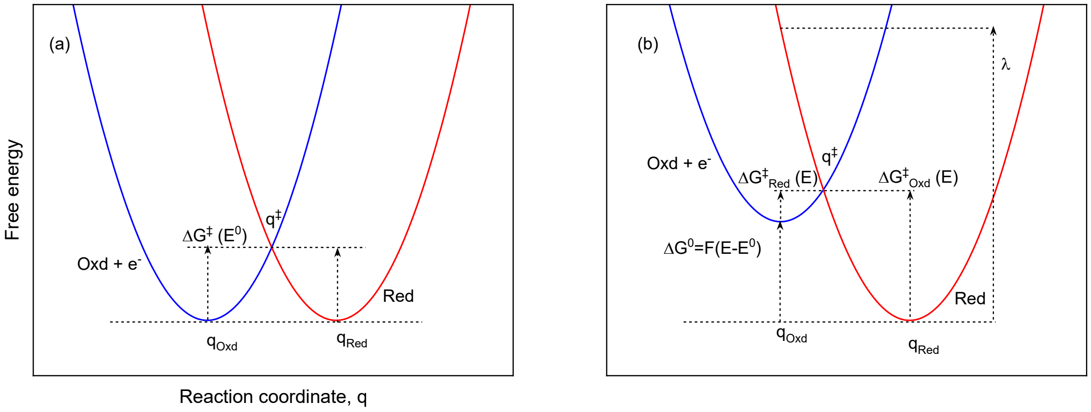

Figure 2.3: Two intersecting parabolas representing the quadratic variation of Gibbs energy curves in the Marcus-Hush model, along the reaction coordinate (combination of vibrational and solvent coordinates) at (a) $E = E^0$ and (b) $E - E^0 \neq 0$. The intersection point between two parabolas is the transition state ($q^{\ddagger}$).

Since the standard free energies of both the oxidized and reduced species, G^0_{Oxd} and G^0_{Red} depend quadratically on the reaction coordinates,(27)

$$G^0_{Oxd}(q) = \frac{k}{2}(q - q_{Oxd})^2 \tag{2.15}$$

$$G^0_{Red}(q) = \frac{k}{2}(q - q_{Red})^2 + \Delta G^0 \tag{2.16}$$

where k is the force constant for a change in bond length, q_{Oxd} and q_{Red} are the corresponding coordinates for the equilibrium atomic configurations of oxidized and reduced species, respectively. At the transition state, $q = q^\ddagger$ and $G^0_{Oxd}(q^\ddagger) = G^0_{Red}(q^\ddagger)$, and the equations 2.15 and 2.16 can be solved for $q^\ddagger$ as,

$$q^\ddagger = \frac{q_{Oxd} + q_{Red}}{2} - \frac{\Delta G^0}{k_j(q_{Oxd} - q_{Red})} \tag{2.17}$$

Since, $\Delta G^\ddagger = G^0_{Oxd}(q^\ddagger) - G^0_{Oxd}(q_{Oxd})$. If all free energies are referenced to $G^0_{Oxd}(q_{Oxd} = 0$, then $\Delta G^\ddagger = G^0_{Oxd}(q^\ddagger)$ and equations 2.17 and 2.15 can be combined to find the free energy of activation for the reduction half-reaction:

$$\Delta G^\ddagger = \frac{k(q_{Red} - q_{Oxd})^2}{8}\left[1 + \frac{2\Delta G^0}{k(q_{Red} - q_{Oxd})^2)}\right]^2 \tag{2.18}$$

Introducing $\lambda = (k/2)(q_{Red} - q_{Oxd})^2$, the above equation reduces to

$$\begin{aligned}\Delta G^\ddagger &= \frac{\lambda}{4}\left(1 + \frac{\Delta G^0}{\lambda}\right)^2 \\ &= \frac{\lambda}{4}\left(1 + \frac{F(E - E^0)}{\lambda}\right)^2 \end{aligned} \tag{2.19}$$

The equation 2.19 provides an expression for the activation energy barrier for ET in terms of total free energy of the reaction, ΔG^0, and the reorganization energy, λ. It is important to note that at condition where $E = E^0$, the value of $\Delta G^\ddagger = \frac{\lambda}{4}$. Using the expression for $\Delta G^\ddagger$ (equation 2.19), the ET rate constant in Arrhenius form can be written as,

$$k_{ET} = A\exp\left[\frac{-(\Delta G^0 + \lambda)^2}{4\lambda RT}\right] \tag{2.20}$$

The reorganization energy, λ, is the key concept introduced in MH formalism, and is defined as the Gibbs energy change associated with the distortion of the reactant to the equilibrium configuration of the products without the electron transfer. The reorganization energy has two contributions:

$$\lambda = \lambda_{in} + \lambda_{out} \tag{2.21}$$

λ_{in} is the solvent-independent term and can be computed from molecular theory by summation of normal vibration modes of the species:

$$\lambda_{in} = \frac{1}{2}\sum_j k(q_{Red} - q_{Oxd})^2 \tag{2.22}$$

where k are the force constants for each oscillator. The contribution of λ_{in} to the total reorganization energy is fairly small (0.1 to 0.3 eV). λ_{out} originates from difference between the orientation and polarization of solvent molecules around reactants and products. Born theory approximates the reactant and products as spheres and the solvent as a dielectric continuum, the so that solvent reorganization energy is expressed as:(4)

$$\lambda_{out} = \frac{e^2}{8\pi\varepsilon_0}\left(\frac{1}{a_0} - \frac{1}{2d}\right)\left(\frac{1}{\varepsilon_{op}} - \frac{1}{\varepsilon_s}\right) \tag{2.23}$$

where e is the elementary charge, ε_0 the permittivity of free space, a_0 the radius of the reactant, ε_{op} the optical permittivity, ε_s the static permittivity and d is the distance between reactant and electrode surface. λ_{out} shows a strong dependence on the distance between the electron donor and acceptor and is sensitive to conformational and geometrical changes.(36) The value of λ_{out} is more significant in case of polar solvents, $(1.0 - 1.5\ eV)$ whereas it is much smaller for non-polar solvents.

Predictions of MH theory

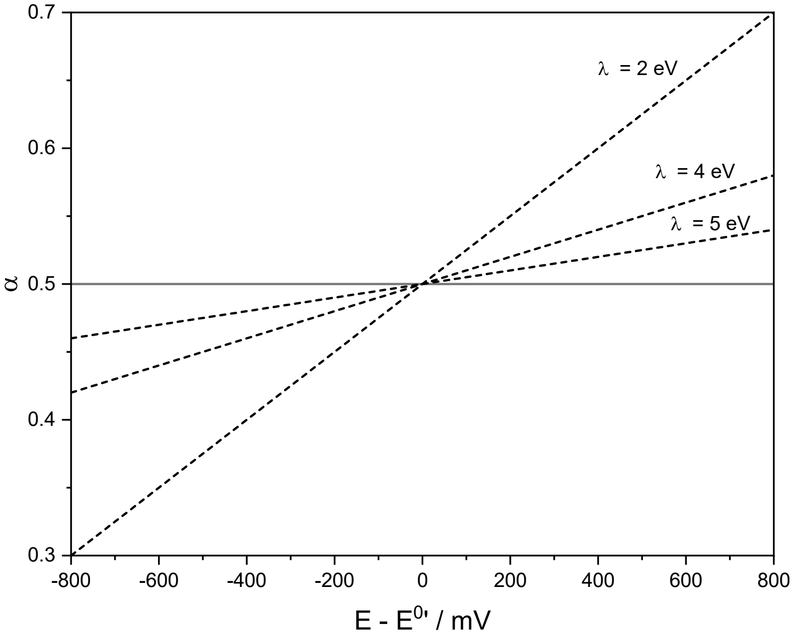

Figure 2.4: Variation of the transfer coefficient with applied potential according to the Marcus-Hush model. Gray solid lines in both figures correspond to values predicted by the Butler-Volmer model for α=0.5

Now, recalling that the transfer coefficent α is defined generally as the dependence of the free energy of activation on the applied potential, i.e. $\alpha = \frac{1}{F}\frac{\partial \Delta G^{\ddagger}}{\partial E}$, one can link the transfer coefficient to the reorganization energy by differentiating equation 2.19:

$$\alpha = \frac{1}{2} + \frac{F(E - E^0)}{2\lambda} \tag{2.24}$$

Hence, MH theory predicts not only that $\alpha \to 0.5$ when $E = E^0$, but also establishes its potential dependency as shown in Figure 2.4; in contrast, BV assumes α as a constant. Figure 2.4 also depicts that the potential dependency of α is difficult to observe experimentally since the value of α also depends on the magnitude of λ (usually not very large).

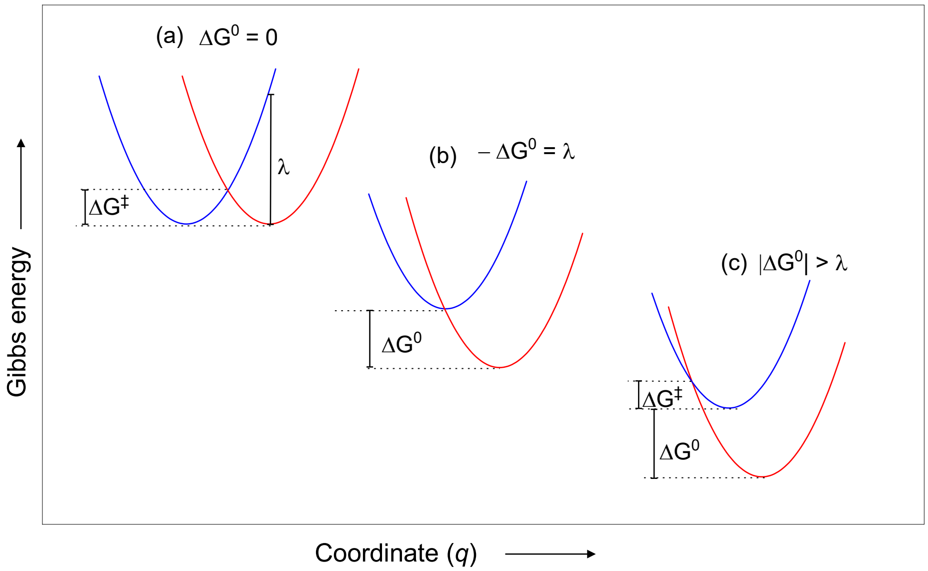

Figure 2.5: Schematic representation of free energy surfaces in non-adiabatic electron transfer reactions for (a) isoenergetic reaction, (b) reaction condition for maximum rate constant, and (c) inversion region

Another striking feature of Marcus theory, specifically regarding the kinetic parameters of homogeneous ET reaction, is illustrated in Figure 2.5. At isoenergetic condition, as represented in Figure 2.5(a), the minimum energy, required for the ET transfer from donor to acceptor without rearranging the solvation shell is $\Delta G^{\ddagger} \approx \lambda/4$. As $-\Delta G^0$ becomes more negative (i.e. a larger driving force for the forward reaction), one would intuitively expect a larger rate constant, k_{ET}. However, as λ is always a positive number, equation 2.20 predicts that starting from no driving force ($-\Delta G^0 = 0$) and moving to increasingly larger driving forces ($-\Delta G^0$ becoming a larger negative number) yields a maximum rate constant. The k_{ET} attains maximum when $-\Delta G^0 = \lambda$, and at this condition, Figure 2.5(b) shows that the activation energy becomes null. Marcus termed the region where $0 \leq -\Delta G^0 \leq \lambda$ as "the normal region". Figure 2.5(c) shows further negative $-\Delta G^0$ causes $\Delta G^{\ddagger}$ to reappear, but k_{ET} will decrease. This is called the "inverted region", where an increase in thermodynamic driving force leads to a decrease in the ET rate.(37; 38)

Although the Marcus inversion region is predicted, early attempts to observe it at the metal electrode electrolyte interface were unsuccessful. It was initially believed that it was because, with increase in $-\Delta G^0$ (or at larger overpotentials), diffusion-limited kinetics dominates the ET kinetics. Since the experimental rate constant (k_{obs}) is related to the ET rate constant (k_{ET}) and the diffusion limited (k_D) as,

$$\frac{1}{k_{obs}} = \frac{1}{k_{ET}} + \frac{1}{k_D} \tag{2.25}$$

conditions at $k_{ET} \gg k_D$, $k_{obs} \cong k_D$. The realization that redox-active SAM would allow experimental validation of the MH model because they mostly eliminate the mass transport effect was met with great enthusiasm. However, the inverted region remains elusive, and MH model needed to be modified for heterogeneous ET reactions.

Chidsey's adaptation of MH theory for electrode reactions

MH theory for ET treated reactants using a spherical model and defined the outer-sphere reorganization energy in terms of single coordinates. The assumption for ET at the metal electrode is that only the electronic state corresponding to the Fermi level of the electrode involves in the ET process. However, the electrochemical interface has more complicated geometrical, or boundary conditions.(36) Chidsey considered three aspects while adapting MH theory for electrode reactions: (1) metal surfaces, participating in the ET process provide a continuum of electronic states, and k_{Oxy} and k_{Red} will be the sum of the individual rates for each electronic state of the metal weighted by the Fermi-Dirac probability of occupancy/vacancy of that state;(2) the transition state rates of the activated complex is limited by the electronic coupling between the electronic states of the metal and the reactant molecule (i.e., the reaction should be nonadiabatic) and (3) the dominant contribution to the activation barrier is from solvent reorganization energy (precursor and product will have same nuclear configuration).(39)

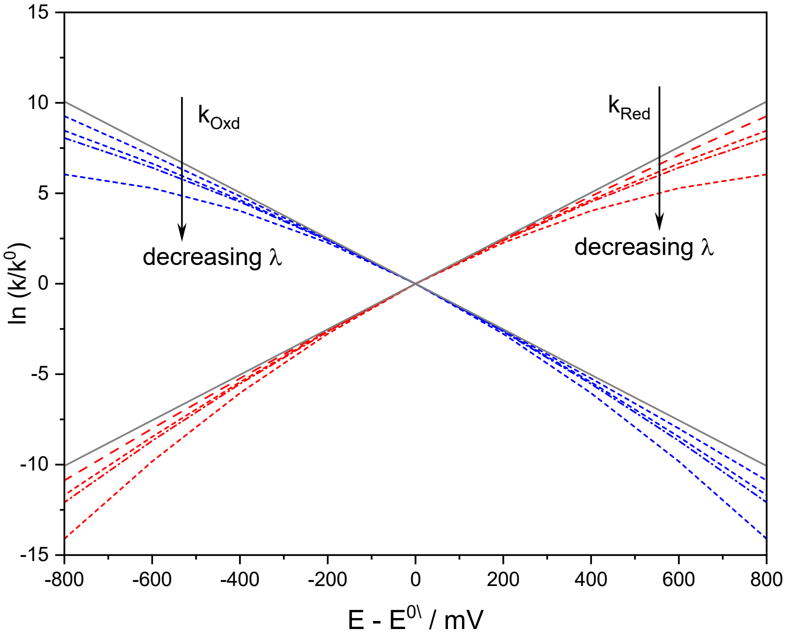

Figure 2.6: Marcus-Hush-Chidsey model showing change in the reduction and oxidation rate constants with the applied electrode potentials.

Contrary to the BV and the MH formalism, Chidsey's treatment for heterogeneous ET predicts a levelling of the ET rate constant with increasing overpotentials, as shown in Figure 2.6. In his original work, Chidsey used potential step chronoamperometry to study the oxidation of ferrocene groups tethered to the electrode surface via long-chain alkyl thiol.(39) The measured current, i corresponds to a potential step applied to the surface-bound redox species and is given by:

$$i = F\Gamma k_{app} \exp(-k_{app}t) \tag{2.26}$$

where F is the Faraday constant, Γ is the electrode surface coverage, t is the time and k_{app} is the apparent rate constant which is the sum of oxidative and reductive rate constants. Equation 2.26 shows that k_{app} of the redox reaction can be obtained from the plot of $\ln |i|$ versus t. Hence, current transient methods are ideal for interrogating ET kinetics, especially at higher overpotentials. Chapter 4 of the thesis provides a detailed discussion about the application of cyclic voltammetry and chronocoulometry/chronoamperometry techniques to study ET kinetics.

Distance dependence of ET rate

One of the major limitations of ET kinetics developed on classical transition state theory is the temperature dependence of ET rate (equation 2.20). Experimental results show that, at low temperatures, the ET rate becomes independent of temperature.(40) The limitation arises due to the assumption that ET occurs only by crossing the activation energy barrier. Quantum mechanical treatment of vibrational states allows the possibility of tunnelling through the barrier. The probability of tunnelling depends on the distance between the donor and the acceptor. The first-order rate constant for ET through tunnelling for a system where the donor and acceptor are separated at a fixed distance is,(4)

$$k_{ET} = \frac{2\pi}{\hbar} H_{RP}^2 (FC) \tag{2.27}$$

in which, FC is the Frank-Condon factor and H_{RP} is the electronic matrix element representing the strength of electronic state coupling between donor and acceptor, which can be expressed in terms of distance between the donor and acceptor as,

$$H_{RP} = V_0 \exp\left[-\frac{\beta_r}{2}(r - r_0)\right] \tag{2.28}$$

where V_0 is the donor/acceptor electronic coupling matrix element at vander Waals separation, R_0. β is a constant that determines the rate of falloff of H_{RP} with distance r. In ET systems where λ_{out} is small (since its value is distance dependent) and FC varies negligibly with r, the rate constant expression in equation 2.27 can be written as,

$$k_{ET} = k_0 \exp[-\beta(r - r_0)] \tag{2.29}$$

Equation 2.29 shows that ET rate falls off exponentially as a function of distance between donor and acceptor moieties, which is an indicative of electron tunnelling process. From the value of β for the bridging group, the effective tunnelling barrier (ΔE_{eff}) can be calculated as (41)

$$\begin{aligned} \Delta E_{eff} &= \left(\frac{\hbar^2}{8m_e}\right)\beta^2 \\ &= (0.952eV\mathring{A}^2)\beta^2 \end{aligned} \tag{2.30}$$

The β value estimated for saturated hydrocarbon chains is approximately 1.0 $\mathring{A}^{-1}$ (i.e $\Delta E_{eff} = 0.95$ eV).(42; 43) A smaller β value (0.04 $\mathring{A}^{-1}$ or $\Delta E_{eff} = 0.002$ eV) is reported for π-conjugated bridges (polyene and phenylenevinylene).(44) There exists a generally good agreement between theory and experiment for the distance dependence of ET rate constants, hence reliable quantitative tools can be adapted to predict the long range ET rate through various bridging units ranging from rigid molecules to complex proteins.

2.2 Conclusion

This chapter provides an overview of two commonly employed ET kinetic models: the empirical BV model and the MHC model. The simplicity of the classical treatment, adapted in the BV model, makes it a popular choice to study the ET kinetics as it agrees with the experimental values at relatively low overpotentials. However, the BV model fails to explain the experimental data showing the potential dependency of the transfer coefficient and the non-exponential behaviour of ET rate constants at higher overpotentials. The MHC model is built on transition state theory, developed through quantum mechanical treatments, and addresses the shortcomings of the BV model. Compared to BV, the MHC model describes the ET kinetics as a function of three parameters: the formal potential, the standard heterogeneous rate constant and the reorganization energy. A significant difference in the two models can be noticed with respect to the variation of the rate constants with the applied potentials. Unlike the BV model, in which the rate constants vary exponentially and continuously with $E - E^{0'}$, MHC predicts a limiting value for the rate constants with increasing overpotentials and reaches a plateau. Meanwhile, at potentials close to the formal potentials, the $\ln(k/k^0)$ vs $(E - E^{0'})$ curves obtained in MHC are very similar to those predicted by the BV model. MHC also reveals the larger reorganization energies significantly contribute to the overall ET kinetics. As the reorganization energy is made smaller, the rate constants reach the limiting value sooner with increasing overpotentials, and the plateau value is smaller. In short, contrasting differences between BV and MHC predictions are more evident at larger overpotentials and systems with smaller reorganization energy. MH formalism assumes both the reactant and product as identical free energy curves (harmonic oscillators with equal force constant k_f), implying the λ value has the same influence on the reduction and oxidation rate constants with applied potentials. Contrary to the above assumption, experimental data reports asymmetric Tafel plots for reactant and product, which shows the predicted symmetric MHC model inadequately fits experimental data for a range of systems. The MHC model is indistinguishable from the simpler BV model in the case of solution-phase redox species, at potentials close to equilibrium. BV model is better suited for the experimental fit of the data from most diffusion controlled systems. In summary, the BV model is easier to handle and compute, whereas the MHC offers better insights about electrode kinetics from the molecular nature of the electrochemical interface. The MHC model is considered a powerful theoretical framework for analyzing surface bound species, using transient methods such as chronoamperometry/chronocoulometry. The kinetic parameters extracted from both models may differ, depending upon the sensitivity of the model to the electrochemical techniques and the nature of the electrochemical interface (surface bound versus solution phase).

The scope of this thesis is the study of ET process of surface bound electroactive species with the application of surface enhanced IR spectroelectrochemistry, a cutting-edge tool for the in-situ analysis of electrochemical interfaces. To design such an interdisciplinary experiment and interpret the IR spectra collected at the timescale of the molecular events associated with the ET process, a prior understanding of ET kinetics of the system is required. In this thesis, the ET kinetics of two electroactive species, ferrocene and tetramethylpiperidine-1-oxyl ($\text{TEMP}\dot{\text{O}}$) radical, bound to the electrode surface via saturated alkyl chains, are examined. The ET kinetic models, BV and MHC are explored in this thesis within the experimental limitations to extract kinetic parameters.

3 Literature review on self assembled monolayers for electron transfer studies

3.1 Introduction

Self assembled monolayers (SAMs) are tightly packed molecular assemblies formed by spontaneous chemisorption of surface-active molecules with a specific affinity of its headgroup to a substrate (Figure 3.1). The two-dimensional network of these molecular films achieves order as the system approaches equilibrium. Functionalized long-chain hydrocarbons are the most frequently used building blocks for such well-organized molecular structures. In contrast to molecular films made by the Langmuir-Blodgett method and the chemical vapour deposition, SAMs are mechanically stable and durable in a moderate chemical environment. While following the simple fabrication process of SAM, a wide range of functional groups can be incorporated both in the alkyl chain and the chain termini (tail group). Therefore, various chemically modified surfaces with specific interactions can be recreated on experimentally controlled systems. In-depth knowledge about the structure of SAMs is essential for designing the experiments for electron transfer (ET) studies and interpreting how the molecular ensemble responds to the events associated with the ET process. This chapter provides a detailed literature background on the structure of SAMs and discusses major electrochemical studies of the ET process using electroactive SAM.

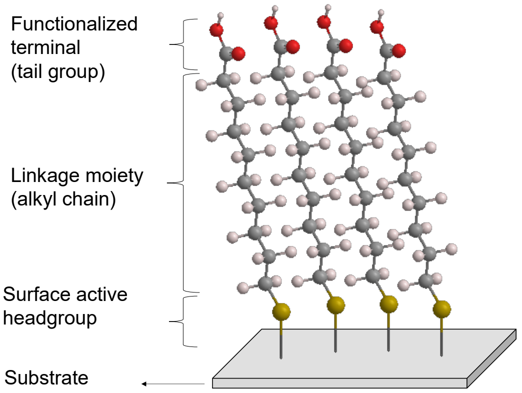

Figure 3.1: Schematic representing the structure of a self assembled monolayer

3.2 Literature on the structural study of SAM

The primary driving force for SAM formation is the chemical affinity between the head group and the substrate. Organosulphur compounds (thiols, disulfides, sulfides) are a prevalent choice to form SAMs on the gold surface due to the high affinity of sulfur to Au. However, the mechanism of Au-S bond formation is still under debate. The cleavage of the S-S bond in disulfide via oxidative addition to form thiolate on gold is reported in XPS and temperature-programmed desorption studies.(45), (46) The fate of hydrogen in S-H during Au-S formation is not confirmed. Possibilities are either hydrogen lost in the form of H_2 via reductive elimination on Au(111) in a vacuum or oxidative conversion to water in the presence of oxygen. DFT calculations show a strong coupling between the s-p orbitals of sulfur and the d orbitals of Au, resulting in the covalent bonding between Au-S.(47) Love et al. (48) published an in-depth review on SAMs, in which the authors discussed multiple studies to determine the bond energy of Au-S in alkane thiol SAMs formed from gas-phase and solution-phase. There are disparities in their conclusions, and the most reported values for Au-S bond strength is around 50 kcal/mol. The effect of solvent-adsorbate and solvent-substrate interactions on SAM formation is also a critical kinetic parameter.(49) Studying the dynamics of SAM formation from solution is difficult due to the complexity of the solid-liquid interface.(50) Gas-phase deposition studies show that molecular adsorption starts with a physisorbed, low-coverage (lying-down) phase and then transitions to chemisorption through a high-coverage (standing-up) phase. The lying-down phase is not detected in solution deposition, possibly because solvent molecules facilitate the standing-up phase by decreasing the transition energy threshold. The first step of the transition phase involves chemisorption of the headgroup with a high degree of gauche defects, which occurs in the first few minutes after the substrate immersion. This step follows Langmuir adsorption kinetics, during which 80%-90% coverage occurs. The second step is 3 to 4 times slower than the first step, during which straightening of the alkane chains occurs. The third and final step (35 to 70 times slower than the second step) consists of the reorientation of the terminal group.(51) Based on SHG studies, Dannenberger et al. (52) proposed a modified Langmuir adsorption model, in which the rate-limiting step is either the displacement of adsorbed solvent molecules by the monomer or incorporation of monomers from solution into the thiolate islands. In contrast, the electrochemical study by Schlenoff et al.(53) refutes Langmuir kinetics and proposes thiol adsorption as a diffusion controlled process. The adsorbate concentration shows a linear dependence on the growth rate. A higher concentration of adsorbate in solution produces dense films in a short time (in minutes); however, well-ordered film formation is a slow process. STM and IR studies show that long-term exposure of the substrate to the adsorbate solution decreases the density of vacancies (pinhole) and conformational defects of the alkane chains in the SAM. Reduced mobility of long-chain molecules is reflected in the lower rate of the initial (rapid) adsorption process. Based on the maximum surface coverage possible for alkane thiol SAM ($\sim 4.5 \times 10^{14}$ molecules cm^{-2}), the formation of a well-packed SAM requires more than 1 μM adsorbate solution. Ethanol is most widely used as the solvent for SAM preparation due to availability, low toxicity and its capacity for solvating organic molecules with varying degrees of polar character. The general criteria for choosing the substrate for SAM formation depend upon its application. A well-defined SAM formed by immersing an Au substrate in a dilute solution of long chain, ω-substituted dialkylsulphide was first reported in 1983.(54) Over the years, Au became a popular substrate material for SAM formation for various reasons. The stability of gold over a wide potential range enables different electrochemical analyses. Another favourable characteristic of Au promoting its use as a substrate for SAMs is the ease of preparing thin films on various surfaces via vapour deposition, sputtering, or electrodeposition. Compared to other noble metals such as Pt and Pd, thin films of Au with large grains ($\sim 45 - 60$ nm) are possible due to its relatively low melting point (1064 ℃). Large grains have fewer steps and defects; hence, they are ideal for substrates for studying SAMs. Treating the deposited Au films with hot piranha solution, followed by dilute aqua regia, can enhance the (111) texture.(55) Thin films of Au are used as substrates for various spectroscopies and analytical techniques such as atomic force microscopy (AFM), scanning electrochemical microscopy (SECM), surface plasmon resonance (SPR) spectroscopy and quartz crystal microbalance (QCM). This allows SAMs formed on Au substrates to be studied with multi-modal functionalities.

The packing and ordering of alkane chains are favoured by van der Waals interaction and opposed by entropy. The distribution of sulfur moieties on the metal lattice controls the free space available for packing alkane chains. In most cases, the alkane chain tends to adopt structural arrangements of the thiol-metal adlayer. Hautman and Klein conducted initial studies on the structure and dynamics of alkanethiol SAM formation on gold, using molecular simulations, in which SAM models with chain tilt were explored.(56) Including or excluding alkane chain tilt leads to a significant difference in the chain rotational dynamics. A low-energy electron diffraction study by Camillone et al.(57) on alkane thiol self assembled on various crystal planes of gold, discussed the spatial arrangement of sulfur on the underlying gold lattice. Here, the authors agreed with the *ab initio* calculations of Ulman and coworkers (58) that the sulfur atom binds to the three-fold hollow sites in fcc arrangement of Au(111) and forms a $(\sqrt{3} \times \sqrt{3})R30^0$ ($R =$ rotated) layer. This finding is supported by Widrig et al.(59) in their scanning tunnelling microscopy (STM) studies on gold surfaces. The spacing between adjacent sulfur atoms along the thiolate structure is ∼4.97 Å, which minimizes the S-S interaction (van der Waals radii of sulfur atom is 1.85 Å).(60; 61)

The alkane chain tilt depends on the S-S spacing in the adlayer. Since the distance of the closest approach for the alkane chains (4.24 Å) is smaller than S-S spacing in the adlayer on Au(111), a greater tilt angle for the alkane chain is possible as it maximizes the favourable interactions between adjacent alkane molecules. IR spectroscopy provides detailed evidence for the molecular orientation of the alkane chain. The width and position of the asymmetric CH_2 stretching vibration at 2918 cm^{-1} indicates well-ordered chains. Defects in the alkane chain structure lead to a blueshift in the peak position and broaden the bandwidth. Relative intensities of symmetric (2850 cm^{-1}) and orthogonal asymmetric polymethylene stretching vibrations indicate titling of the alkane chain to the surface normal. Hydrocarbon chain tilt, as measured on Au(111) using IR spectroscopy, and the grazing incident x-ray diffraction methods, reports $\sim 30^0$ from the surface normal.(62;

63) IR spectra also reveal that the C-C-C plane rotated about $\sim 55^0$ along the titling plane. The tilt and twist angle of hydrocarbon chains implies that the Au-S-C bond angle is $\sim 120^0$ to accommodate the chain packing. Various studies on the molecular orientation of alkane SAM on Au generally agree that a long alkane chain ($C \geq 22$) maintains all-trans, zigzag conformation on Au(111) lattice. However, they also observed a static disorder in aged alkane SAMs, where the molecules are randomly distributed between two orientations.

Gas phase studies show that alkane chain length significantly influences the kinetics of alkane thiol SAM formation on gold.(64) Formation of the SAM initiates with the physisorption of thiols on gold, followed by dissociative adsorption of the S-H bond. Longer chain alkanethiols have a higher reactive sticking probability than shorter ones. The heat of adsorption for the longer chain is large enough to overcome the activation barrier for the S-H bond dissociation process. As discussed before, SAMs formed from molecules with long alkane chains ($C \geq 22$) form $(\sqrt{3} \times \sqrt{3})R30^0$ structures. IR spectral inspection of docosanethiol (C=22) SAMs at low temperature showed a splitting of methylene scissoring mode at 1467 cm^{-1} into two peaks at 1472 and 1463 cm^{-1}.(65) However, a shorter alkane chain ($C \leq 17$) thiol SAMs reveals a dissimilar diffraction pattern than its long chain counterpart.(66) This contrast in the diffraction pattern of shorter alkane chain SAM refers to the formation of incommensurate c(4 x 2) superlattice on Au(111). Computational studies on packing and molecular orientation of alkane chains in the case of dodecanethiol ($CH_3(CH_2)_{11}SH$) SAM on Au(111) by Ulman et al.(60) reports pseudohexagonal (face-centred orthorhombic) structure.

X-ray diffraction profiles of alkanethiol on Au(111) show that the alkane chains have a tilt angle $\sim 31^0$. This results in a dissimilar surface projection of the terminal groups for SAMs with odd and even number of methyl units. In the case of CH_3 terminal SAM, the CH_3-CH_2 bond is perpendicular to the substrate for odd number of units, thus the monolayer surface consist of methyl group. For even numbered units, the terminal CH_3-CH_2 is tilted with respect to the normal, thus the surface consist of both methyl and methylene groups. The odd-even effect result in very different IR spectral patterns, due to the changes in direction of transition dipole moments of CH_3 stretching modes relative to the surface normal. The high frequency regions in the IR spectra of heptadecane and octadecanethiol SAM clearly show diagnostic change due to odd-even effect. Heptadecane (even numbered alkane chain) shows intense asymmetric (2957, 2965 cm^{-1}) and weak symmetric (2878 cm^{-1}) methyl stretches, whereas octadecane (odd numbered alkane chain) shows almost equal intensities. The odd-even effect causes a significant impact on the chemical behaviour of the monolayer interface, and the topic has been thoroughly reviewed.(67) The impact of odd-even effect on electron transfer properties of redox-active alkane chain is observed in the ET kinetic studies reported in this thesis and discussed in the subsequent chapters

Pristine Au(111) facets normally undergo a $(23 \times \sqrt{3})$ reconstruction to increase the atomic surface density by adding one extra Au atom per $(23 \times \sqrt{3})$ unit cell (or 4.4% higher density) than the original lattice.(68) Thiol adsorption on Au(111) lifts the reconstruction and induces one net atom vacancy per $(23 \times \sqrt{3})$ unit cell by releasing two atoms per unit cell to the surface terraces. The (110) crystal lattices of 5d fcc metals (Au, Ir, Pt) tend to undergo (1×2) reconstruction, i.e., every other closed-packed row of atoms along $[\bar{1}11]$ direction in the surface layer is removed, known as missing row (MR) type reconstruction.(69) Chemisorbed thiols on Au(110) precludes the MR surface reconstruction. The thiolate favours the rectangular hollow sites of the Au crystal lattice and form a commensurate $c(2 \times 2)$ layer on Au(110).(57) In the case of Au(100), adsorption of the short chain thiol molecules leads to the formation of $c(2 \times 2)$, however long chain alkanethiols are incommensurate with the underlying Au lattice.(64) Higher tilt angles allow stronger interchain interactions, hence the thiols in Au(111) expect to have more favourable inter-molecular bonds. Meanwhile, the lowest tilt angle of alkane chains results in the highest packing density (17.75 Å^2 per chain) in Au(100). The packing density of Au(111) is (21.74 Å^2 per chain) and that of Au(110) is (23.58 Å^2 per chain).

The surface properties of well-ordered SAMs depend on the terminal moieties of the monolayer. Nuzzo et al.(70) studied IR spectral features of various ω- substituted (CH_3, CH_2OH, COOH, CO_2CH_3) hexadecane thiol SAMs. These films differ primarily in the nature of exposed functionality; otherwise, they all exhibit sharp symmetric and asymmetric CH stretching bands centred at ~2850 and ~2918 cm^{-1}, respectively. These IR spectral features are similar to unsubstituted SAMs on Au with densely packed alkane chains and all-*trans* conformations. Ellipsometry measurements on all those mentioned above ω- substituted thiols showed the same thickness of 22 Å, indicating the orientation of the alkane chain is independent of the terminal group. The surface geometry of terminal ester groups can be estimated based on IR spectra, according to which, the carbonyl group is exposed to the ambient interface. Calculated transition dipole moments suggest that the O-CH_3 bond is close to perpendicular to the surface. Carboxylic acid substituted alkanethiols adopt similar orientations as discussed above, which leaves the O–H bond exposed at the surface. It is evident from the 1718 cm^{-1} peak that, the C=O moiety in the carboxylic acid forms inter-molecular hydrogen bonds with neighbouring headgroups. The vibrational data (shift in the characteristic wavenumber) indicates that these functional groups are chemically and physically distinct from their bulk phases.

The exposed functional groups of ω-substituted SAM provides room to alter the composition of surface layers after monolayer formation. Post modification of SAM has the following advantages. It simplifies the procedure to immobilize specific molecules of interest on a substrate. It also obviates the complicated synthesis of large molecules with anchoring groups like thiols. The surface modification makes it possible to generate multiple samples with different ligands on a standard SAM layer in a short period. This method preserves the ordered underlying structure of alkane chains, thereby avoid diffusion of molecules to the substrates. Tightly packed SAM terminals, due to its restricted motions, are expected to have higher energy barrier for reactions compared to solution chemistry. And also, the reaction conditions must be compatible with the stability of SAM. Sullivian and Huck reviewed various organic reactions suitable for modifying the surface chemistry of thiol SAM.(71) The current discussion focuses on reactions with carboxylic acid terminal alkane thiol SAMs, as they are within the scope of this thesis. Reactions used to modify carboxylic acid-terminated SAMs include the formation of acid chlorides, mixed anhydrides and activated esters. The latter is a popular method to immobilize biomolecules appended with amine groups under mild conditions. The reaction is often referred to as surface activation, in which the carboxylic group terminated SAM is allowed to react with an aqueous solution of *N*-hydroxysuccinimide (NHS), and a coupling agent like *N*-ethyl-*N′*-(3-(dimethylamino)propyl)carbodiimide (EDC). The reaction occurs at room temperature and is relatively fast (1-2 hour), producing a succinimidyl ester (-COOSuc)-terminated SAM. These active layers can efficiently form amide linkage with molecules containing amine terminals. Real-time monitoring of EDC/NHS reactions for surface modification under various conditions is discussed in Chapter 6 of this thesis.

3.3 Literature on ET studies using redox-active SAM

Ferrocene and pentaaminepyridine ruthenium redox couple labelled SAM layers are the most studied electrochemical interfaces for ET kinetics. In the landmark study of ET kinetics, Chidsey measured the rate constants of kinetically homogeneous redox sites of ferrocene groups tethered to a gold electrode via hexadecanethiol, over a large range of potentials and calculated the solvent reorganization energies of ferrocene redox species as 0.85 eV (the theoretical value is 0.94 eV).(39) Chidsey pioneered the application of potential step chronoamperometry to study the ET kinetics at the electrode interface. Initially, Chidsey modified the Marcus-Hush theory of homogeneous ET reactions for the electrochemical interface and reported an excellent agreement between the modified ET theory and the experimental results. Marcus-Hush-Chidsey (MHC) formalism satisfies the observed feature of ET rate constants, i.e. the observation of plateau in k_{ET} at larger overpotentials rather than continuing to increase exponentially as predicated by Butler-Volmer theory.(72) Chidsey considered only two parameters; reorganization energy and electronic state of the metallic electrode, and specifically excluded the effect of tunnelling from fitting the data with his theoretical model. The simulated Tafel plot becomes asymmetrical if through-space tunnelling was included in the formalism.(73) The change in the barrier height (as the electrode potential changes) results in the asymmetry of Tafel plot. Finklea and Hanshew (43) followed Chidsey's approach to study the ruthenium redox SAM in which $\mathrm{pyRu(NH_3)_5^{2+/3+}}$ was tethered to a gold electrode via different length (n=10, 11, and 15) alkanethiols. The potential step experiment yielded $\ln |i|$ vs t plot and its linearity indicated a kinetically homogeneous surface. This report successfully demonstrated the fitting of curved Tafel plots using MHC formalism and parameterized the electrode kinetics. The authors reported the standard ET rate constant is primarily determined by the number of methylene units in the bridging molecule. Another finding was a decrease in the reorganization energy of ferrocene moieties in the case of shorter alkane linkage, which was attributed to the lowering of the dielectric constant of the solvent molecules.(74) This behaviour of water molecules was explained as restricted freedom of rotation as the solvent molecules approached the polarized conductive interfaces. The tunnelling parameter β, (which depends upon the height of the energy barrier for the ET process and the nature of the bridging medium) for the saturated alkane chain was estimated as 1.06 ± 0.04 per $\mathrm{CH_2}$. Based on the tunnelling parameter value and the symmetry of the Tafel slope, Finklea proposed electron tunnelling through the alkane chain as the ET mechanism rather than through-space electron tunnelling.(43)

Defects in the SAM structure create a range of local environments in which the ET occurs with a distribution of apparent rate constants and is referred to as kinetic dispersion or kinetic heterogeneity. Rowe et al.(75) investigated different sources of kinetic dispersion using ferrocene-alkanethiol modified electrode model. Their model considered the kinetic dispersion arising from a Gaussian distribution of the formal potential of ferrocene redox sites, the reorganization energy, and the tunnelling distance. All three cases exhibited curved plots of $\ln|i|$ vs t and broadened cyclic voltammetric curves. The simulation of formal potential distribution provided the most consistent agreement with the experimental results, hence, it is considered as the likely cause of kinetic dispersion for that system. The impact of organized molecular films' chemical nature and structural composition on conducting electrons has been extensively studied. Reports have shown that conjugated bridges promote much stronger electronic coupling between the redox centre and the electrode than saturated alkane chains.(76) The interaction between adjacent molecular chains in compact films also plays a role in the ET process. Sumner et al.(77) investigated the rate constants in monolayers with a carboxamide group interposed between the alkane chain and the ferrocene. They reported that a carboxamide-linked ferrocene moiety had nearly the same rate constant as an alkane-linked ferrocene when the number of bonds in the direct pathway between the ferrocene group and the electrode was the same. Sumner and Creager compared the electrochemical behaviour of redox centres positioned within the interior portion of the monolayer and at the SAM termini.(78) The study was carried out on an electrode interface modified with the monolayers of ferrocenyl-decanethiol coadsorbed with 1-mercapto-eicosane ($C_{20}H_{41}SH$) and decanethiol. The ET kinetic analysis was carried out using AC voltammetry. The buried ferrocene groups within the monolayer exhibited sluggish electron transfer (200 s^{-1}) compared to the ferrocene groups exposed to the electrolyte (40,000 s^{-1}). The difference in the ET kinetics between 'buried' and 'exposed' redox centres was attributed to the difference in the local micro-environment around the two redox species. The buried molecular structure restricts the access of electrolyte anions to the redox-active sites. The study implies the ET from ferrocene to the electrode occurs concomitantly with anion transfer from the electrolyte to the oxidized ferricenium site in the monolayer. However, whether the ET is truly concomitant with counterion transfer remains an open question. Part of the motivation for this thesis is the development of time-resolved spectroelectrochemical tools that can differentiate the apparent rates of ET and ion transfer.

Ravenscroft and Finklea observed significant kinetic heterogeneity in the monolayers of $HS(CH_2)_nCONHCH_2pyRu(NH_3)_5(PF_6)_2$ co-adsorbed with $HS(CH_2)_nCOOH$ where n=10 or 15, on gold electrodes and in various nonaqueous electrolytes.(79) In this work, the authors introduced a reliable method to account for the iR drop while analyzing the chronoamperometric data for rate constants. The uncompensated resistance (from the electrolyte) and time constant (RC, which is the time required for the electrochemical cell to initiate faradaic processes after double layer charging) were determined from the non-faradaic current transients. These resistance values were used to correct the iR drop from the chronoamperometric data. Redox monolayers with n=15 displayed significant kinetic dispersion in nonaqueous solvents than in water. A possible explanation for this feature is that alkanethiolate monolayer order might be lost due to interactions of less polar solvents with alkane chains. In the event of kinetic heterogeneity, ET kinetics were measured for 50% and 90% conversion of the redox centres to the final oxidation state. Here, the smaller and larger conversion fraction represents the redox population with faster and slower kinetics. The standard rate constant between the faster and slower kinetic domains was varied by a factor of 8. The estimated solvent reorganization energy for the oxidation and the reduction of pentaaminepyridine ruthenium redox system was 0.9 eV and 0.7 eV, respectively. The asymmetry in the reorganization energies of oxidized and reduced species was postulated to change in the local solvent properties in response to switching the oxidation state for the redox centres. The CV features of the system under study inferred strong ion-paring properties of Ru(III) species, resulting in a larger effective radius and hence lowering the cathodic reorganization energy. Later, Finklea and coworkers conducted an electrochemical study of the pentaaminepyridine ruthenium redox couple affixed to the termini of monolayers co-adsorbed with $HS(CH_2)_mCOOH$, in aqueous electrolytes.(80) In this study, the number of methylene units in the diluent (m) were chosen appropriately such that position of the ruthenium redox centre in the monolayer were classified as 'matched' (n=m), 'exposed' (n=15, m=10-14) and 'buried' (n=10, m=11-15). Electrochemical measurements were carried out using a variety of methods including CV, ac impedance spectroscopy, and chronoamperometry. The kinetic heterogeneity in the redox system was manifested as unusually broad CV peaks under fast scan rates. The kinetic dispersion was attributed to disparity in the electronic coupling and reorganization energies within the population of redox sites due to diverse chain conformations and loosely packed domains. Presence of lattice steps and different crystallographic faces on the electrode surface could also have contributed to the kinetic heterogeneity. The estimated reorganization energy of $pyRu(NH_3)_5$ was in good agreement with the theoretical value of 1.0 eV. The value of tunnelling parameter (β) for the matched case (0.97 ± 0.03) was in excellent agreement with previous reports. However, β for the exposed case (0.83 ± 0.03) was significantly greater than buried cases (0.16 ± 0.02), which indicated the existence of alternative electron tunnelling pathways via proximate diluent thiols, other than the alkane chain tethered to redox centre. The discrepancy in the β value for the exposed cases has been attributed to the interaction between the redox centre and adjacent diluent terminus, which leads to an alternative ET pathway. In addition to the restricted access of counter ions, in the buried case, the degree of contact between the redox centre and the adjacent diluent alkane chains was relatively insensitive to the diluent chain length. An interesting observation is that the population of redox centres with faster rate constants (50% conversion) exhibits larger reorganization energy compared to the slower population (90% conversion). In fact, larger rate constant implies greater electronic coupling, which suggests that the redox centres are closer to the electrode surface or have better interaction with the SAM. Smaller reorganization energy is expected for closer redox centres due to image charge effects and the presence of a less polar monolayer environment. In contrast, the experimental data indicates faster population of the redox centres is located in more polar surroundings (i.e., outside the close packing of monolayer). Such anomalies are difficult to resolve by predominantly relying on conventional electrochemical methods. A major goal of this thesis is to use vibrational spectroelectrochemistry to obtain a better picture of molecular events associated with the ET processes at the electrode interface.

Liu et al. studied the electrochemical behaviour of amino-substituted ferrocene molecules covalently linked via amide coupling, onto a mixed SAM layers formed from carboxylic acid-terminated alkanethiols with either methyl-terminated or alcohol-terminated alkanethiols as diluents.(81) The electrochemical analysis were carried out using cyclic voltammetry. The estimated surface coverage of ferrocene indicated only 1-2% of the alkanethiol monolayer has a ferrocene attached. Hence, there were no interactions between ferrocene molecules resulting in very little kinetic heterogeneity. An interesting observation was that the apparent rate constant for the ET of ferrocene SAM with the alcohol terminated-diluents was significantly greater than the methyl-terminated diluents. According to Creager and Rowe (82), the ferrocene molecules nestles on the top of methyl-terminated SAM, creating a hydrophobic region around the redox moieties. Therefore, Liu and coworkers concluded that changing the diluent layer to an alcohol-terminated alkanethiol could create a more hydrophilic environment around the ferrocene, leading to better access of ions to the redox site and increased ET rates.

TEMPȮ (2,2,6,6-tetramethyl-1-pipyridinyloxy radial) is an electrochemically interesting redox molecule with three oxidation states. The free radical form of TEMPȮ can be oxidized to the nitrosonium ion (TEMPO^{+}) or reduced to the hydroxylamine. The TEMPȮ/TEMPO^{+} couple is reversible, whereas the TEMPOH/TEMPȮ couple is irreversible. Finklea and Madhiri studied the electrochemical properties of TEMPȮ (2,2,6,6-tetramethyl-1-pipyridinyloxy radical) attached via an amide linkage to prefabricated SAM layers of 11-mercapto-undecanoic acid on polycrystalline gold electrode.(83) Estimated coverage of TEMPȮ was $\sim$ 20% of the alkane SAM terminals. The kinetic parameters of TEMPȮ redox system was extracted using cyclic voltammetric analysis. The standard rate constant for the ET of TEMPȮ system tethered to the $HS(CH_2)_{10}$ linkage is 1.3 s^{-1}. The transfer coefficients (α) were calculated for a range of negative and positive overpotentials (η). The value of α at formal potential obtained from the linear regression fits of α vs η was greater than 0.5, therefore, as per the Marcus theory, the reorganization energy of oxidized species is expected to be greater than reduced species. However, the reorganization energies of TEMPȮ and TEMPO^{+} estimated from the slope of α vs η are 1.45 eV and 1.28 eV respectively. These are the first experimental measurements of reorganization energies for TEMPȮ/TEMPO^{+} redox system. The authors attributed this aberration in the reorganization energy of TEMPȮ species to the experimental uncertainties in the measurement of overpotentials and rate constants. TEMPȮ is a convenient redox system for IR spectroelectrochemical studies that has been explored in the subsequent chapters of this thesis.

3.4 Conclusion

This chapter provides a discussion on the structure of SAM layers as well as various ET kinetic studies conducted using SAM modified electrode surfaces. The discussion is mostly focused on alkane thiol monolayers self assembled on gold electrodes. The effect of alkane chain length, the crystallinity of the gold substrate and the terminal composition of alkane chains on the packing density of SAM layers was discussed to provide the reader with an appreciation of the complexities of such “model” systems. Literature reporting the surface activation reactions used for the post-modification of SAM terminal layers are also discussed. The later part of the chapter discusses various ET studies using electroactive SAM layers. The anomalies observed in the ET kinetics of various electroactive SAM systems discussed here highlight the importance of spectroelectrochemistry to obtain a detailed understanding of molecular events associated with ET processes at the electrode interface. The primary objective of this thesis is to study the electrode surfaces modified with various electroactive SAMs, such as TEMPȮ and ferrocene, using surface enhanced IR spectroelectrochemistry to correlate the molecular events with the ET kinetics.

4 Experimental methods and data analysis

4.1 Electrochemical methods

The electrode surface at the electrochemical interface is generally charged. The excess electronic charge carried by the metal surface is balanced by the electrolyte species of opposite in charge but equal in magnitude. This charge distribution at the proximity of the electrode-electrolyte interface is called the electrical double layer, and it can be modelled as a simple capacitor. Typically, electrode processes occurring at the electrode-electrolyte interface are categorized as faradaic and non-faradaic processes. The former process features charge transfer (or electron transfer) across the electrochemical interface, resulting in the reduction and oxidation of the adsorbed species on the electrode. In this thesis, measuring the kinetics of the faradic process and related events are the primary experimental objectives. The kinetics of such events must be separable from non-charge transfer processes, including adsorption and desorption of charged species from the bulk of electrolyte onto the electrode surface. In the case of systems with little non-faradaic contribution, the measured current is proportional to the rate of electron transfer (ET) reaction happening at the electrode-electrolyte interface. However, the rate of the overall ET process can be limited by the time it takes for the interface to charge up (double-layer charging) or mass transport limitation. Surface-modified electrodes are ideal for recording the current response exclusively from the ET reaction. This is because the electrochemically responsive moieties are tethered to the electrode surfaces, which forces the interfacial concentration of redox-participating species to remain constant and thus avoids mass transport limitations to measured reaction kinetics. It is often also the case that double-layer charging currents can be separated from faradic currents for redox-active self assembled monolayer (SAM) systems.

The condition at which the net current remains zero from the oxidation and reduction processes is referred to as equilibrium. At equilibrium conditions, the electrode holds a defined potential (E_{eq}) based on the surface concentrations, Γ (mol/cm^2) of the oxidized and reduced species, as

$$E_{eq} = E^{0'} + \frac{RT}{nF} \ln \frac{\Gamma_{Oxd}}{\Gamma_{Red}} \tag{4.1}$$

where $E^{0'}$ is the formal potential[1] of the electrode, n, R, T and F are the number of electrons, the gas constant, temperature, and the Faraday constant, respectively. To study ET kinetics, the system under equilibrium needs to be perturbed by changing the electrode potential and measuring the subsequent current response. The difference between the electrode potential (E) and its equilibrium potential, E_{eq} is referred to as overpotential, η. There are various methods to study the kinetics of electrochemical systems by applying potential perturbations, among which, this chapter will restrict the discussion to two electrochemical techniques widely applied in this thesis. The first one is potential sweep methods in which a periodic varying potential perturbation is applied, and the corresponding current is recorded. Here, the measured response will be periodic as well. The frequency variation in the perturbation is important to analyze the electrode processes occurring at different velocities. For a perturbation with small amplitude (typically $< 10mV$), the current response will become linearly proportional to the applied potential, whereas the current response will be nonlinear for perturbations with larger amplitude. The second category are potential step methods in which the system is initially at a stationary state (or, preferably, an equilibrated state) and then the electrode potential is stepped to a different potential. Electrode processes occurring at multiple velocities can be obtained by analyzing the measured response over different time scales.

---

[1] The formal potential is the modified form of standard potential, which includes the activity coefficients of the oxidation and reduction species

4.1.1 Potential sweep method: Cyclic voltammetry

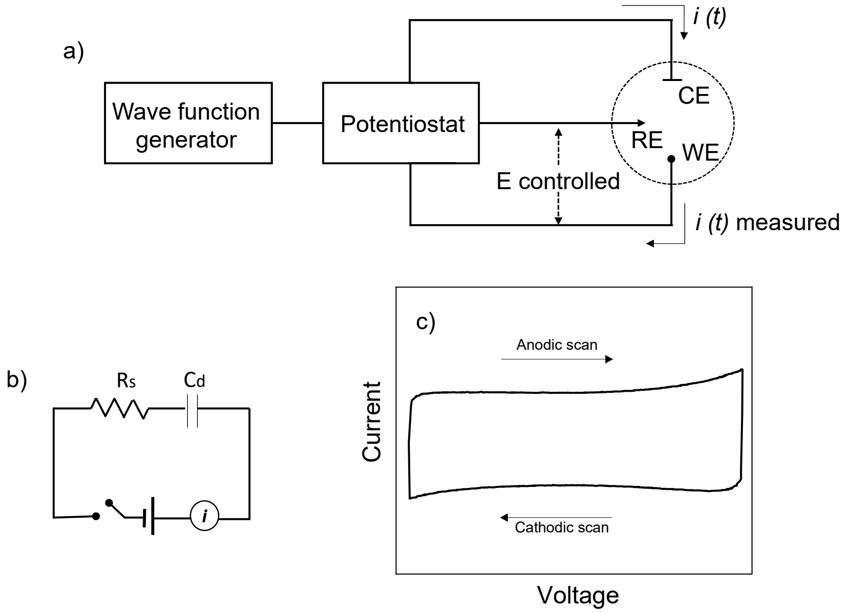

Figure 4.1: Cyclic voltammetry overview (a) experimental setup for electrode potential control and current measurement, (b) figure representing electrochemical cell in terms of circuit elements when the system is at open circuit potential, and (c) cyclic voltammogram of a simple RC circuit.

Cyclic voltammetry is widely practised as a preliminary analytical technique to survey the electrochemical processes occurring over the range of applied potentials.(84) In an electrochemical set-up, the bare working electrode (WE) should be ideally polarizable (no charge transfer across the interface), over the range of applied potentials. The reference electrode (RE) has to be ideally non-polarizable (electrode potential unaffected by the passage of current) so that cell potential is measured between the WE and RE (Figure 4.1(a)). The potentiostat holds high input impedance while measuring the potential difference between WE and RE electrodes to minimize the current drawn through the RE electrode. Figure 4.1(b) shows an RC circuit equivalent for an electrochemical system without any charge transfer process, in which R_s corresponds to the solution resistance exerted by the electrolyte and C_{DL} is the capacitive character from the electrochemical double layer at the WE interface. The applied voltage is the sum of the voltages across the resistor and the capacitor, therefore,

$$E = E_R + E_C = iR_s + \frac{q}{C_{DL}} \tag{4.2}$$

where i is the current and q is the charge on the capacitor. During the passage of current, a drop in the measured voltage between the WE and the RE, originating from the solution resistance, is equal to iR_s. At conditions where iR_s is large, a three electrode system is desired, in which the current is passed between the counter electrode (CE) and the WE. It is imperative that the species formed at the CE during the passage of current should not interfere with the electrochemical processes at the WE.

The current flowing through the double layer region in the absence of any faradaic process can be obtained by differentiating the charge stored in the capacitor as,

$$C_{DL} = \frac{q}{E}$$

or,

$$q = C_{DL}E$$

Therefore,

$$\frac{dq}{dt} = C_{DL}\frac{dE}{dt}$$

So, if the potential is scanned at a linear rate $\nu = \frac{dE}{dt}$ and if C_{DL} is approximated as being constant over the potential range, then the non-faradiac current is accounted as,

$$i_{nF} = \frac{dq}{dt} = C\nu \tag{4.3}$$

In cyclic voltammetry, the electrode potential is linearly varied with time between the desired voltage window. It is customary to record the current as a function of applied potential, and the current-potential plot, as given in Figure 4.1(c), is called a cyclic voltammogram (CV). The potential sweep rate, ν, can be varied depending on the investigation method. The features of the CV will provide the electrochemical behaviour of the system at the scanned potential window. The potential scan that drives oxidation is called the anodic scan, whereas the cathodic scan drives the reduction reaction. Cyclic voltammetry is a surveying tool, ideal for the qualitative evaluation of electrochemical systems. The capacitive feature (C_{DL}) of the electrical double-layer region at the electrode-electrolyte interface will result in a charging current upon every change in the electrode potential. Hence, the measured faradaic current response is always superimposed on the double-layer charging current. Therefore, the double-layer charging current is to be adequately accounted for while using the cyclic voltammetry for ET kinetic analysis.

Cyclic voltammetry of nernstian systems

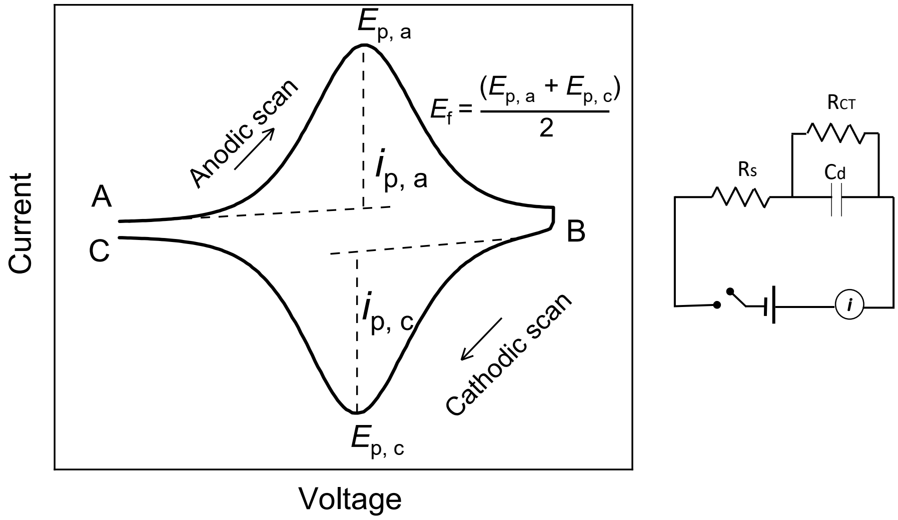

Figure 4.2: Cyclic voltammogram of a redox system and the Randles equivalent circuit

One can now consider how the interface model and the voltammetry differ when the WE surface is modified by a redox-active SAM. For an electrochemically reversible system, the faradaic process (charge transfer) occurs at facile rate without the limitation of mass transfer. Therefore, surface bound redox systems show electrochemical reversible character, especially at sufficiently low scan rates. The CV of the electrochemically reversible reactions shows characteristic features, with similar peak current for both anodic and cathodic scans, as shown in Figure 4.2. The corresponding Randles circuit is shown in the same figure, which features a charge transfer resistor (R_{CT}) parallel to the double layer capacitor. The current flowing through R_{CT} to the overall circuit increases with larger overpotentials. The CV features such as peak current, its position and area under the curve are relevant to obtain information about the environment around the redox centres. The anodic to cathodic peak potential separation ($\Delta E_p = |E_p^a - E_p^c|$) is ideally 0 mV, and the peaks are symmetrical with full-width half maxima (FWHM) of 3.53 RT/nF, or 90.6/n mV at 25 ^{0}C. Significant deviation from the theoretical values of FWHM can be attributed to intermolecular interactions between redox molecules. Shifts in the formal potentials of electroactive SAM compared to its solution analogs indicates the difference in the nature of the solvation sphere around the redox centres.

Under Nernstian conditions, the faradaic current is

$$i = \frac{4i_p e^{\theta}}{(1+e^{\theta})^2} \tag{4.4}$$

where $\theta = \frac{nF|\eta|}{RT}$, in which $\eta = E_p - E^{0'}$, and for redox-active layers adsorbed on the electrode, the peak current is

$$i_p = \frac{nF\upsilon Aq}{4RT} \tag{4.5}$$

Experimentally, the amount of charge, $q = nF\Gamma$ is obtained by integrating the faradaic peak after subtracting the double layer charging current and can be converted to surface concentration $\Gamma(mol/cm^2)$. Equation 4.5 reflects an important cyclic voltammetric feature of nernstian systems for adsorbed species, according to which, the peak current is linearly dependent on the sweep rate (υ). When the electron transfer kinetics cannot keep up with the faster scan rates, the redox system becomes irreversible, and peak separation (ΔE_p) increases.

Laviron developed a mathematical treatment for liner sweep voltammetry, where no-diffusion limitations apply, and the electrode species follow Langmuir kinetics. These equations enable one to extract kinetic parameters from experimental data obtained by CV at different scan rates, and its theoretical treatment is built on Butler-Volmer (BV) theory(see section 2.1.1). Determination of α, the symmetry measure of the energy barrier for the redox reaction, is crucial in Laviron's approach. Mathematical details of Laviron analysis are provided in Chapter 7. CV based ET analysis is less sensitive to kinetic heterogeneity, that is observed in electroactive SAM modified interfaces.(85) Kinetic heterogeneity is a distribution of ET rates that originates from the variations in the molecular environment around the redox centre due to the defects in SAMs. The major drawback of Laviron method is, contrary to its assumption, α deviates from its initial value at higher overpotentials (as noted by the Marcus model). Furthermore, the adsorption of electrode species does not always follow a Langmuir isotherm because the intermolecular interaction and analysis of CV data for kinetic information become complicated when double-layer effects and iR drop is included.

As an alternative to the Laviron method, kinetic parameters such as the reorientation energy λ can be elucidated by fitting the experimentally obtained plot of $\log i$ vs η, to the simulated curves predicted by Marcus-Hush-Chidsey (MHC) theory.(86) According to which, the rate constants of the reduction and oxidation half-reactions, k_b and k_f, can be written as,

$$k_b(\eta) = A \int \exp\left[-\frac{((\epsilon_F - \epsilon) + e\eta + \lambda)^2}{4\lambda k_B T}\right] [f(\epsilon)] \frac{d\epsilon}{k_B T} \tag{4.6}$$

$$k_f(\eta) = A \int \exp\left[-\frac{((\epsilon_F - \epsilon) - e\eta + \lambda)^2}{4\lambda k_B T}\right] [1 - f(\epsilon)] \frac{d\epsilon}{k_B T} \tag{4.7}$$

In equations 4.6 and 4.7, ϵ is the energy level of the electrode, ϵ_F is the Fermi level of the metal electrode, $f(\epsilon)$ is the Fermi function given in the expression, k_B is the Boltzmann constant and A is the pre-exponential factor. In the case of nonadiabatic electron transfer (weak coupling between redox molecule and electrode), the pre-exponential factor is expressed as:

$$A = \rho(\epsilon)|V_{AB}|^2 \left(\frac{k_B T}{\hbar}\right) \left(\frac{\pi}{\lambda k_B T}\right)^{\frac{1}{2}}$$

where $\rho(\epsilon)$ is the density of electronic states at the electrode energy ϵ, and V_{AB} describes the electronic coupling between redox molecule and electrode. Using the calculated values of rate constants, Tafel plots can be simulated and fit to the experimental data, to obtain values of λ and k_{ET}. The recommended range of $|\eta|$ in the experimental Tafel plot is at least one-half of λ in eV to obtain accurate values of the kinetic parameters. Since the above expressions (equations 4.6 and 4.7) are valid for homogeneous SAM layers where the electronic coupling between the redox molecule and electrode remains consistent, the presence of kinetic heterogeneity in the SAM layer compromises the accuracy of this method.

4.1.2 Current transient methods: Chronoamperometry and chronocoulometry

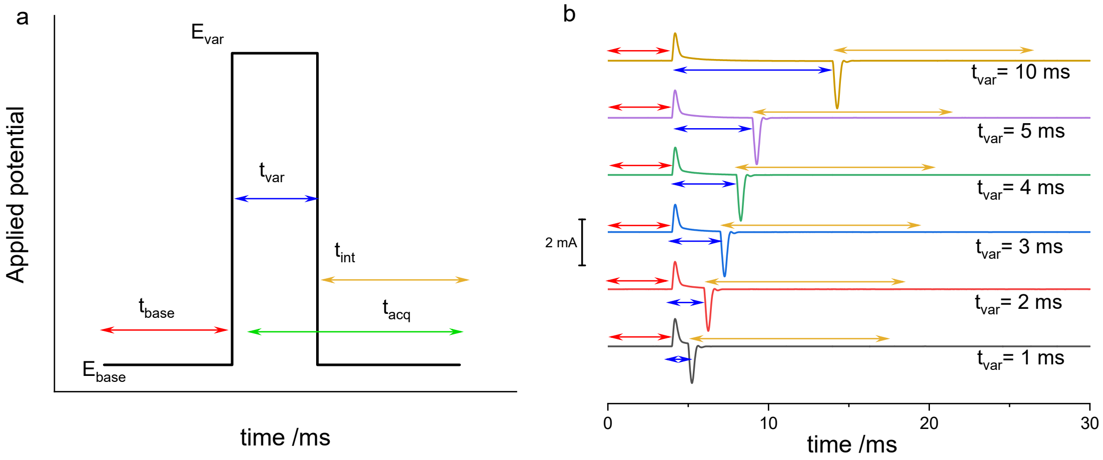

Figure 4.3: (a) Schematic representation of double-step potential applied to the working electrode, and (b) the current transients recorded at various time increments.

Chronoamperometry is a potential step method in which a square-wave potential is applied to the working electrode, and the current decay is recorded as a function of time. In a double-step experiment, a base potential is initially applied long enough to ensure the complete oxidation or reduction of the redox-active SAM. The potential is then "instantaneously" stepped to a potential, E_{var}, near the formal potential of the redox couple. The potential is then"instantaneously" stepped back to the base potential such that species generated in step to E_{var} are returned to their initial condition in the second step (Figure 4.3). The double-step routine is repeated using a series of values for E_{var}. The electrochemical stability window of the electrode and electrolyte needs to be considered while setting the potential steps for the measurements. The duration that the potential is held at E_{var} determines what fraction of the monolayer undergoes the ET reaction. As E_{base} is considerably removed from $E_{var} \approx E^{0'}$, the kinetics of the second ET process are exponentially faster than the kinetics of the first process. This means that the second current transient (i.e. the current vs time curve acquired for the step from $E^{var} \rightarrow E^{base}$) captures all the charge associated with reducing (oxidizing) the partially oxidized (reduced) monolayer formed in the first potential step $E^{base} \rightarrow E^{var}$. Implicit in the description of double-step chronocoulometry provided above is the assumption that each potential step is instantaneous and potential manifest at the SAM interface occurs much faster than the rate of measured ET. Thus, two important factors must be accounted for in the analysis of double-step chrono; 1) the RC constant of the cell and 2) the contribution of the measured current from double-layer charging ($q_{nonfaradaic}$). The faradaic response can be temporally separated from double layer charging provided the time constant for the latter is sufficiently smaller than the rate constant of the faradaic process. A detailed explanation of how the double layer charging is accounted for is provided in Chapter 7.

Once the faradaic current has been isolated, it can be fitted to a simple exponential decay,

$$i_F = F\Gamma k_{app} \exp(-k_{app} t) \tag{4.8}$$

where $k_{app}(= k_{Oxd} + k_{Red})$ is the apparent rate constant. Thus, the value of k_{app} can be obtained from the slope of $\ln|i_F|$ versus t. Deviation from linearity, more specifically, regions in the plot with different slopes, infers the kinetic heterogeneity of the redox sites.(75)

In chronocoulometry, the current transients stimulated by a potential step are integrated to obtain the charge passed as a function of time. The double-layer charging measured in the electrolyte, without electroactive species, q'_{DL} is not necessarily equal to q_{DL}. Double-step chronocoulometry is an efficient method to accurately estimate faradaic charges in the presence of appreciable non-faradaic charging. The technique is primarily developed to quantify the faradaic component associated with adsorbed species from the total charge measured, which comprises faradaic and non-faradaic components.(87) More details are provided in Chapter 7 with reference to a specific redox-active SAM.

Kinetic analysis using chronocoulometry

Both the chronocoulometry and chronoamperometry follows similar theoretical treatment however the earlier method offers some experimental advantage. In chronoamperomerty, the analog to digital converter for current measurement needs to be set to accommodate the initial spike of the transient. Therefore, decaying current during the later time of the transient is measured with poor sensitivity. Moreover, the bandwidth selection can distort the shape of current transient. In chronocoulometry, integrating the acquired current transients smooths the noise and recovers the relatively slow changing non-zero current contribution arising from the faradaic processes. Also, integration act nullifies the artifacts due to distortion of current transients.

This section presents analytical expressions for the transient charge versus time response of electroactive monolayers adsorbed on the electrode surface upon a potential step. The forward and backward reactions have characteristic first order rate constants k_f and k_b, respectively. The total coverage of redox-active species is the sum of the surface concentrations of Ox and Red, $\Gamma_{Oxd} + \Gamma_{Red} = \Gamma_{Tot}$. Defining a fractional coverage of the oxidized species as $\theta = \Gamma_{Oxd}/\Gamma_{Tot}$, a simple differential rate law for the redox reaction, $Ox + e^- \rightarrow Red$

$$\frac{d\theta}{dt} = k_b(1-\theta) - k_f\theta \tag{4.9}$$

Solving this linear, first-order differential equation leads to the time dependent expression for the coverage,

$$\theta(t) = \frac{k_b}{k_{app}}[1 - \exp(-k_{app}t)] \tag{4.10}$$

where k_{app} is defined above. At sufficiently large time, the interface equilibrates and,

$$\theta_{eq} = \frac{k_b}{k_{app}} \tag{4.11}$$

Practically, equation 4.10 can be applied to the charge data i.e. integrated current transients, generated from double-step measurements. The potential is stepped from an initial equilibrated state where $\theta_{eq} = 0$ to a new potential with $0 \leq \theta_{eq} \leq 1$. In the double-step measurement, each time interval (t_{var}) at which the electrode is held at E_{var} is shorter than the time required to oxidize/reduce the system completely. The faradaic charge, q_F, recovered in the subsequent return step to the base potential, is given by Faraday's law, $q_F = nF\Gamma_{Oxd}$. Similarly, the total charge associated with the reduction/oxidation of all redox-active species is $q_{F,max} = nF\Gamma_{Tot}$. Substituting these expressions into Equation 4.11 provides

$$q_F(t) = \frac{k_b}{k_{app}} q_{F,max}[1 - \exp(-k_{app}t)] \tag{4.12}$$

It is worth noting that when $E_{var} = E^{0'}$, i.e. at formal potential,$k_b = k_f$. And at this unique condition, the equation 4.10 becomes,

$$\theta(t) = \frac{1}{2}[1 - \exp(-k_{app}t)]$$

or,

$$\ln(1 - 2\theta) = -2tk_{app} \tag{4.13}$$

4.2 IR spectroelectrochemistry

Although the ET reaction is simplified as two conjugate species undergoing a reduction/oxidation with the exchange of electrons, in organized or complex systems, the redox reaction is only one of the potentially many chemical and physical processes associated with electron exchange. Assessment of the overall process is highly limited if it relies solely on an electrochemical response to a thermodynamic perturbation. Information from conventional electrochemical techniques is often inadequate for the elucidation of reaction mechanisms. Insight regarding molecular structural changes associated with interfacial electrode processes requires coupling the electrochemical measurements with other complementary techniques. The surface chemistry of the electrode differs significantly when it is removed from the solution; therefore, it is imperative to use *in situ* techniques to study electrode processes. Vibrational spectroelectrochemical techniques are ideal for probing the species adsorbed at the solid surface. Among these, the combination of infrared spectroscopy with electrochemical control called infrared spectroelectrochemistry (IR-SEC) is a popular *in situ* surface characterization method.(88; 89)

An elementary way to perform IR-SEC is in external reflection geometry, where IR light is allowed to reflect from the electrode surface while performing electrochemistry. Fourier transform (FT) IR spectrometers are capable of acquiring broadband spectra from near IR to far IR wavelengths, and this feature is called the multiplex advantage. IR-SEC methods make use of the multiplex advantage to perform SNIFTIRS (subtractively normalized interfacial FTIR spectroscopy). In this approach, spectra are collected separately at two potentials, in which at one potential no specific electrode activity occurs and the second potential triggers the electrochemical process. Subtracting the two spectra generates the so-called SNIFTIRS spectrum, which provides insight concerning the change in surface structure caused by the potential step.

The major constraint of performing IR-SEC in external reflectance mode is to maintain a thin layer of electrolyte ($1\sim 10\mu m$) over the electrode surface to reduce the IR absorption of aqueous electrolytes. However, low volumes of electrolytes drastically increase cell resistance and limit the mass-transport of reactants and products, which disturbs the spectral and electrochemical measurements. For the above reasons, the external reflection mode is not suitable for studying fast reactions. This problem can be circumvented by changing the configuration to attenuated total reflection (ATR). IR spectroscopy in ATR mode requires an internal reflection element (IRE) that is transparent to light in the IR frequency range. IREs are made of materials such as Si, ZnSe or diamond, and come in specific geometries suitable for ATR applications. The ATR process occurs only when the incident light is propagating from a high index medium (n_i) to low index medium (n_t), and requires the incident angle to be above the critical angle.[2] At this condition, the p-polarized fraction of incident light imparts momentum at the interface, generating an electric field normal to the reflected surface. This is called an evanescent field, which oscillates at the same frequency of incident photons and decays exponentially into the less optically dense medium. The electric field of the evanescent wave can be expressed as,

$$E = E_0 \exp(-\beta D) \tag{4.14}$$

where $\beta = \frac{2\pi\sqrt{\sin^2\theta_i - ((\frac{n_t}{n_i})^2)}}{\lambda_i}$ is the decay coefficient and D is the distance from the reflecting surface, into the low index medium. As a general rule of thumb, the evanescent wave penetrates a distance $\sim \lambda/2$. In this sense, ATR-FTIR offers some surface sensitivity, but it is insufficient to detect monolayer concentrations of electrochemical species formed at the electrode surface. Achieving that level of surface sensitivity requires coupling ATR-FTIR with plasmonic enhancement.

---

[2] Critical angle, $\theta_C = \sin^{-1}\left(\frac{n_t}{n_i}\right)$, where n_t and n_i are the refractive index of transmitted and incident medium, respectively

4.2.1 Surface enhanced IR absorption spectroscopy (SEIRAS)

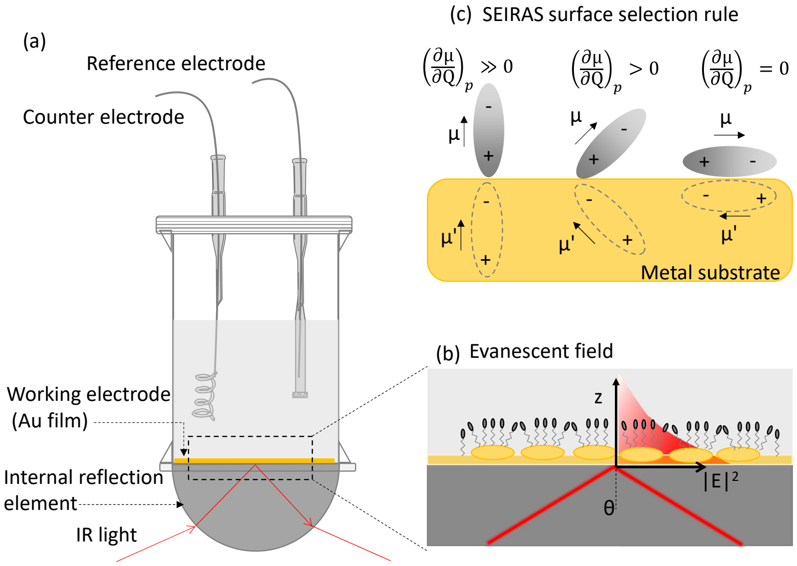
(a)
Reference electrode
Counter electrode
Working electrode
(Au film)
Internal reflection
element
IR light
(c) SEIRAS surface selection rule
$\left(\frac{\partial\mu}{\partial Q}\right)_p \gg 0$
$\left(\frac{\partial\mu}{\partial Q}\right)_p > 0$
$\left(\frac{\partial\mu}{\partial Q}\right)_p = 0$
μ
μ'
+
-
Metal substrate
(b) Evanescent field
z
|E|²
θ

Figure 4.4: (a) Schematic representation of Kretschmann configuration of ATR-IR spectroelectrochemical set-up, (b) the evanescent field confined to the electrode surface and (c) various orientations of dipoles and the induced mirror images on the metal substrate

If a plasmonically active metal island (smaller than the wavelength of incident light) film is in close contact with the dielectric medium, then the evanescent field couples to the localized surface plasmon resonance of the metal structure, resulting in an enhanced electric field around it. When analyte molecules are adsorbed on these plasmonically active metal islands, the IR radiation absorbed by the analyte molecules will be typically 10^2 to 10^3 times higher in magnitude than IR absorption without metal films. This phenomenon of enhanced IR vibration modes of adsorbed molecules on metal film was first reported by Hartstein et al.(11) The surface characterization technique utilizing the above phenomenon is now called surface-enhanced infrared absorption spectroscopy (SEIRAS). Osawa et al. proposed an electromagnetic model to explain the phenomenon of surface enhancement and computed the electric field enhancement factor using effective medium theory.(90) Effective medium theory is a formalism used to model the discontinuous metal island films based on a set of effective electrical properties, such as conductivity or dielectric function. In the case of SEIRAS, the effective property represents an average for the metal films, the substrate and the adsorbed layer of organic molecules. The dielectric function for the SEIRAS layer involves effective optical properties of the mixture of these components.

An efficient way to couple SEIRAS to an electrochemical cell is, to coat the top surface of an IRE with thin metal films which acts as a working electrode as shown in Figure 4.4. Such an optical geometry where the IRE is tightly bound to a metal film is called the Kretschmann configuration.(16; 91) ATR-IR measurement in Kretschmann configuration exhibits enhanced IR absorption by the molecules confined to the metal film surface.(11)

The total enhancement effect observed in SEIRAS is expected to have contributions from both electromagnetic (EM) and chemical factors.(92) The infrared absorption (A) can be expressed as,

$$A \propto \left| \frac{\partial \mu}{\partial Q} \times \mathbf{E} \right|^2 = \left| \frac{\partial \mu}{\partial Q} \right|^2 |\mathbf{E}|^2 \cos^2 \theta \tag{4.15}$$

where $\frac{\partial \mu}{\partial Q}$ is the derivative of the dipole moment with respect to a normal coordinate Q, $\mathbf{E}$ is the incident electric field and θ is the angle between $\frac{\partial \mu}{\partial Q}$ and $\mathbf{E}$. The enhancement is highly confined to the metal surface and decreases sharply with distance d from the surface, as represented by the following equation:

$$|E|^2 \propto \left(\frac{a}{a+d} \right)^6 \tag{4.16}$$

where a is the local radius of curvature of the island. It also proves a relatively short-ranged enhanced EM that contributes to the surface enhancement effect. According to the chemical mechanism, an increase in the absorption coefficient ($\left| \frac{\partial \mu}{\partial Q} \right|^2$) is due to the charge oscillations between the molecular orbitals of adsorbates and the metal surface.(93) Metals inherently show larger absorption coefficients in the IR region and the volume fraction of metal in the SEIRAS layer is larger compared to adsorbed layer of molecule. Therefore, change in the absorbance or reflectance of the metal are much greater than IR absorption of molecules. However, the polarization of the metal particle p is perturbed by the molecular vibration of adsorbed molecules by inducing a dipole δp. The induced perturbation is significant only at the vibrational frequencies of the molecule. As a result, the molecular vibration is observed through the change in absorption or reflectance of the metal film. In simple terms, the metal islands act as an amplifier for the IR absorption in SEIRAS.

At a high angle of incidence, p-polarized light has a sizable component of electric field vector normal to the metal surface. According to the surface selection rule of SEIRAS for molecules adsorbed on the metal surface, only the vibrational modes having nonzero dipole moment derivative components perpendicular to the surface are IR active.(94) The change in adsorbate dipole perpendicular to the surface constructively interacts with the image dipole (the adsorbate dipole induced in the metal) to enhance the adsorption.(95) Meanwhile, the adsorbate dipole parallel to the surface destructively interacts with its image dipole to reduce the adsorption. Surface selection rules are used to elucidate the molecular orientation of adsorbed species.

Baseline shift is a common characteristic feature of SEIRAS spectra. This is the result of reflectivity change of the metal films due to the adsorption of molecules on the SEIRAS films. The adsorption of molecules and anions decreases the reflectivity of SEIRAS films, which is attributed to the decrease in the free electron density of the metal surface. Meanwhile, adsorption of hydrogen can increase the reflectivity. The reflectivity of the interface is also governed by the refractive indices of the adsorbed layer and the electrode. Both the replacement of interfacial water molecules by the adsorbates and changes in the electronic state of the metal surface changes the reflectivity. Therefore, the baseline shift provides additional information about the surface changes and interaction of molecules with the electrode surface.

The enhancement factor of SEIRAS depends greatly on the morphology of the metal islands, which is influenced by the film fabrication methods. A common practise to prepare SEIRAS active metal islands is by vacuum deposition onto an IR transparent substrate.(96) Here, the metal deposition rate is a crucial parameter to obtain discontinuous metal islands. Potential cycling of the high vacuum deposited films in acidic electrolytes also leads to higher surface enhancement.(97) The main drawback of this method is, poor mechanical stability of the thin metal films due to poor adhesion between the metal film and the IRE surface. Electroless deposition of metals, especially Au on Si surface, is another popular method for SEIRAS film preparation.(98) Despite its excellent surface plasmonic enhancement, the preparation method is cumbersome and films are less reproducible. Electrochemical deposition is an alternative method for the fabrication of durable SEIRAS films. The method requires a conductive metal oxide (CMO) base layer, such as indium tin oxide (ITO) or indium zinc oxides (IZO), over the surface of IRE crystal. The surface roughness or film morphology, which plays a crucial role in enhancement factor, can be controlled by changing the electrochemical parameters such as deposition potential and solution concentration. Clarke et al.(99) demonstrated that anisotropic Au structures grown under potential control in presence of shape directing ligands, such as 4-methoxypyridine, showed excellent surface enhancement. A major concern of this method is that, the CMO coated IR substrates yields frequency shifted spectra as well as distorted band shapes. Andvaag et al.(100) reported that volume fraction of metal islands deposited on CMO plays a critical role in determining the overall reflectivity and as well can be used to control line shape and the band intensity of the IR absorption bands.

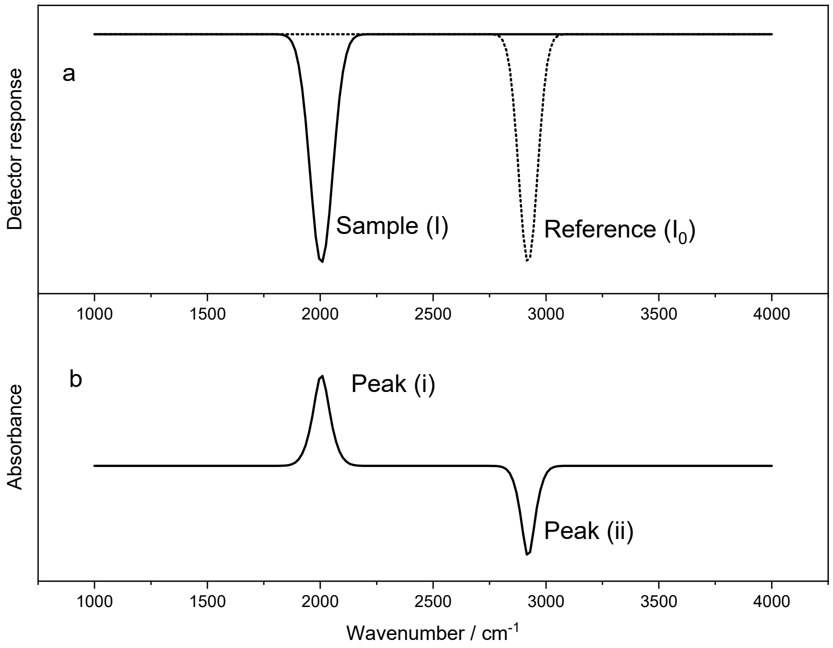

Figure 4.5: (a) Schematic representation of the IR single beam intensity at the detector of FTIR spectrometer, for the reference and sample potentials, (b) the absorbance spectrum is generated from the reference and sample signals. Peak (i) results from a situation where the vibrational mode is active in the sample single beam spectrum and inactive/not present in the reference spectrum. Peak (ii) is for the opposite case.

Conventionally, the electrochemical SEIRAS spectra are represented as absorbance spectra, $Abs = -log(\frac{I}{I_0})$, where I_0 and I are the IR signal collected at the reference and sample potentials. In the absence of IR active modes from surface adsorbed species, the signal measured at the detector in the reference single beam spectrum will be determined by the optical throughput of the experiment. However, if a molecule is adsorbed on the surface at the potential where the refence single beam spectrum is measured, the detected signal will be smaller than the full optical throughput at IR frequencies corresponding to the vibrational modes of surface allowed vibrational transitions. When the potential is changed and a sample, single beam spectrum is measured, the same arguments are applicable. As the final spectrum is the ratio of the two single beam spectra, the calculated absorbance can yield either an upward or downward feature depending on whether or not there were surface active modes in the reference and sample single beam spectra. This is shown schematically in Figure 4.5.

4.2.2 Time-resolved SEIRAS

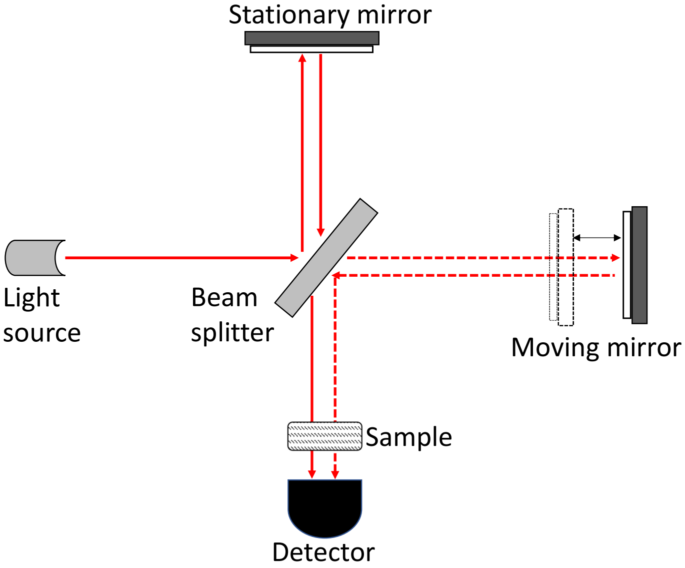

Figure 4.6: Schematic diagram of a Michelson interferometer configuration for FTIR

Modern FTIR spectrometers are equipped with Michelson interferometers that consist of a stationary mirror and a moving mirror, aligned in right angles to each other with a beam splitter positioned in the centre and equidistant to each other. Ideally, 50% of the light from the source is reflected towards the stationary mirror and the remaining light is transmitted to the moving mirror. The reflected light from both the mirrors recombines at the beam splitter. Unlike a dispersive grating instrument, the incident beam in FTIR comprises all frequencies bound to the IR region and are collected simultaneously at the detector (multiplex or Felgett advantage). The optical path difference between the two reflected beam introduced by the moving mirror give rise to an interference pattern due to the superimposing of sinusoidal waves at numerous frequencies. The resulting interferogram comprises a strong signal at the point corresponding to the point of zero path difference between the two beams and falls off rapidly on both side. These acquired interferograms are Fourier transformed to generate an IR spectrum. Principle advantages of FTIR spectrometer such as multiplex (Fellgett), throughput (Jacquinot) and wavelength accuracy (Connes), makes time-resolved IR measurement ranging from seconds to nanoseconds possible. Temporal resolution can be increased either by decreasing the maximum pathlength of the mirror, which comes at the cost of poor spectral resolution, or by increasing the mirror velocity. Although it reduces the signal-to-noise ratio, it can be circumvented by co-adding numerous interferograms. Consistent performance of the reaction on the IR substrate needs to be maintained to ensure a benefit from co-additions. However, large signal strength of ATR-SEIRAS enables to build high quality IR spectrum with smaller numbers of co-added interferograms. Prior knowledge about the reaction rate is necessary to choose the suitable time-resolved FTIR technique. Two complex approaches are employed in this thesis to study the time-resolved ET kinetics of various redox reactions.

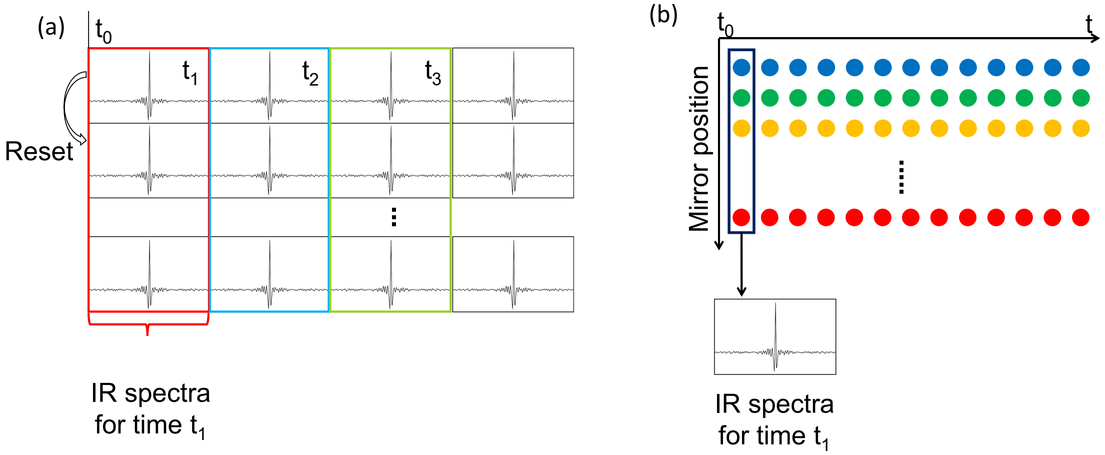

Figure 4.7: Schematic representation of (a) rapid scan FT-IR and (b) step-scan FT-IR. These figures are adapted from the PhD thesis of Kaiyang Tu (1)

Rapid scan requires fast scanning of the movable mirror, such that the duration of a scan should be at least one order of magnitude shorter than the half-life of the surface reaction under study. The acquisition of interferograms occurs in tandem with the potential perturbation applied to the IR spectroelectrochemical cell. Figure 4.7(a) shows the schematic representation of the rapid scan method. A series of interferograms are collected in rapid succession when the perturbation is triggered. After each set of acquisitions, the electrochemical system is reset to the initial state by applying the base potential. The measurements are repeated to collect interferograms sufficient to get an acceptable signal-to-noise ratio. Interferograms belonging to each time interval are co-added, and Fourier transformed to get the IR spectra of that particular time element. Mirror velocity in modern spectrometers allows rapid scan with a maximum of no better than 20 millisecond resolution. The physical limitation in rapid-scan TRS is the rate at which the mirror can be moved. Sheer inertial considerations limit mirror velocities to speeds that equate to maximum time resolutions in the range of milliseconds.

In step scan interferometry, the mirror moves at discrete steps along its path. The reaction is initiated with a potential step at each mirror position and transient signals are collected and averaged. The potential is reset to base potential to repeat the measurement at the next mirror position, as depicted in Figure 4.7(b). Thus, a complete interferogram can be obtained for each time interval, with the averaging of the signal collected at each mirror position. The time resolution in this method is independent of mirror movement and is only limited by the IR-detector response time and signal-to-noise ratio of the measurement. A major drawback of this technique compared to rapid scan is the requirement of many repeated sample perturbations and longer measurement time ($\sim$ 24 to 48 hours).

4.3 Conclusion

Spectroelectrochemical evaluation of a redox system primarily requires determining the potential window of interest at which the electrochemical reaction occurs and tuning the timescale of the measurement with the time constant of the electrochemical processes. This chapter covers the fundamentals and technical details of the electrochemical and IR spectroelectrochemical methods applied in the thesis. Conventional electrochemical techniques such as cyclic voltammetry and chronocoulometry provide a wealth of information regarding the electron transfer event. Elucidation of the reaction mechanism requires insights into the multiple steps involved in the electrode reaction. IR-SEC combines these complementary techniques and reveals molecular structure reorganization during the electrochemical processes. The ATR-SEIRAS method is employed in this thesis to study the electroactive monolayers assembled on the electrode surface. SEIRAS active films are fabricated using the electrochemical deposition method where the film morphology is well controlled, and enhancement features are continuously monitored, to avoid spectral band distortion.

5 IR spectroelectrochemical analysis of ferrocene terminated alkanethiol mixed monolayers

Contributions All the experiments and result analysis, discussed in this chapter are solely conducted by Bipinlal Unni, under the supervision of Dr. Ian Burgess. Methodologies used for the time-resolved spectroelectrochemical measurements are developed by Dr. Kaiyang Tu.

5.1 Introduction

Ferrocene as a redox probe has been well-utilized in electrochemical systems studying interfacial charge-transfer processes. A comprehensive discussion of the electrochemical studies of ferrocene-based self assembled monolayers (SAM) is beyond the scope of this chapter. Therefore, the current discussion is restricted to the most recent and relevant reports on electrochemical and attenuated total reflectance-surface enhanced IR absorption spectroscopy (ATR-SEIRAS) studies of ferrocene-terminated alkanethiol SAM. Ferrocene is a highly stable molecule that undergoes reversible one-electron oxidation and reduction reaction at the electrode interface in response to applied potentials. The chemical stability of ferrocene is due to its sandwich structure, which comprises a Fe ion between two cyclopentadienyl (Cp) rings. The Cp rings form π-bonded interactions with the central metal, and the metal-ligand coordination achieves a stable 18 e^- configuration (6 e^- from Fe^{+2} and 6 e^- from each Cp). During the oxidation and the reduction reactions, Fe in ferrocene changes its oxidation state between Fe^{+2} and Fe^{+3}.

Ferrocene can be functionalized with versatile substituents, on one or both the Cp rings, without affecting the electrochemical reversibility or the structural stability. Therefore, ferrocene derivatives have been tailored as redox markers and immobilized on desired substrates as monolayers.(101; 102; 103). However, a huge disparity has been reported in the redox behaviour of the ferrocene-terminated monolayers. Apparently, various factors such as the substituent group's functionality, substrate morphology, the nature of counter-ions, and the interaction between the adjacent ferrocene centres influence the ferrocene SAM redox behaviour. Ferrocene with electron-withdrawing substituents has higher oxidation potentials and vice-versa.(104) Fontanesi et al. (105) reported quasi-reversibility for hydroxy substituted ferrocenes covalently grafted on the Si(111) surface. Taherinia studied the electron transfer kinetics of ferrocene-terminated SAM with varying numbers of cyclohexyl groups as spacers in ionic liquids.(102) The standard rate constant values remained the same for all ferrocene systems irrespective of the increase in the spacer length, which is attributed to the nature of the electrolyte-SAM interactions. Many previous reports established that the densely covered redox terminated monolayer shows CVs with peak separation much greater than the theoretically reversible system.(106; 27). The deviation from reversible behaviour is attributed to the interaction of the neighbouring ferrocene terminals, which results in a variation in the local chemical environment at the redox centres.(107) Intermolecular electron transfer occurs between the closely positioned ferrocene moieties, manifesting in the CVs as a broad redox peak. The steric hindrance caused by the bulky head group of the monolayer units results in altering the packing density and orientation order in the SAM. Diluting the functionalized monolayers with long chain molecules (diluents) results in isolating the redox sites within well-defined monolayers. The chain length of the diluent molecules with respect to the redox linkage unit plays an important role in setting the local environment around the redox centres in the SAM modified interfaces. Creager and Rowe (82) studied mixed monolayers of ferrocenyl-hexanethiol coadsorbed with several n-alkanethiol as diluents. The formal potential shift was smaller with short chain-alkane thiols and alkane chains with polar substituents; however, a significant positive shift was observed with increasing alkane chain length of the diluents. This behaviour was attributed to the solvation and double layer effects when the redox moieties are enveloped inside the alkane-like pockets of long chain diluents. The former refers to the perturbation of the redox activity due to the stabilization of the redox moieties inside the diluent molecules. The latter refers to the restricted access of counter-ions to these pockets.

Rudnev et al.(108) employed ATR-SEIRAS to examine the effect of different anions on the redox behaviour of mixed monolayers of ferrocenyl-1-undecanethiol ($FcC_{11}SH$) and decanethiol ($C_{10}SH$). The authors claim that SEIRAS experiments were performed with quasi-single crystalline Au(111) films. Their report provides a molecular picture of the ferrocene redox process, according to which the repulsive force between the ferrocenium moieties and the positively charged substrate surface leads to a more upright orientation of the alkyl chains, with respect to the electrode surface. Also, they predict that upon oxidation there is a rotation of the ferrocene ring around the bond between ferrocene and the carbonyl-terminated alkyl chain. Their study reveals the formation of interfacial ion-pairs in correlation with the extent of water coadsorption. Hydrophobic anions such as ClO_4^- form ions pairs with Fc^+ ions whereas the stronger solvation shell around hydrophilic anions such as SO_4^{2-} prevents ion pairing. The above information about the redox processes of ferrocene and the solvents corresponds to a static picture of the electrode-electrolyte interface. A more dynamic description of these elementary interfacial processes is required for a better picture of the redox processes.

Within the scope of the thesis, this chapter presents a comprehensive study involving voltammetric, and time-resolved SEIRAS analysis on the redox response of an undecanethiol substituted ferrocene SAM coadsorbed with decanethiol. This study specifically aims at the structural effect of the diluents in the redox-active SAM, as well as the influence of increasing hydrophilicity of the counter-ions on the redox process of ferrocene SAM. By using per-deuterated 1-decanethiol it is possible to differentiate the SEIRAS signal of the diluent molecules from the complex SEIRAS spectra of the ferrocene SAM. The redox behaviour of the ferrocene terminated SAM in a mixed monolayer is studied using two different anions, ClO_4^- and NO_3^- due to their difference in hydrophilicity. Based on the electrochemical and SEIRAS analysis, a molecular model is proposed for the redox process of ferrocene-substituted alkanethiol SAM on the Au surface.

5.2 Experimental

Reagents and electrode preparation The reagents used in this study were purchased from Sigma Aldrich and the deuterated diluent, 1-Decane-d21-thiol ($C_{10}D_{21}SH$) was purchased from CDN isotopes. The reagents required for electro-deposition of Au film for SEIRAS measurements were potassium gold (III) chloride ($KAuCl_4$), 4-methoxypyridine. The reagents required for ferrocene SAM mixed monolayers were 11-ferrocenyl-1-undecanethiol $Fc(CH_2)_{11}SH$ ($FcC_{11}SH$), 1-decanethiol $CH_3(CH_2)_9SH$ ($C_{10}SH$). The reagents required for EDC coupling reaction were N-(3-Dimethylamino propyl)-N'-ethylcarbodiimide hydrochloride (EDC), N-Hydroxysuccinimide (NHS), aminoferrocene and mercapto-hexadecanoic acid, COOH-$CH_2(CH_2)_{15}SH$ (COOH-$C_{16}SH$).

The electrode for the electrochemical measurements was a gold bead electrode (polycrystalline), which was made by melting a 0.5 mm gold wire (99.99%) in a propane flame. The gold bead electrode was treated with aqua regia to remove the surface metallic impurities, and melted repeatedly. The gold was allowed to cool slowly in air after the final melt. The Au electrode was immersed in a freshly prepared piranha solution (3:1 H_2SO_4 and 30% H_2O_2) for 30 seconds and gently flame annealed prior to every experiment. The Au electrode surface was modified with various ferrocene-SAM mixed monolayers by immersing it in 5 mM solutions (95% ethanol) of the different fractions of $FcC_{11}SH/C_{10}SH$ for four hours. Then, the electrodes were rinsed thoroughly with 95% ethanol and stored in deionized water.

For the amide coupling reaction, the Au bead/film was modified with acid-terminated alkanethiol (COOH-$C_{16}SH$) SAMs by immersing the cleaned gold bead electrodes in 5 mM (COOH-$C_{16}SH$) solutions (solvent was 95% ethanol) for four hours. Then, the electrodes were rinsed thoroughly with 95% ethanol and deionized water. The SAM layers were treated overnight with a reaction mixture containing equimolar concentration (5 mM) of EDC and NHS. Then, the electrodes were treated with 5 mM solution of aminoferrocene in 95% ethanol.

Electrochemical measurement were done with a HEKA PG590 potentiostat and custom software written in the LabVIEW environment. A home-made Ag/AgCl in saturated KCl was used as the reference electrode and a flame-annealed, coiled gold wire served as the counter electrode. The electrolytes were 0.05 M $KClO_4$ and 0.05 M KNO_4 prepared in deionized water.

SEIRAS substrate preparation and spectroelectrochemical measurements A 60° face-angled Si crystal (PIKE technologies) was used as the internal reflection element (IRE) for ATR-SEIRAS experiments. The principal reflecting plane of the IRE was polished with 3 microns and 0.5 microns diamond polishing solutions, rinsed with copious amount of deionized water and air dried. Approximately 20 nm thickness of indium tin oxide (ITO) was sputter coated on the IRE surface using a home-built RF magnetron sputtering unit using a power of 30 W and a base vacuum of 4×10^{-5} Torr. The ITO sputtered IRE was annealed under vacuum at 300 ^{o}C for an hour and was assembled in a Jackfish SEC J1 cell (Jackfish JEC). The ITO-coated Si IRE served as the working electrode for in situ spectroelectrochemical experiments. SEIRAS active gold layers on the ITO surfaces were prepared by electrodepositing gold islands from an electrolyte containing 0.25 mM $KAuCl_4$, 0.1 mM 4-methoxypyridine and 0.05 M $KClO_4$. After the electrodeposition, the gold layer on ITO was rinsed thoroughly with deionized water, before $\text{TEMP}\dot{\text{O}}$ coupled SAMs were formed on the Au island film using the protocol described in the previous chapter.

SEIRAS measurements were performed using a Bruker Vertex 70 FT-IR spectrometer with a liquid nitrogen cooled, MCT detector. An in-house developed Labview program was used to control both the IR spectrometer and potentiostat. The IRE assembled Jackfish SEC cell was mounted on a VeeMax III optic box (PIKE technologies) and the angle of incidence was set to 60°. The IR spectra were collected between 800 and 4000 cm^{-1} at 8 cm^{-1} resolution and 2 mm aperture. The scanning velocity was 40 kHz for ATR-SEIRAS measurements and 160 kHz for the time-resolved ATR-SEIRAS measurements. The spectra are plotted in absorbance scale, $Abs = -\log \frac{I}{I_0}$, where I and I_0 are the single beam intensities collected at the sample and reference potentials, respectively.

5.3 Results and discussion

5.3.1 Cyclic voltammetry of $FcC_{11}SH$ / $C_{10}SH$ mixed monolayers

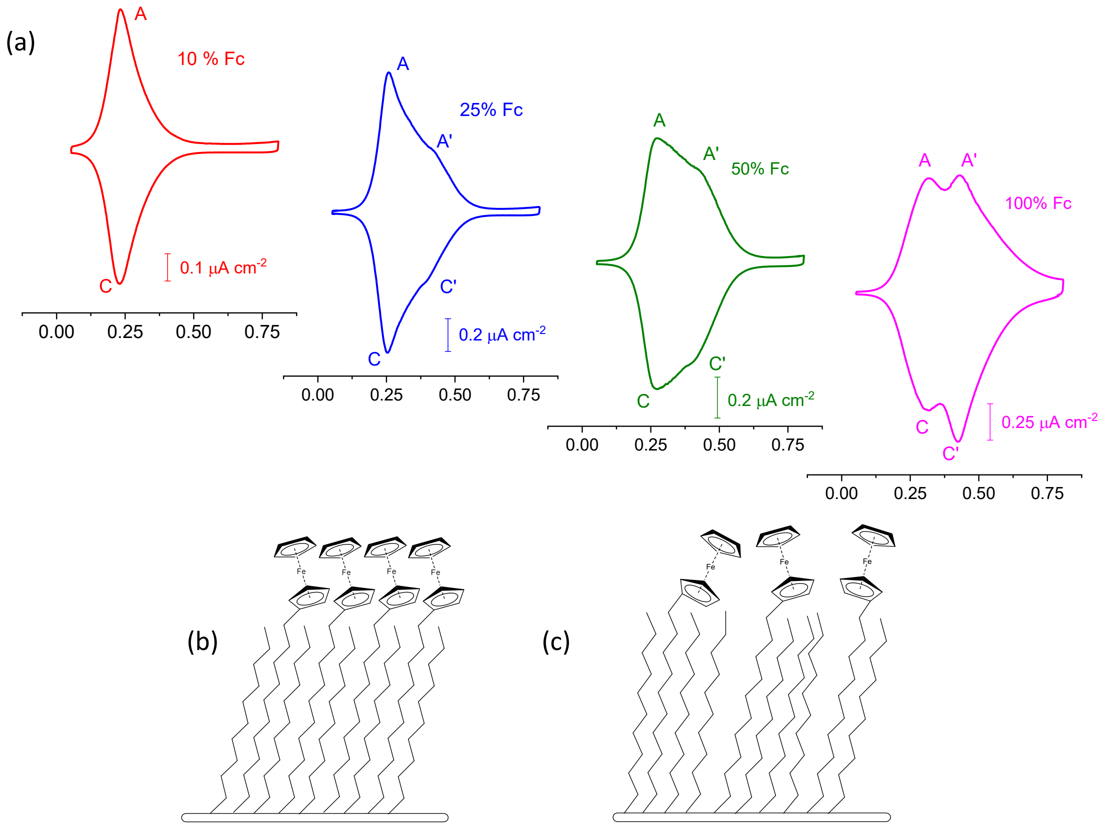

Figure 5.1: (a) Cyclic voltammograms of ferrocene SAMs on polycrystalline Au bead at a scan rate of 20 mV/s in 0.1 M $HClO_4$. Each cyclic voltammogram corresponds to the SAM layers prepared from different fractions of $FcC_{11}SH$ to $C_{10}SH$. The multiple peaks at anodic (A, A') and cathodic (C, C') scans are marked on individual cyclic voltammograms, (b) and (c) are the schematic representation of densely packed and isolated ferrocene units in the mixed monolayers of SAM, respectively

% $FcC_{11}SH$ incubation sol'n	**Ferrocene coverage (x 10^{-10} moles cm^{-2})**	**First redox (A/C) peak potentials / V**	**Peak current (A/C)**	**Second redox (A'/C') peak potentials / V**	**Peak current (A'/C')**
1 %	0.04	0.201 (0.198)	1.23	–	–
10 %	1.44	0.234 (0.229)	1.04	–	–
25 %	2.92	0.262 (0.253)	1.00	0.436 (0.411)	0.910
50 %	3.41	0.265 (0.261)	1.42	0.436 (0.426)	0.954
100 %	5.46	0.306 (0.286)	1.09	0.436 (0.432)	0.826

Table 5.1: Data summarized from the CVs of the mixed monolayers of $FcC_{11}SH/C_{10}SH$ shown in the Figure 5.1

Figure 5.1 shows the CV of ferrocene SAM in mixed monolayers consisting of different ratios of $FcC_{11}SH$ / $C_{10}SH$. The CVs are measured at 20 mV/s sweep rate. The data obtained from the cyclic voltammograms are summarized in Table 5.1. After the double-layer correction, the integrated oxidation and reduction currents provided the charge (q) contribution of ferrocene anions and cations, respectively. Assuming the ferrocene redox process involves single electron transfer, the surface concentration of ferrocene moieties (Γ) can be estimated according to $q = nF\Gamma$, where F is the Faraday constant. The ferrocene surface concentration on the Au electrode is controlled by changing the concentration of the diluent ($C_{10}SH$) in the incubating solution. An incubating solution containing 1:100 $FcC_{11}SH$ to $C_{10}SH$ resulted in mixed monolayers with 0.04×10^{-10} moles cm^{-2} of ferrocene, whereas the ferrocene coverage on an Au electrode without any diluent is 5.46×10^{-10} moles cm^{-2}. The experimentally calculated Γ for the 100% $FcC_{11}SH$ monolayers is higher than the theoretically estimated maximum possible coverage for $FcC_{11}SH$. Chidsey et al.(107) estimated the maximum theoretical coverage of ferrocene monolayers, by approximating ferrocene moieties as a close-packed layer of 6.6 Ådiameter spheres, as 4.5×10^{-10} moles cm^{-2}. Rudnev et al.(108) reported a similar discrepancy in the calculated $FcC_{11}SH$ surface concentrations. The larger value of Γ for the ferrocene SAM compared to the theoretical value has been attributed to the charge contributions from the ClO_4^- counter-ions in the redox peaks.

The cyclic voltammetry of 1% is not included in Figure 5.1. The 1% and 10% $FcC_{11}SH$ SAM shows a single redox feature, with the formal potentials at ∼ 0.200 V and ∼ 0.231 V, respectively. The single redox feature is indicative of kinetic homogeneity in these highly diluted ferrocene layers. With higher surface concentration of ferrocene, two distinct redox peaks are evident in the CVs of 25%, 50% and 100% $FcC_{11}SH$. As seen in CVs in Figure 5.1, the second redox peak appears at more positive potentials relative to the first peak. The ferrocene peaks at the lower potential region is labelled as A/C and the second redox couple as A'/C'. Literature on electrochemical studies of ferrocene systems attributes the formation of two sets of the redox peak to "densely-packed" and "isolated" ferrocene moieties as depicted in Figure 5.1(b) and (c), respectively.(108) With increasing $FcC_{11}SH$ fraction in the mixed monolayer, the A'/C' peak current increases, which shows the formation of large terraces of densely-packed $FcC_{11}SH$ fractions on the Au surface. The desorption of the ClO_4^- counter ions during reduction scan, contributes to a higher current at the first reduction peak compared to the second reduction peak in the CV of 100% $FcC_{11}SH$. It is also noted that the redox potentials for the A/C moieties tend to shift towards more positive potentials with the increasing fraction of $FcC_{11}SH$ in the monolayers. In contrast, the A'/C' redox moieties remain at the same redox potentials. The positive potential shift of the isolated moieties' redox peaks indicates that more ferrocene units are added to the isolated A/C colonies which asserts a better packing order to these loose molecular structures. The average peak current intensity ratios for the A/C and A'/C' moieties are estimated as 1.15±0.17 and 0.89±0.06, respectively. It shows that irrespective of the packing density of both the A/C and A'/C' moieties are electrochemically reversible. All the ferrocene SAM systems showed a comparable double-layer capacitance at the lower potential region. However, SAM layers with a larger fraction of $FcC_{11}SH$ show a noticeable increase in the capacitance at the oxidation potentials. This is due to an increased co-adsorption of ClO_4^- counter-ions to the larger fraction of the ferrocenium cations.

5.3.2 SEIRAS of $FcC_{11}SH$ with $C_{10}D_{21}SH$ diluents

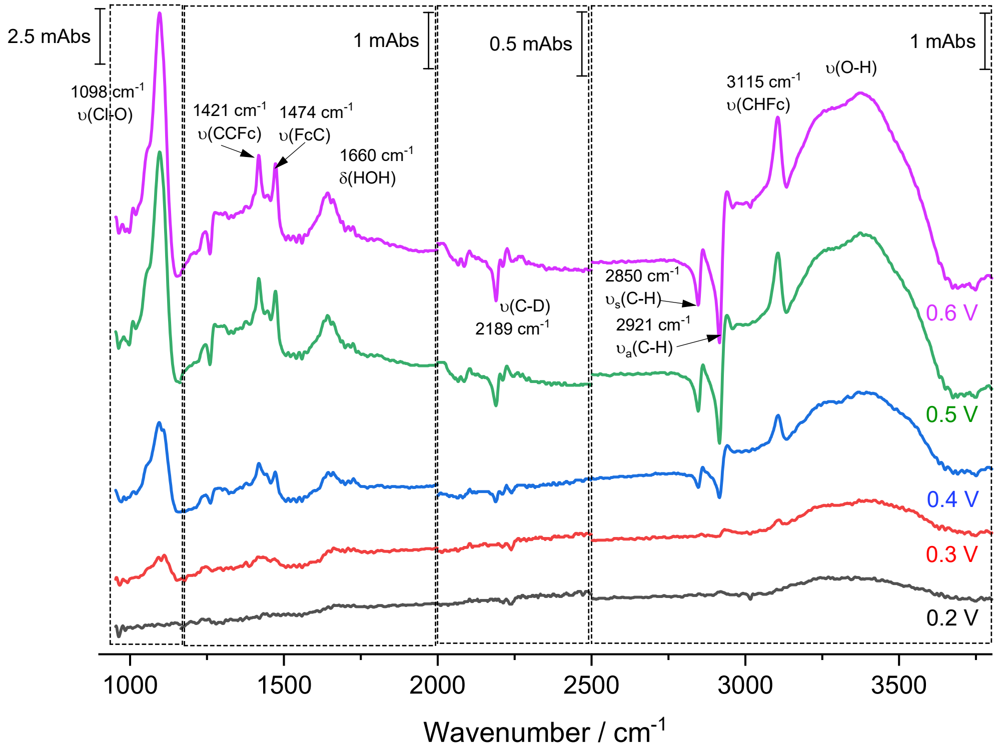

Figure 5.2: Potential dependent SEIRAS spectra of the mixed monolayers of $FcC_{11}SH$ and $C_{10}D_{21}SH$ (1:1 ratio), in 0.05 M $KClO_4$ electrolyte

Based on the voltammetric analysis of the different fractions of $FcC_{11}SH$ and $C_{10}SH$, monolayers with 50% $FcC_{11}SH$ showed a good distribution of isolated and close-packed ferrocene moieties. Also, a higher surface concentration of the redox centres and the diluent monolayers are favourable to generating SEIRAS spectra with a sufficient signal-to-noise ratio. Therefore, 50% $FcC_{11}SH$ mixed monolayers were chosen as a suitable system for SEIRAS experiments. The deuterated diluent, due to higher reduced mass than its hydrogen-substituted counterpart, shows a difference in its C–H bond stretching frequencies. Therefore, the vibrational bands of the deuterated diluent are shifted to a lower wavenumber. In the SEIRAS substrates with mixed monolayers, the C–D stretching mode at 2190 cm^{-1} can be used to track the ET-induced structural changes of the diluent monolayers. The electrode potentials to record SEIRAS spectra were chosen based on the CV features of the ferrocene-mixed monolayer. The sample spectra were recorded at every 0.05 V interval between 0.2 V and 0.6 V (Figure 5.2), and the reference spectra were collected at 0.05 V, where all the ferrocene moieties were in the reduced form.

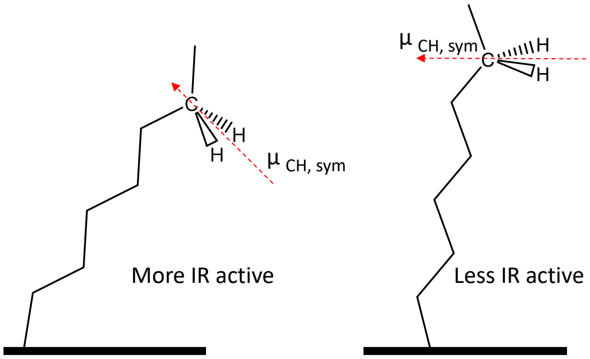

Figure 5.3: Schematic representing the transition dipole moment (μ) of the CH stretching modes in the tilted and upright orientations of alkane chains

According to the surface selection rules, vibrational bands corresponding to the molecular vibrations with an oscillating dipole moment parallel to the surface are suppressed in the SEIRAS spectrum. Therefore, not all IR active modes appear in the SEIRAS spectrum.(90) The three positive-going peaks that evolve with increasing potentials are at 1421, 1474 and 3115 cm^{-1}. The peak at 1421 cm^{-1} originates from the C-C stretching of the ferrocene ring υ(CCFc) and the 1474 cm^{-1} could have contributions from the bending mode of the methylene group, δ(HCH) and Fc–C stretching mode, υ(FcC). The positive peak at 3115 cm^{-1} belongs to the C–H stretching mode of the ferrocene ring, υ(CHFc). The two negative peaks at 2921 and 2850 cm^{-1} are assigned to the asymmetric and symmetric C–H stretching of the methylene groups of the $\mathrm{FcC_{11}SH}$. The potential dependent downward growth of these two peaks (υ_s(C–H) and υ_a(C–H)) are related to the structural changes of the alkyl bridging unit during the oxidation of the ferrocene centres (5.3. According to Ye et al.(109), the positively charged substrate is expected to exert a repulsive force on the ferrocenium moieties, which leads to an upright orientation for the alkyl bridging units with respect to the Au surface. A decrease in the absorption of the υ_a(C–H) mode of the methylene group confirms the assumptions about the reordering of the ferrocene chains during the redox process. A potential dependent increase in the C–H absorption of ferrocene,υ(CHFc) at 3115 cm^{-1} indicates rotation of the ferrocene moieties along the Fc–

C bond such that the plane of the cyclopentadienyl rings become perpendicular to the Au surface. The downward peak at 2189 cm^{-1} is assigned to the C–D stretching band of the diluent alkane chains. The potential dependency of the υ(C–D) provides structural evidence about the effect of reorientation of the ferrocene-substituted alkane chain onto the diluent monolayer structures. Apparently, the diluent alkane chains change the inclination angle to a perpendicular position, in order to accommodate the molecular motion of the FcC$_{11}$SH units.

The broad feature between 3100–3600 cm^{-1} belongs to the O–H stretching, υ(O–H) of water and the band at ~ 1640 cm^{-1} belongs to the H–O–H bending, δ(H–O–H) of surface adsorbed water molecules. Peaks at ~ 3250 and ~ 1640 cm^{-1} are attributed to the interfacial hydrogen bonded water molecules that coexist with the isolated water molecules (υ(O–H) at ~ 3400 cm^{-1}). The degree of water penetration into the SAM layer depends on the hydration energies of the anions. The rise of a very strong absorption peak at around 1095 cm^{-1} with increase in oxidation potential belongs to the ingress of the perchlorate ions υ(Cl-O) to the redox centres.

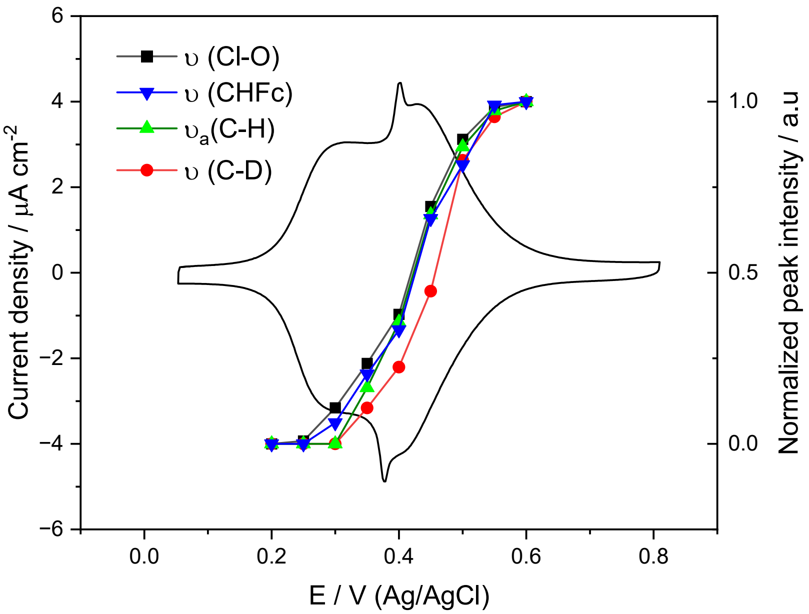

Figure 5.4: Comparison of the SEIRAS peak intensities and the CV of the corresponding SEIRAS layer with the (1:1) mixed monolayers of FcC$_{11}$SH and C$_{10}$D$_{21}$SH. The distinct sharp feature of the CV indicates the quasi-crystallinity of the SEIRAS film

Figure 5.4 is a comparison of the electrochemical behaviour of the FcC$_{11}$SH and C$_{10}$D$_{21}$SH (1:1) SAM on an Au-ITO film, with the structural information obtained from the SEIRAS spectra. The CV of 50% FcC$_{11}$SH SAM on the Au-ITO film in HClO$_4$ exhibits a sharp feature at around 0.4 V. The crystalline features of the substrate influence the packing density of the SAM layer. Studies of FcC$_{11}$SH SAM on Au single crystal electrodes by Rudnev et al.(108) reported the evolution of a sharp pair of redox peaks in addition to the two sets of redox peaks. Rudnev attributed these distinct, sharp pair of redox peaks in the CVs of ferrocene SAM to the formation of locally ordered domains of ion-pairs between ferrocenium and ClO_4^-. In the present study, the SEIRAS layer preparation via electrodeposition of Au on ITO, by the potential cycling method, could have formed large Au (111) terraces. The change in the intensities of all the four bands (υ (Cl-O), υ(C–D), υ_a(C–H) and υ(CHFc)), in Figure 5.4, corresponds to various molecular events during the redox process of ferrocene SAM. It is noticeable that all bands are not equally sensitive to potential change. Upon oxidation, the υ(Cl-O) band begins to rise at around 0.25 V, the potential region corresponding to oxidation of the isolated and disordered $FcC_{11}SH$ monolayers. The υ(CHFc) peak starts to evolve at the same potential region, whereas υ(C–D) and υ_a(C–H) peak intensities are insignificant. This observation bodes well with the assumption that at the low oxidation potentials, the ClO_4^- reaches the vicinity of ferrocene redox centres, and pairs with the ferrocenium cations, that are formed at the isolated and disordered $FcC_{11}SH$ monolayers. During this oxidation process, the ferrocene ring undergoes rotation without interrupting the orientation of alkane bridging units and the diluent monolayers. At the higher oxidation potentials ($\sim$ 0.4 V onwards), the ferrocene centres in the rigid alkanethiol layer undergo oxidation during which, both the rotation of ferrocene rings and reorientation of alkane chains occurs. Another noticeable feature in Figure 5.4 is that the rise of the υ(C–D) peak intensity is systematically offset to more positive potentials compared to the other three peaks, which indicates reorientation of the diluent molecules requires a larger driving force during the oxidation of ferrocene SAM. A schematic representation of the molecular events that are proposed based on the electrochemical and SEIRAS analysis is given in Figure 5.5. With stronger spectral evidence, the predicated model agrees with the structural model for the redox process of the ferrocene monolayer suggested by both Rudenev et al.(108) and Viana et al.(110). In addition, the present studies provide insights into the structural response of the diluent molecules to the redox process. During the potential step for the EC-SEIRAS measurements, the isolated Fc moieties experience a higher overpotential compared to its close-packed counterparts. Therefore, the molecular events during the oxidation of isolated Fc moieties occurs at much faster rate. In the absence of any distinctive SEIRA spectral features at the lower oxidation potentials, its is suspected that isolated Fc moieties undergoes similar molecular processes similar to closed packed Fc entities, as shown in Figure 5.5.

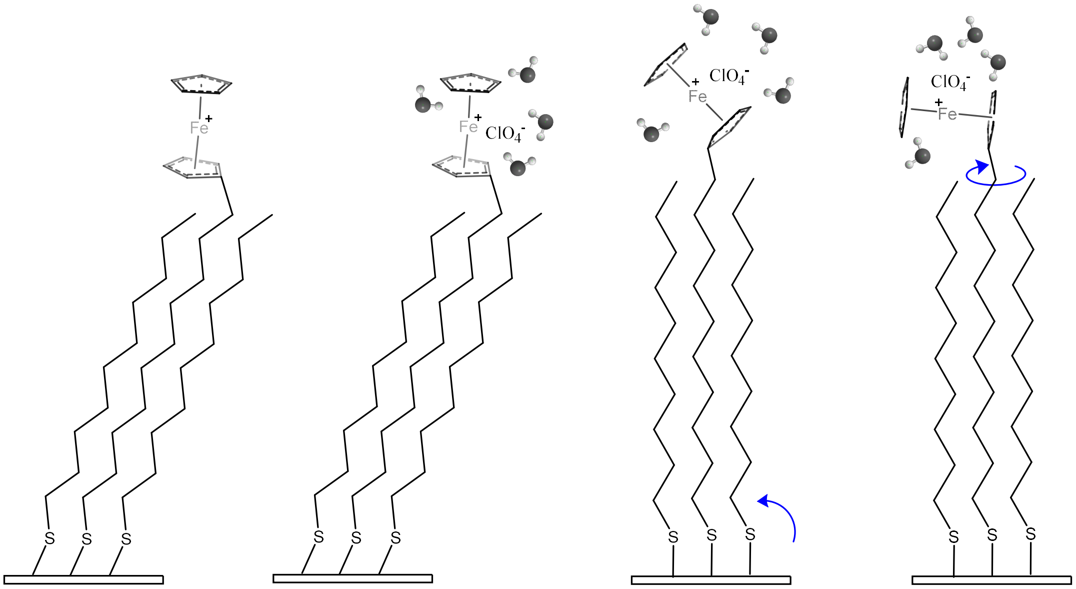

Process 1:
Electron transfer

Process 2:
Ion pairing/water ingress

Process 3:
Chain reorientation

Process 4:
Ring rotation

Figure 5.5: Predicted model showing various stages of molecular events during the oxidation of mixed monolayers of $\mathrm{FcC_{11}SH}$. Process 1: conversion of ferrocene to ferrocenium ion ($\mathrm{Fc^+}$) during the electron transfer, Process 2: ion pairing to stabilize the charged redox moiety and the ingress of water molecules towards the electrode interface, Process 3: reordering of the bridging units and adjacent diluents to an upright position, and Process 4: rotation of the ferrocenium moiety along Fc–C bond. Time-resolved EC-SEIRAS analysis is required to identify the sequence of these molecular processes

5.3.3 Time-resolved SEIRAS studies of the $FcC_{11}SH + C_{10}SH$ mixed monolayers with different anions

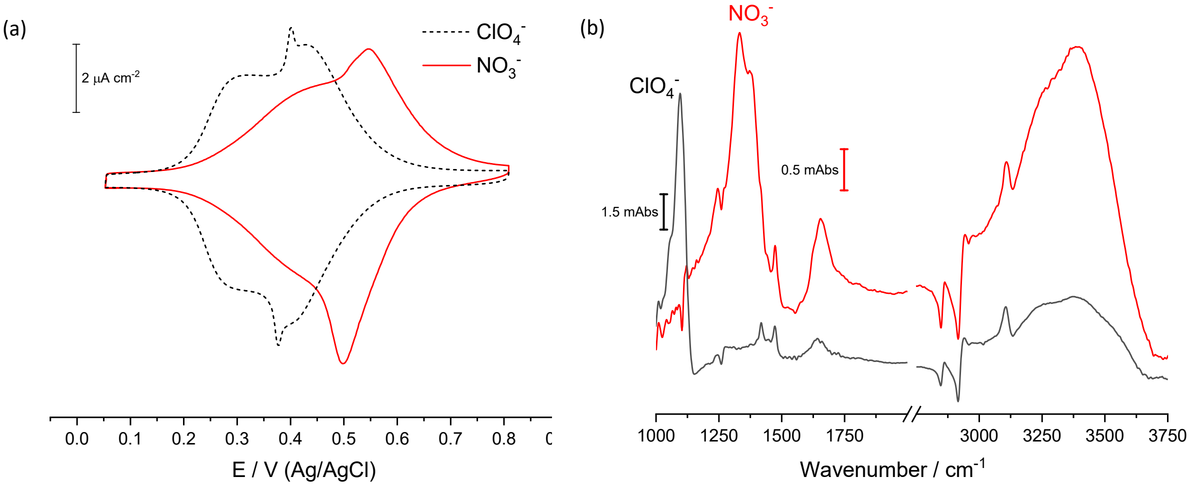

Figure 5.6: Comparison of the effect of ClO_4^- and NO_3^- as counter-ions on (a) the CVs and (b) the SEIRAS spectra of $FcC_{11}SH + C_{10}SH$ mixed monolayer. The potential dependent SEIRAS spectra is collected between 0.05 V as base potential and 0.45 V for ClO_4^- (0.55 V for NO_3^-)

In this section, the effect of hydrophobic and hydrophilic anions (ClO_4^- and NO_3^-, respectively) on the redox behaviour of $FcC_{11}SH + C_{10}SH$ mixed monolayer is studied using time-resolved SEIRAS. Initially, the electrochemical features of the ferrocene system in both electrolytes (0.1 M $HClO_4$ and 0.1 M HNO_3) are compared in Figure 5.6(a). The kinetic inhomogeneity due to multiple packing densities of the $FcC_{11}SH + C_{10}SH$ mixed monolayers is observed in both CVs. Apparently, the sharp redox features in the CVs due to the low crystal indices are unique to hydrophobic anions. A positive potential shift in the redox potentials of ferrcoene SAM system with NO_3^- counter-ions is due to the strongly bound solvation shell around the hydrophilic anions that interrupts the ion paring with the redox centres.

Figure 5.6(b) compares the SEIRAS spectra of $FcC_{11}SH$ mixed monolayers with two different anions. The spectrum with NO_3^- counter-ion shows two bands at $\sim$1332 and $\sim$1375 cm^{-1}. and these are assigned to the N–O stretching modes. The υ(N-O) peak at 1375 cm^{-1} overlaps with the υ(FcC) peak at 1421 cm^{-1}. Compared to the spectrum with ClO_4^- anions, the peaks from δ(H–O–H) and υ(O–H) at $\sim$ 1660 and 3100–3600 cm^{-1} are much more pronounced in the spectrum with NO_3^- counter-ions. This observation supports the inference from the CVs, that the hydrophilic anions brings more interfacial water molecules into to the SAM by maintaining an intact solvation shell. The υ(O–H) peak at around 3400 cm^{-1} belongs to hydrogen bonded interfacial water molecules in the case of NO_3^-. Meanwhile, in the case of ClO_4^-, the additional peaks like υ(O–H) around 3500 cm^{-1} confirm the presence of isolated and the hydrogen bonded water molecules at the interface.

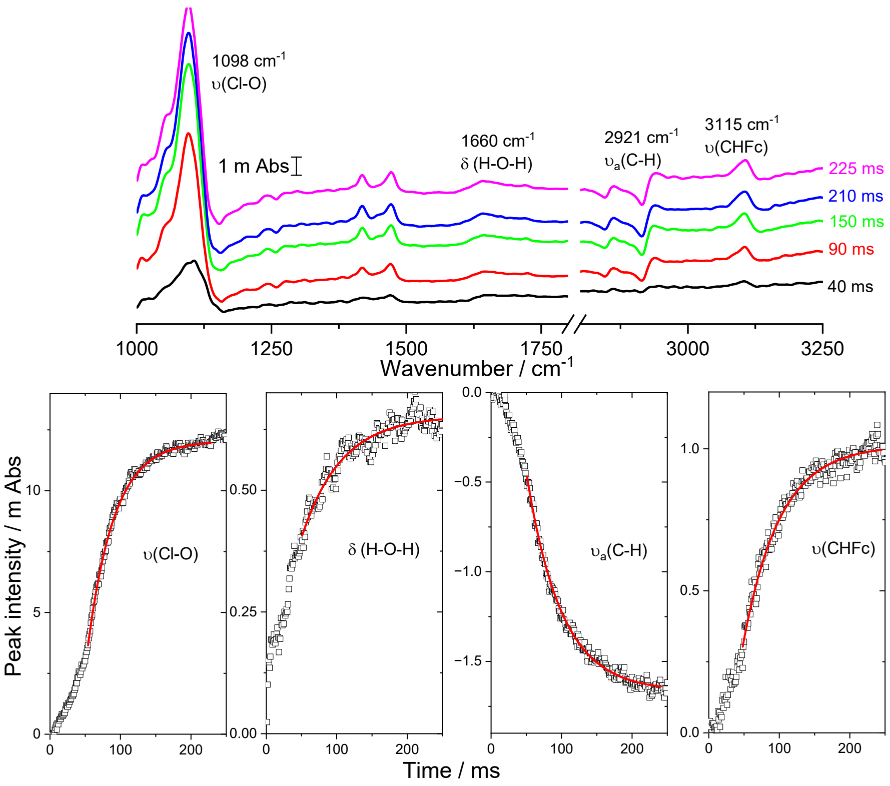

Figure 5.7: Time-resolved SEIRAS spectra (step scan) of the mixed monolayers of $FcC_{11}SH$ and $C_{10}SH$ (1:1 ratio), in 0.05 M $KClO_4$. Spectra are collected between 0.45 V (sample potential) and 0.05 V (base potential)

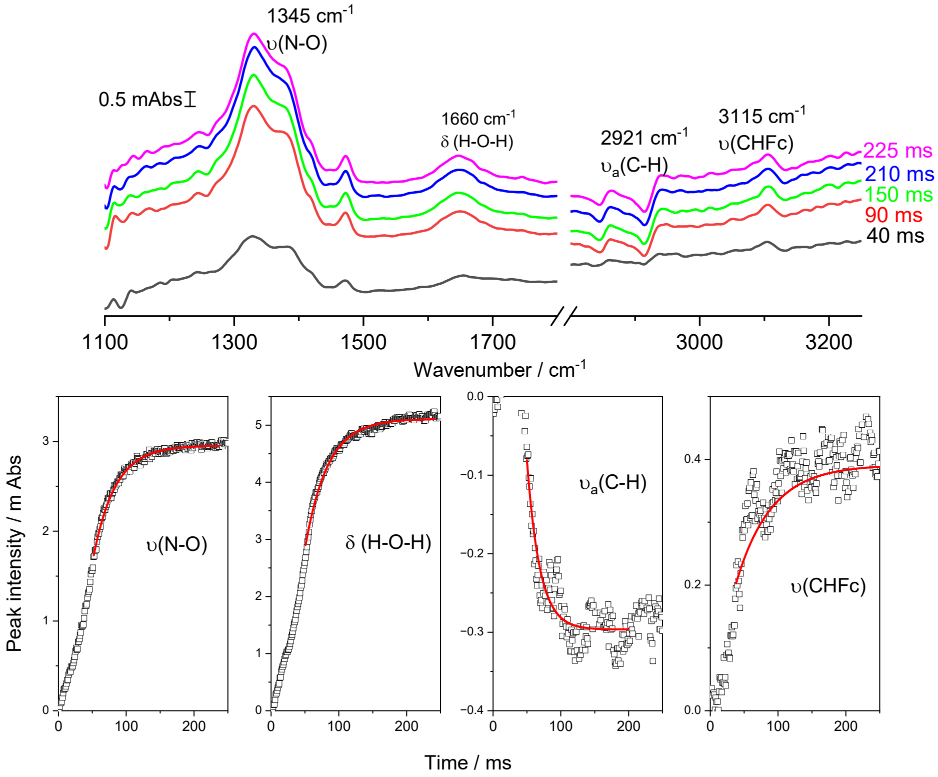

Figure 5.8: Time-resolved SEIRAS spectra (step scan) of the mixed monolayers of $FcC_{11}SH$ and $C_{10}SH$ (1:1 ratio), in 0.05 M KNO_3. Spectra are collected between 0.55 V (sample potential) and 0.05 V (base potential)

This section discusses the kinetics of the interfacial molecular events including the coadsorption of anions, ingress of the water molecules and the reorientation of the ferrocene moieties. Time-resolved FT-IR measurements are performed using the step-scan procedure (refer to Section 4.3.2 for details), at the potential steps between 0.05 V (base potential, E_{Ref}) and the formal potentials for the oxidation/reduction at the closely packed Fc units (0.45 V and 0.55 V, in $KClO_4$ and KNO_3, respectively). The step scan spectra are calculated at one-millisecond resolution. Sample spectra from the step scan measurements for ferrocene mixed monolayer system with ClO_4^- and NO_3^- are shown in Figure 5.7(a) and 5.8(a), respectively. The time-resolved measurements were initially performed with deuterated diluents $C_{10}D_{21}SH$ to follow the kinetics of adlayer, however the υ(C–D) signal intensity deteriorated during the time-resolved SEIRAS measurements. Rate constants are obtained from the peak intensity plots, by fitting the data to an exponential function $Abs = A + \exp(\frac{-t}{k})$ as shown as the red traces in Figure 5.7(b) and 5.8 (b). The value of k was taken as the inverse of the rate constant. To avoid interference from double-layer charging, data points at the first 40 milliseconds were excluded, and the remaining transient were fitted to a simple exponential function. The calculated rate constants for various peak intensities are provided in Table 5.2.

In the case of ClO_4^- as the counter-ions, all four signals are rather close in the rate constants. Within

Peaks	**Wavenumber / cm^{-1}**	**Rate constant, k / s^{-1} in $KClO_4$ (0.05 M)**	**Rate constant, k / s^{-1} in KNO_3 (0.05 M)**
υ(Cl-O)	1098	26.5 ± 0.3	–
υ(N-O)	1345	–	30.9 ± 0.5
δ(H–O–H)	1660	18 ± 1	30.2 ± 0.6
υ_a(C–H)	2921	20.3 ± 0.3	53 ± 5
υ(CHFc)	3115	19.2 ± 0.5	19 ± 2

Table 5.2: Apparent rate constants for the various peak evolution, obtained from the step scan data of $FcC_{11}SH$ mixed monolayers given in the Figures 5.7 and 5.8

the error, there is no evidence that the H_2O ingress, Fc backbone tilt change and the C-Fc rotation occur at anything but at concomitant rates (at least within 1-millisecond temporal resolution). There is, arguably, some evidence that perchlorate ingress happens faster (26.5 ± 0.3 s^{-1}). This may be caused by a rapid accumulation of the hydrophobic counter-ion as part of the double-layer charging process. Comparatively lower k values for δ(H–O–H) (18 ± 1 s^{-1}) reveal that the presence of hydrophobic counter-ions at the interface slows down the movement of the hydrogen-bonded water molecules at the interface. Meanwhile, the hydrophilic nature of NO_3^- makes it strongly solvated and remains outside the SAM when the monolayer is in its reduced state. Double-layer charging more than likely involves the movement of ions in the diffuse part of the double layer beyond the probing volume of the surface enhanced field. Closer values of k for υ(CHFc) in both sets infer that the hydrophilicity of the electrolyte has little contribution to the potential dependent molecular reorientation of the redox layer. The larger overpotential is needed to drive a re-orientation of the backbone toward a more upright alignment. ET is distinctively linked with the accumulation of solvated NO_3^- at the interface. The Fc rotation proceeds only after the Fc is oxidized and electrostatically stabilized by a solvated NO_3^- ion. Due to a 0.1 V shift in the formal potential, a larger overpotential was applied for the oxidation of $FcC_{11}SH$ SAM in NO_3^- compared to ClO_4^-. This potential drive is the important factor for higher rate constant values of water ingress in the case of NO_3^- compared to ClO_4^-.

5.3.4 Potential dependent SEIRAS study of amide coupled ferrocene-alkanethiol SAM

As stated earlier in this chapter, Fc-SAM is a widely studied redox system in literature. However, in most cases the electrochemical and spectral features of Fc-SAM systems were distinctively different.(108; 110; 109) Apparently, the degree of order of the alkyl chain as well as the distribution of ferrocene at the terminal layer of SAM can significantly increase the kinetic heterogenity of ferrocene-substituted alkanethiol SAM. Lack of consistency in the redox behaviour of the Fc-SAM is a challenge, especially when the electrochemical and spectral analysis requires repeated measurements. Moreover, kinetic valuation from such system will be inaccurate since the electron transfer theories (BV and MHC) are formulated for kinetically homogeneous systems. A better strategy to obtain well ordered adlayer and homogeneous distribution of Fc moieties at the SAM surface, and thereby consistently performing ferrocene-SAM modified electrode would be immobilizing the ferrocene moieties on a pre-fabricated alkane SAM terminals. Carbodiimide cross-linking reaction is a prominent method to immobilize biomolecules through its amine functional group to ω-alkanoic acid SAM modified substrates.(111) Interestingly, Viana et al (110) mentions the lack of agreement on the redox-induced orientational changes of between ferrocene-alkyl SAM with and without carboxylate ($FcCOO(CH_2)_{11}SH$ and $Fc(CH_2)_{11}SH$).

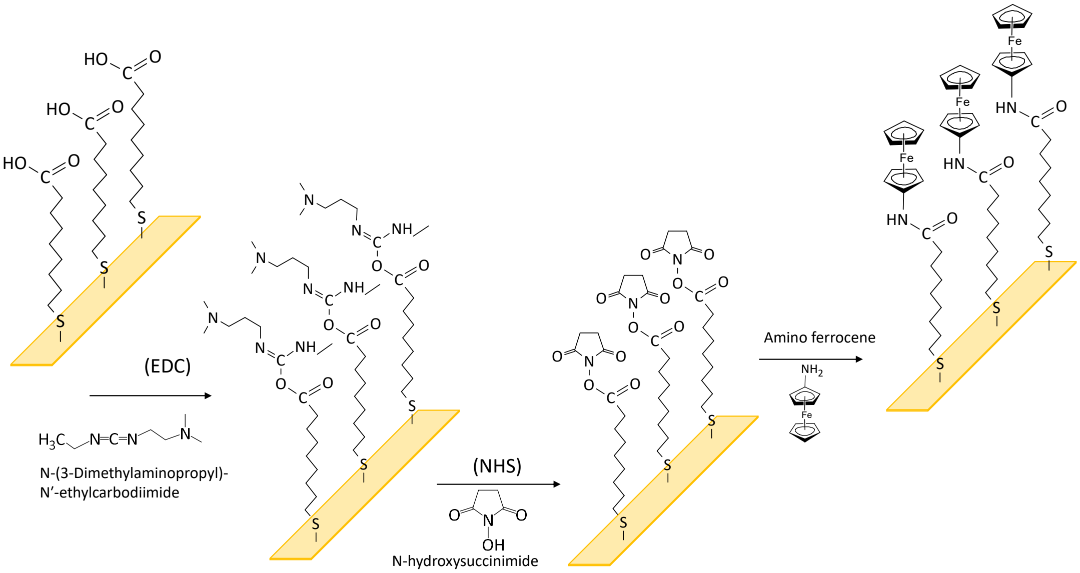
(EDC)
N-(3-Dimethylaminopropyl)-
N'-ethylcarbodiimide
(NHS)
N-hydroxysuccinimide
Amino ferrocene

Figure 5.9: Schematic representation of covalent bonding of amino-substituted ferrocene to the COOH-terminals of preformed alkanethiol SAM, via amide-coupling reaction

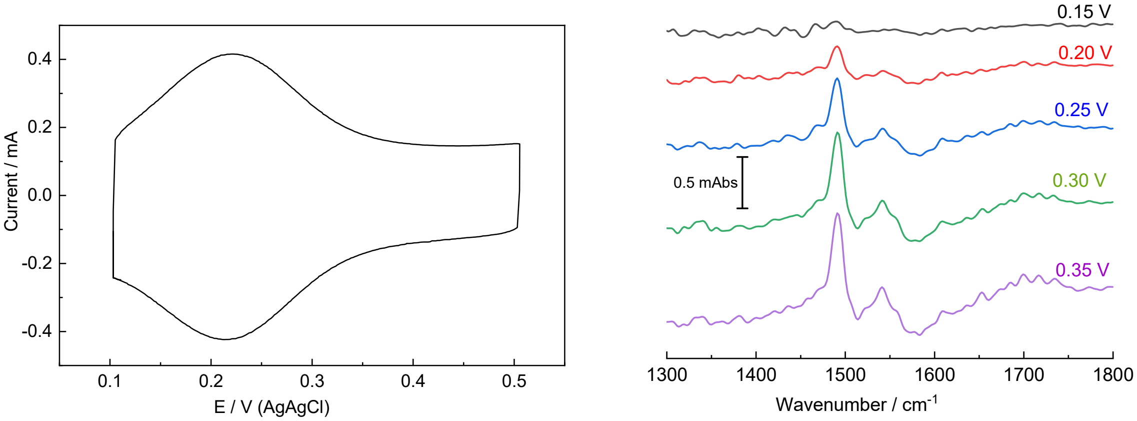

Figure 5.10: (a) CV and (b) the potential dependent SEIRAS spectra of amide coupled ferrocene-$NHCO_2$ $C_{16}SH$ SAM on Au-ITO layer

To explore the redox behaviour of well-ordered Fc SAM and to analyse the influence of functional groups containing alkyl chain to the redox induced molecular reorientation, amine-substituted ferrocene molecules were chosen to append with hexadecanoic acid SAM, via EDC/NHS amide coupling reaction (Figure 5.9. The measurements were collected in 0.1 M $HClO_4$ electrolyte. The single redox peak in the CV given in the Figure 5.10(a) shows kinetic homogeneity due to the formation of isolated (non-interacting) ferrocene centres coupled to a well-ordered alkane thiol SAM. However, the low current signifies the low coverage of ferrocene centres. The electrochemical stability of these redox films was not sufficient to carry out the kinetic measurements. The SEIRAS spectral features of Fc-$NHCOC_{16}SH$ SAM given in Figure 5.10(b) is distinctively different from the SEIRAS spectra of $FcC_{11}SH$ SAM in Figure 5.2. The peak at 1493 and 1540 cm^{-1} were the only two peaks observed in the spectral window between 1000 and 4000 cm^{-1}. IR spectroelectrochemical studies of the carbonyl-substituted ferrocene SAM $(FcCOCH_2)_9SH$ shows a positive band at around 1455 cm^{-1} and is assigned to the stretching mode of C=O.(110) Even though the peaks in the SEIRAS spectra in Figure 5.10(b) are reproducible and shows a potential dependency in the redox region shown in Figure 5.10(a), the overall spectral window lacks enough details to any draw conclusions. The absence of signals from the ferrocene moieties in the SEIRAS spectra is accounted for low ferrocene coverage. Therefore, EDC/NHS reaction conditions has to be fine-tuned for a better coupling efficiency of amine-substituted redox moieties to the -COOH substituted alkanethiol SAMs.

5.4 Conclusion

This chapter presents a comprehensive electrochemical and SEIRAS study of ferrocene terminated electroactive SAM, specifically the structural response of the diluent molecules in the mixed monolayers and the influence of hydrophilicity of the anions in the redox process. The CV analysis supports the findings of earlier studies about the formation of isolated and densely packed ferrocene monolayers. The influence of substrate morphology as well as the nature of electrolytes on the electrochemical behaviour of ferrocene layers were demonstrated and discussed in details. Deuterated alkanethiols were used as the SAM diluents in the SEIRAS studies to track the potential dependent molecular reorientation of alkyl chains adjacent to the ferrocene redox centres. The SEIRAS spectral features of the ferrocene moieties, counter-ions and the interfacial water molecules were identified and compared with the literature. The CV features and the SEIRAS data were correlated to obtain the detailed picture of the molecular events during the oxidation of ferrocene moieties in the mixed monolayers. With compelling data, the predicated molecular model agrees with many features of the two other published models of redox process in the ferrocene SAM, which expects the rotation of the ferrocene moieties along the Fc–C bond and the rotation of the linkage chain itself. The present model provides more details to the molecular events associated with oxidation process of mixed monolayers of ferrocene SAM such as the effect of reorientation of the ferrocene molecules to the adjacent diluent layers. Another highlight of this chapter was the time-resolved SEIRAS study in the two different (hydrophilic and hydrophobic) supporting electrolytes. Kinetic data estimated from the time-resolved spectra of ferrocene SAM provided more details on the molecular events occurring at the electrode interface. It includes the rate at which the counter-ions, hydrogen bonded water molecules, and reorientation of the ferrocene moieties in two different electrolytes.

Homogeneous sites of ferrocene-alkanethiol SAM is more suitable for the systematic study of electron transfer kinetics as well as the time-resolved SEIRAS analysis. Attempts were made to couple the amine substituted ferrocene to a well ordered -COOH functionalized alkanethiol SAM layers. The CV features signified the presence of homogeneous redox sites for the ferrocene linked alkanethiol SAM layers. However, significantly low coverage of ferrocene resulted in low spectral quality for the SEIRAS analysis. Better insights into the mechanism of the EDC/NHS coupling reaction could prove room to improve the coupling efficiency and thereby control the ferrocene coverage on the preformed alkanethiol SAM layers.

6 Surface enhanced infrared adsorption studies of amide coupling reaction

Contributions All the experiments and result analysis, discussed in this chapter are solely conducted by Bipinlal Unni, under the supervision of Dr. Ian Burgess.

6.1 Introduction

Heterogeneous electron transfer (ET) kinetics are highly sensitive to the position of the electroactive moieties with respect to the electrode surface. Synthesis of molecular species containing redox functionality and suitable spacer units is a laborious process. Several protecting/deprotecting steps are typically required to covalently attach a redox-active moiety while still retaining a thiol headgroup suitable for self-assembly. Additionally, the conformational and steric effects of bulky head groups hinder the packing of the underlying spacer units. Inconsistent spacing between the reactant and electrode surface complicates the parameterization of ET kinetics. Covalent coupling of electroactive species to the chain terminals of pre-formed SAMs is an alternative method.(48) This strategy preserves the order of the underlying SAM structure. In addition, if the terminal end group of the SAM forming molecule has sufficient reactivity, a variety of interesting chemical and biological moieties can be chemically grafted to the electrode surface.

A wide variety of methods have been explored for covalently binding molecular subunits to SAM surfaces.(112) Preference to a specific method depends on factors such as selectivity of the terminal groups, stability of the reactive complex, compatibility of reaction conditions with the chemistry, and the efficiency of the coupling reaction. A large number of amine ($-NH_2$) substituted organic and organometallic ligands are commercially available or easy to synthesis. These ($-NH_2$) substituted ligands can be coupled via amide linkage to the exposed carboxylic acid (–COOH) group of ω-substituted alkyl SAMs.(113) Yan et al.(114) reported a method for the formation of interchain carboxylic anhydride as a reaction intermediate. The procedure involves dehydrating the terminal –COOH with trifluroacetic anhydride. The carboxylic anhydride reacts with alkyl amines to form an amide linkage, and results in a SAM surface composition of a 1:1 mixture of –COOH and –CONHR functional groups.

A popular method called the 'activated ester method' is widely used to anchor amine substituted molecules on carboxylic acid terminated SAM surfaces.(115; 116; 117) The method involves generating an active intermediate by treating the –COOH surface groups with *N*-hydroxysuccinimide (NHS) to form succinimide esters (NHS-ester), in the presence of a coupling agent like N-ethyl-N-(3-(dimethylamino)propyl) carbodiimide (EDC) (Figure6.1).(118) Despite the wide adoption of the activated ester method, no standard protocols describing the conditions such as concentrations of EDC and NHS, molar ratio of EDC/NHS and pH conditions, can be found in the related literature.

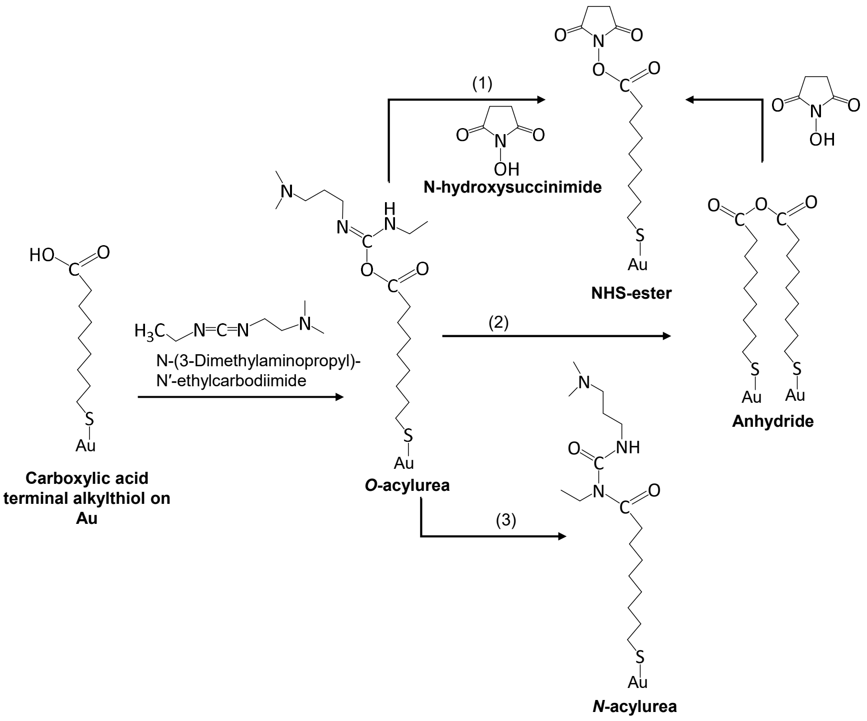
(1)
N-hydroxysuccinimide
NHS-ester
Carboxylic acid terminal alkylthiol on Au
N-(3-Dimethylaminopropyl)-N′-ethylcarbodiimide
O-acylurea
(2)
Anhydride
(3)
N-acylurea

Figure 6.1: Schematic representation of the activation of carboxylic acid by carbodiimide to form *O*-acylurea and (1) its reaction with NHS to yield NHS-ester, (b) formation of anhydride in the absence of NHS and (c) showing formation of *N*-acylurea via intramolecular acyl transfer (the reaction scheme is adapted from Reference(2))

The proposed surface EDC/NHS reaction mechanism is derived from the more thoroughly studied solution phase reaction and consists of NHS-ester formation in a two-step process. First, the carboxylic acid reacts with carbodiimide to form *O*-acylurea, which in turn reacts with NHS to yield an NHS-ester (reaction path 1 of Figure 6.1).(118) IR studies of EDC/NHS activation of acid terminals on porous Si by Sam et al.(119) reports subsidiary pathways for the ester activation process, which are mostly driven by the concentrations of EDC and NHS (reaction path 2 and 3 of Figure 6.1). According to their findings, at larger concentrations of EDC and NHS ($\approx$ 100 mM), *O*-acylurea generates a nonreactive byproduct identified as *N*-acylurea. Larger concentrations of EDC ($\approx$ 100 mM) with lower concentrations of NHS ($\approx$ 5–10 mM) generate unstable and reactive *O*-acylurea, which can be subsequently transformed along two pathways: (1) rapid reaction with neighbouring –COOH to yield anhydride along with urea release and (2) rearrangement via intramolecular acyl transfer to form *N*-acylurea. At conditions where both EDC and NHS concentrations are low, the reactions proceeds slowly to form the desired NHS-ester without forming byproducts. The study by Sam et al.(119) reports equimolar concentrations of EDC and NHS between 5–20mM as optimal for –COOH surface activation. IR reflection absorption spectroscopy and mass spectroscopy studies on EDC/NHS reaction on Au substrates conducted by Palazon et al.(2) supports these findings and reaction conditions suggested in the aforementioned literature. EDC/NHS reaction kinetics were studied using ATR-SEIRAS by Tsai et al.(120). This work emphasized the influence of pH conditions on NHS-ester formation. The pH dependence of EDC/NHS reaction with –COOH was described on the basis of the pKa values of the carboxylic acid SAMs and EDC. Deprotonation of –COOH terminals of SAM and protonation of EDC is essential to drive this reaction, which is expected to be maximal at pH 4–6.

Various studies within the scope of this thesis require redox-active SAM of various alkyl chain length. The EDC/NHS coupling reaction was chosen for the SAM surface activation and used to anchor amino-substituted electroactive probe molecules. Palazon et al.(2) studied the role of solvent and reactant concentration in EDC/NHS reactions using polarization modulation-IR reflection spectroscopy (PM-IRRAS) in combination with mass spectroscopy. Using ATR-SEIRAS, Tsai et al.(120) investigated the pH dependency of EDC/NHS reaction on –COOH terminals of SAM modified Au surfaces. With the available information in the above literature, the goal of this chapter is to demonstrate real-time monitoring of the EDC/NHS reaction with –COOH terminals of SAM modified Au surfaces. With the assumption that the applied potential can drive the kinetics of EDC/NHS reaction at the electrode surface, this study explores the various reaction intermediates formation and the preferred reaction pathways of NHS-ester formation under different electrode potentials.

6.2 Experimental Section

The reagents N-(3-Dimethylaminopropyl)-N'-ethylcarbodiimidehydrochloride (EDC), N-Hydroxysuccinimide (NHS) and the various mercaptoalkanoic acids (6-mercaptohexanoic acid (MHA), 8-mercaptooctanoic acid (MOA), 11-mercaptoundecanoic acid (MUA), 12-mercaptododecanoic acid (MDDA), and 16-mercaptohexa decanoic acid (MHDA)) were purchased from Sigma Aldrich and used as received. The polycrystalline gold electrodes were formed by melting a 0.5 mm diameter gold wire (99.99%) in a hydrogen flame. The bead is immersed in aqua regia and melted several times to remove surface impurities. After the final melt, the electrode is allowed to cool slowly in air. Electrodes formed in this fashion were cleaned prior to every experiment by immersion in freshly prepared piranha solution (3:1 H_2SO_4 and 30% H_2O_2) and gently flame annealed. –COOH terminated SAMs were prepared by immersing the cleaned gold bead electrodes in 5 mM solutions (95% ethanol as solvent) of the alkanoic acid thiols for four hours. After incubation, the electrodes were rinsed thoroughly with 95% ethanol and deionized water. The SAM layers were reacted with equimolar concentration (5 mM) of EDC and NHS for surface activation. A computer-controlled system, consisting of a HEKA PG590 potentiostat and custom software written in the LabVIEW environment, was used for all electrochemical analyses. An Ag/AgCl in saturated KCl was used as the reference electrode and a flame-annealed, coiled gold wire served as the counter electrode. 0.05 M $KClO_4$ was used as the electrolyte solution.

A 60^0 face-angled Si crystal (PIKE technologies) was used as the internal reflection element (IRE) for ATR-SEIRAS experiments. The principal reflecting plane of the IRE was polished with 3 and 0.5 micron diamond polishing solutions, rinsed with copious amounts of deionized water and air dried. Approximately 20 nm thick indium tin oxide (ITO) films were sputtered on the IRE surfaces using a home-built RF magnetron sputtering unit using a power of 30 W and a base vacuum of 4×10^{-5} Torr. The ITO sputtered IRE was annealed under vacuum at 300^0 C for an hour and then assembled in a Jackfish SEC J1 cell (Jackfish JEC). The ITO-coated Si IRE served as the working electrode for in-situ spectroelectrochemical experiments. SEIRAS active gold layers on the ITO surfaces were prepared by electrodepositing gold islands from an electrolyte containing 0.25 mM $KAuCl_4$ and 0.05 M $KClO_4$. The SEIRAS activity of electrodeposited Au film was monitored using 0.1 mM 4-methoxypyridine. After the cell was disassembled, the gold layer on ITO was rinsed thoroughly with deionized water, before the formation of the –COOH substituted alkane thiol SAM layer.

IR measurements were performed using a Bruker Vertex 70 FTIR spectrometer with a liquid nitrogen cooled, MCT detector. An in-house developed Labview program was used to control both the IR spectrometer and potentiostat. The IRE assembled SEC cell was mounted on a VeeMax III optic accessory (PIKE technologies), and the angle of incidence was set to 60^0. IR spectra were collected between 800 and 4000 cm^{-1} at 8 cm^{-1} resolution and 2 mm aperture. All spectra are expressed in absorbance units, defined as $A = -\log(I/I_0)$, where I and I_0 are the sample and reference single beam spectrum, respectively.

6.3 Results and Discussion

6.3.1 Real time monitoring of EDC coupling reaction using ATR-SEIRAS

ATR-SEIRAS spectra of EDC/NHS coupling reaction with MUA SAM at various time intervals is shown in Figure 6.2. Absorbance spectra are calculated using the MUA SAM on Au as a reference spectrum. Therefore, $\upsilon(CH_2)$ peaks from alkane chain at higher wavenumbers are not expected in the calculated absorbance spectra. Prominent peaks associated with the surface activation are observed in the lower wavenumber region. Spectra collected at the beginning (∼1 min) of the EDC/NHS reaction show a strong peak at 1709 cm^{-1}, which significantly loses intensity as the reaction proceeds. IR spectra of individual components in the reaction reveal that the presence of NHS at the Au surface is responsible for the 1709 cm^{-1} peak. NHS is consumed by reacting with *O*-acylurea, resulting in a drop in the peak intensity. The excess NHS is removed after rinsing, as indicated in the final spectrum. The characteristic set of three peaks at 1735, 1780 and 1811 cm^{-1} is assigned to the asymmetric and symmetric $\upsilon(C{=}O)$ modes of the carbonyl groups of the succinimide ring and the $\upsilon(C{=}O)$ mode of the ester unit, respectively.(120) Frey et al.(121) considered the first two peaks (1735, 1780 cm^{-1}) to arise from covalently bounded NHS to –COOH and not derived from the activated ester. However, the peak intensities remain unchanged before and after removing the excess reactants. This implies that all three peaks mentioned above belong to the surface activation process. A notable spectral

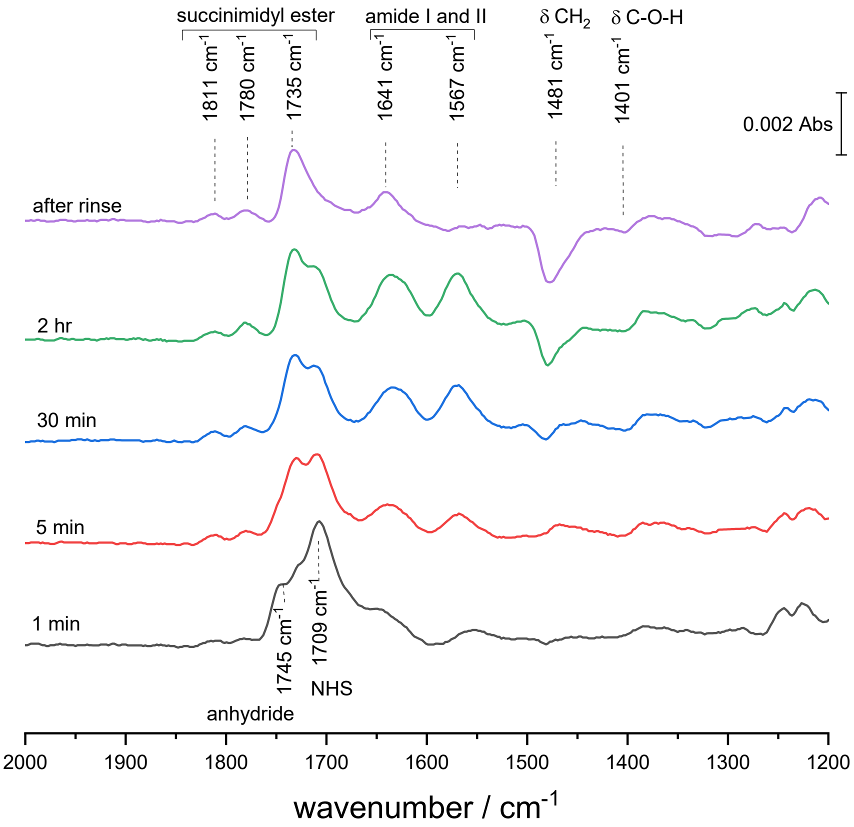

Figure 6.2: ATR-SEIRAS spectra of the EDC/NHS reaction on the MUA SAM modified Au surface

feature is the 1745 cm^{-1} peak, which is an evidence for reaction pathway 2 in Figure 6.1. The band at 1745 cm^{-1} in the initial spectrum disappears within 5 min of reaction. This short-lived peak belongs to anhydride formation, which converts to the ester in the presence of NHS. The short reaction time of the anhydride species is consistent with the literature on capacitive measurements of EDC/NHS reaction.(122) Formation of anhydride is the result of *O*-acylurea hydrolysis, which subsequently releases urea. The amide I and II peaks at 1641 and 1567 cm^{-1} are strong evidence of urea formation. Loss in the peak intensities of amide bands after rinsing the Au surface supports the above conclusion. A broad shoulder of the ester peak at 1735 cm^{-1} indicates the presence of a carbonyl stretching υ(C=O) peak at 1714 cm^{-1} from the unreacted acid group.(123) The downward going band at 1481 cm^{-1} associated with δCH_2 (scissor mode) of methylene groups, indicates molecular rearrangement of SAM layers during the reaction. The weak downward peak at 1401 cm^{-1} is attributed to δ(C–O–H) in plane mode, showing the involvement of –COOH in the reaction.

6.3.2 Potential dependence on EDC reaction kinetics

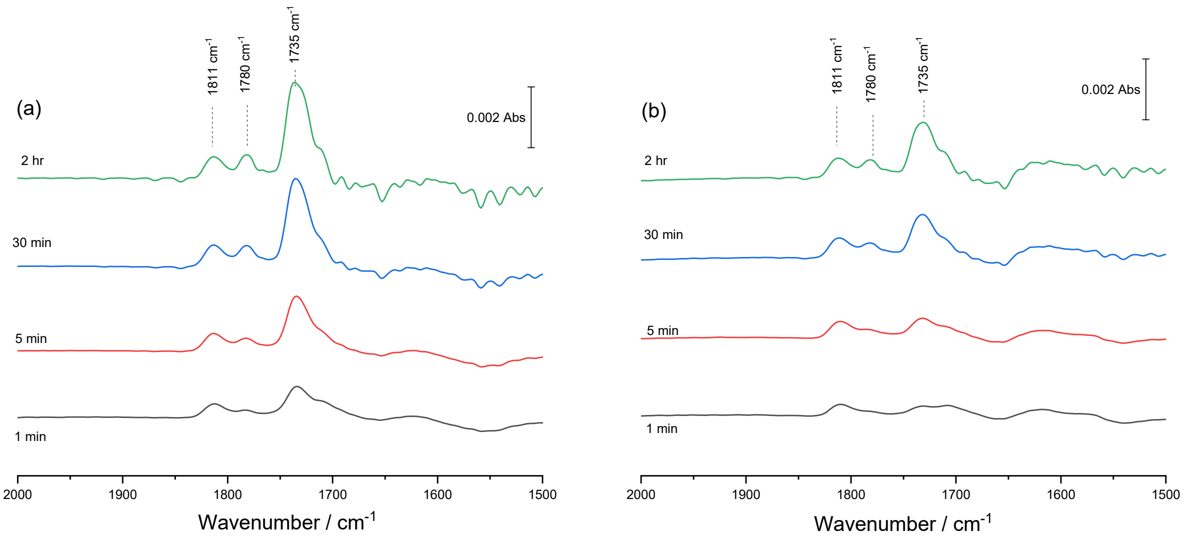

Figure 6.3: Potential dependent ATR-SEIRAS spectra of EDC/NHS reaction collected at (a) 500 mV and (b) -300mV

The amide coupling reaction proceeds through deprotonation of the carboxylic acid terminals and protonation of EDC.(120)(124) And, various studies have shown that the state of protonation of the ω-terminus of alkanoic acid SAMs can be controlled by applied potentials.(125) Therefore, it is hypothesised that the rate of the amide coupling reaction might be driven by altering the electrode potential. This section presents the reaction kinetics of EDC/NHS surface activation studied under potential control. ATR-SEIRA spectra of the reaction are collected at different potentials ranging from -300 and +500 mV. Figure 6.3 shows SEIRA spectra collected at two potential extremes. Significant difference in the growth of the characteristic succinimidyl and ester carbonyl peaks of the NHS ester (1735, 1780 and 1811 cm^{-1}) during the initial stage of reaction (within 10 minutes) among the potential dependent spectra indicates the reaction pathways can be altered by the electrode potentials.

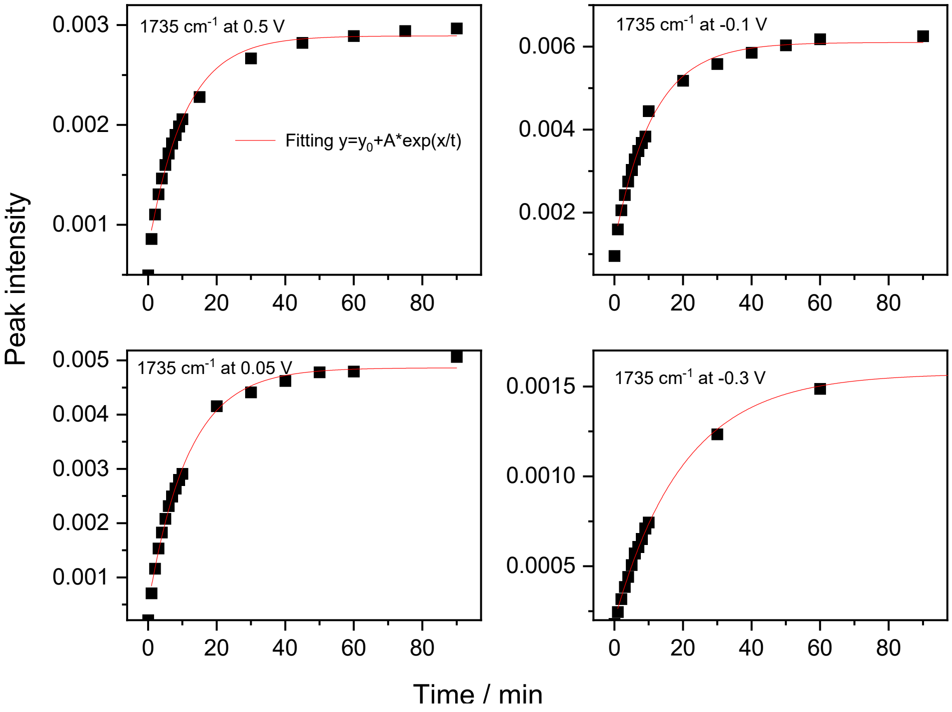

Figure 6.4: Fitted exponential functions to the plots of band intensities at 1735 cm^{-1} as a function of time, collected at various applied potentials

Kinetic analysis of the potential controlled EDC/NHS reaction was carried out by fitting an exponential function to the peak intensities of the band at 1735 cm^{-1} as shown in Figure 6.4. The data analysis was also performed on the other two major bands at 1780 and 1811 cm^{-1}. Figure 6.4 shows an excellent exponential fit ($R^2 > 0.99$) for the data points, denoting first-order kinetics for the EDC/NHS reaction. The time constant (k) values were obtained from the exponential fitting parameters for all three peaks. These estimated k values plotted with respect to the applied potentials are shown in Figure 6.5, and it reveals more details of the reaction pathways. The conversion of *O*-acylurea to the NHS-ester via pathway 1 occurs through a single step (Figure 6.1); hence it is expected to be kinetically faster compared to pathway 2. Figure 6.5 shows the rate of formation of the 1811 cm^{-1} peak is always faster among the characteristic peaks related to ester formation. Therefore, the kinetics of pathway 1 can be assessed by following the 1811 cm^{-1} peak. A sharp growth of 1735 and 1780 cm^{-1} peaks indicates faster consumption of NHS to form ester when the electrode potential becomes positive whereas, the peak at 1811 cm^{-1} shows a reverse trend. It infers that reaction pathway 1 is more favoured at negative potentials, whereas EDC/NHS reaction proceeds through pathway 2 at positive potentials. Contribution from a change in the molecular orientation of –COOH SAM with respect to the electrode potentials is also suspected to adopt different reaction pathways. The surface activated SAM

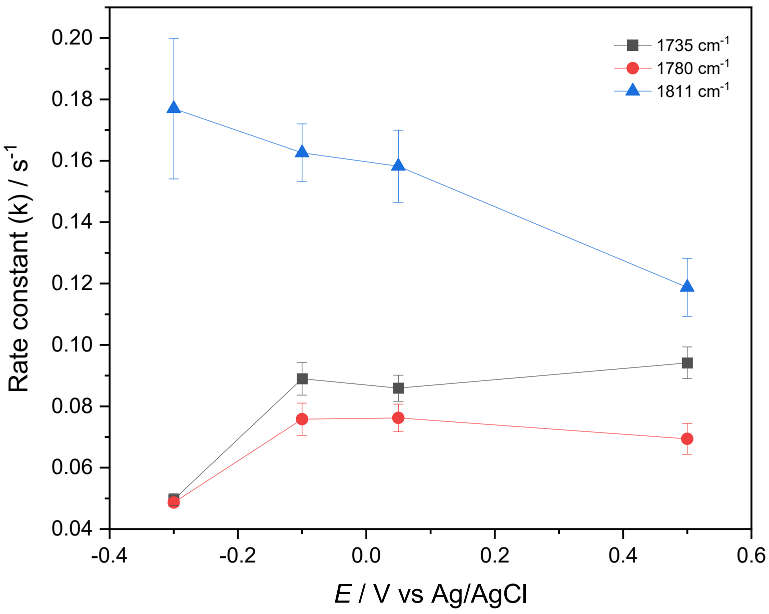

Figure 6.5: Plot showing rate constant of 1735, 1780 and 1811 cm^{-1} peaks as a function of electrode potential. The error bars are obtained from the fitting function

layers prepared under various applied potentials were allowed to react with amino-substituted redox molecules such as 4-amino TEMPȮ. However, no significant difference in the redox current densities were observed between these redox-active SAM layers. All the SAM layers showed comparable redox current densities, which indicates the number of active sites (succinimide-ester) formed on the electrode were independent of the applied electrode potentials.

6.4 Conclusion

Amine substituted chemical moieties tether spontaneously to the EDC/NHS activated –COOH terminals of ω-alkanoic acid SAMs. An in-depth understanding of the EDC/NHS reaction is required to design experiments for binding the amine-substituted redox species efficiently with SAM modified surfaces. This chapter discussed the formation of the activated layer during the EDC/NHS reaction, on a close packed alkyl SAM with –COOH termini. A brief literature review on various reaction pathways for EDC/NHS reaction were presented and the possible formation of the intermediate species were also discussed. The protonation of EDC and the deprotonation of carboxylic acid initiates the reaction to form *O*-acylurea, an unstable reaction intermediate. In the presence of equimolar concentrations of EDC and NHS, the activation reaction of carboxylic acid monolayers proceeded to form succinimide-ester, a stable intermediate that efficiently couple with the amine functional groups. The characteristic IR peaks at 1735, 1780 and 1811 cm^{-1} confirmed the formation of succinimide-ester. The EDC/NHS activation of carboxylic acid monolayers were monitored in real time using ATR-SEIRAS method, and the results showed evidence of direct and indirect pathways for the formation of succinimide-ester.

Increased number of activated sites on the SAM terminals potentially increases the number of redox moieties tethered to the electrode surface. Substrates packed with greater numbers of redox molecules can potentially improve the signal intensity during the SEIRAS measurement. As the EDC/NHS reaction is initiated by protonating and deprotonating of EDC and –COOH, respectively, this chapter explored the effect of applied potentials on the activation reaction. The findings were, the direct conversion of *O*-acylurea to succinimide ester occurred at faster rates at negative potentials with respect to the OCP and that the indirect conversion of *O*-acylurea to succinimide ester via anhydride formation is preferred at the positive potentials. The Au electrodes with activated ester-SAM surfaces, that were prepared under various applied potentials, were reacted with amine-substituted redox molecules. No significant difference was observed in the loading of redox centres onto the SAM terminals. This implies that the role of other factors such as steric hindrance, rather than the number of activated sites, controls the covalent binding of the redox centre to the electrode.

7 Electrochemical analysis of the TEMPȮ coupled alkanethiol monolayers

Contributions All the experiments and result analysis, discussed in this chapter are solely conducted by Bipinlal Unni, under the supervision of Dr. Ian Burgess. Some of the results discussed in this chapter are published in Electrochimica Acta 2021, 381, 138263.

7.1 Introduction

Electrochemical interfaces with surface confined electroactive molecules as functional probes find a great number of practical applications, such as energy conversion devices, electrocatalysis and advanced sensors.(126; 127; 128). Optimizing the performance of charge transfer processes across modified interfacial surfaces and obtaining insight about the mechanism of interfacial processes occurring under operando conditions, requires accurate measurement of kinetic parameters. Well-defined molecular films organized on an electrode surface limit the access of molecules (ions and electroactive species) in the electrolyte to the electrode surface. The presence of a dielectric film between the electrode and the electrolyte significantly drops the interfacial capacitance (as explained in the previous chapter). This phenomenon is beneficial as it enhances the faradaic current relative to charging current in the voltammetric method of analysis. As described in Chapter 2, fundamental theories of electron transfer (ET) relate the kinetics of ET to the thermodynamic driving force (overpotential). Experimental validation of theoretical predictions requires the ability to measure ET rates over a large span of overpotentials. Self assembled monolayers (SAMs) with large windows of potential stability allow such measurements.

Electrochemical methods generally employed for measuring kinetics in such systems are: cyclic voltammetry and chronoampherometry which are discussed in detail in previous chapters. The initial assumptions about the redox system bound to the electrode are: nerstian behaviour with no iR drop, no-double layer effects, constant transfer coefficient of 0.5 and uniform rate constant for all redox centres in the SAM. Peak potentials of kinetically controlled CVs are linearly dependent on the scan rate. When the electron transfer kinetics cannot keep up with faster scan rates, the system becomes irreversible and peak separation (ΔE_p) increases, which is the basis of the Laviron analysis.(106) This simplified approach is not applicable to all electrochemical systems and deviates from its predicted trajectory especially at larger overpotentials. Marcus-Hush-Chidsey (MHC) formalism provides a more advanced approach to obtain various kinetic parameters such as reorganization energy and rate constants.(39)

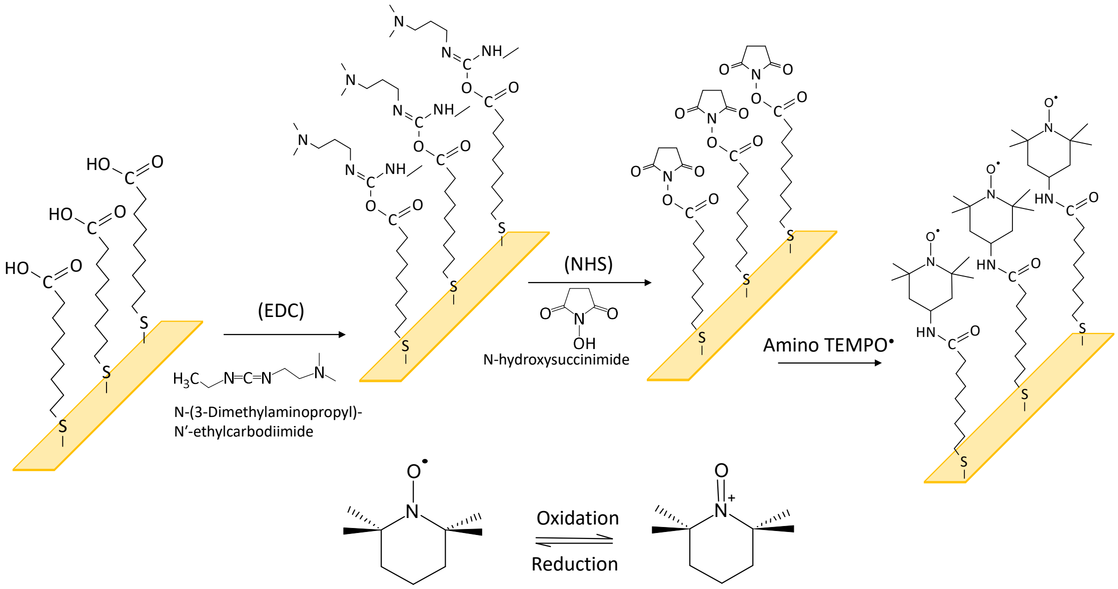

Figure 7.1: Schematic representation of covalent bonding of amino-substituted TEMPȮ to the COOH-terminals of preformed alkanethiol SAM, via amide-coupling reaction, and the redox structure of TEMPȮ/TEMPO$^+$ redox couple. Redox formal potential of TEMPȮ SAM is measured as ~0.690 V vs Ag/AgCl in 0.05 M $KClO_4$

Criteria for choosing the redox species to study the ET kinetics is important. The electrochemical sensitivity of SAM termini must be within the stable potential window of the SAM. Also, the redox moiety should not interfere with the tethering chemistry needed to link the redox centre to the rest of the SAM structure on the electrode surface. In this regard, dialkylnitroxyl radicals, exemplified as TEMPȮ (2,2,6,6-tetramethylpiperidine-1-oxyl free radical) is a suitable candidate (Figure 7.1). Organic free radicals are molecules with one or more unpaired electrons, hence they exhibit exceptional electronic and magnetic character. The stability of radicals is attributed to a combination of odd electron stabilization by the adjacent lone pairs or by delocalization and steric hindrance to prevent undesired reactions. Families of stable and persistent organic free radicals are employed for surface functionalization to explore their potential in versatile applications including spintronics (due to magnetic hysteresis), spin labelling (due to sensitivity towards paramagnetic spin resonance) and catalysis.(129; 130; 131). TEMPȮ and its derivatives are extensively used in synthesis as redox mediators, specifically for oxidation of primary alcohols. For example, TEMPȮ is employed to facilitate regeneration of transition metal catalyst (Ru and Cu) for the aerobic oxidation of alcohols via metal-centred dehydrogenation.(132) Self assembled TEMPȮ modified films on electrode surfaces has been explored for electrochemical applications such as 4-methylbenzyl alcohol oxidation and enantioselective oxidation of amines.(133; 134) Levillain et al. (135) extensively studied the electrochemical behaviour of $\mathrm{TEMP\dot{O}}$ tethered alkane thiol SAMs. Pre-synthesized $\mathrm{TEMP\dot{O}}$ coupled alkyl thiols (of various chain length) were used in these studies to modify the electrode surfaces. $\mathrm{TEMP\dot{O}}$ SAM with various surface coverage were examined, and high coverage was found to result in deviation from Langmuir character. This provided experimental evidence that was challenging to the Laviron interaction model.(136) [1] Finklea and Madhiri performed some of the first work on experimentally determined electron transfer rate constants and the reorganization energies of the $\mathrm{TEMP\dot{O}/TEMPO^+}$ redox couple.(83) Amino substituted $\mathrm{TEMP\dot{O}}$ molecules were surface confined by coupling to a pre-formed SAM layer of 11-mercaptoundecanoic acid and the measurements were carried out using CV analysis. Computational studies prior to Finkela's report estimated the total reorganization energy for $\mathrm{TEMP\dot{O}/TEMPO^+}$ to be 1.6-1.7 eV, with negligible difference between $\mathrm{TEMP\dot{O}}$ and $\mathrm{TEMPO^+}$.(137) Finkela's experimental analysis yielded a standard rate constant of 1.3 s^{-1}. and reorganization energies of 1.0 eV and 1.4 eV for $\mathrm{TEMP\dot{O}}$ and $\mathrm{TEMPO^+}$ respectively. The drawback of the CV method of analysis used in the above study is that peak overpotentials cannot be easily corrected for iR drop. This method requires CV measurements at higher scan rates, at which iR drop becomes significantly high ($\sim$ 10 mV). Uncertainty in the peak positions contributes to errors in the kinetic parameter estimation. Therefore, the electron transfer kinetics of $\mathrm{TEMP\dot{O}}$ coupled electroactive SAM needs to be verified using an alternative electrochemical method. Also, at higher scan rates, the potential windows must be extended to very large overpotentials to find the peak positions. Large overpotentials adversely affect the chemical stability and molecular orientation of the redox-active SAM layers on the electrode surface.

This chapter reports cyclic voltammetric and chronocoulometric analysis of electroactive monolayers of $\mathrm{TEMP\dot{O}}$ tethered to alkylthiol SAMs of various chain length. Covalently attached electroactive species to the SAM terminals makes the system less sensitive to the pinholes and defects in the SAM. The surface activation process via EDC/NHS for amide coupling is employed to covalently bind the amino substituted $\mathrm{TEMP\dot{O}}$ to the –COOH functionalized alkyl thiol SAM on Au electrodes. The kinetic analysis of the C_n-$\mathrm{TEMP\dot{O}}$ system that follows is built on the same framework described in Chapter 2. Specifically, the $\mathrm{TEMP\dot{O}/TEMPO}$ $^+$ redox couple is assumed to follow Langmuir-type kinetics for the reaction

$$TEMPO^+_{(Ox)} + e^- \rightleftharpoons TEMPO_{(Red)} \tag{7.1}$$

so that,

$$\frac{d\theta}{dt} = k_f(1-\theta) + k_b(\theta) \tag{7.2}$$

where $\theta = \dfrac{\Gamma_{Red}}{\Gamma_{Ox} + \Gamma_{Red}}$ in which Γ_{Ox} and Γ_{Red} are the surface concentrations of the oxidized and reduced species and, k_f and k_b are the rate constants for the oxidation and reduction reactions, respectively. It is recommended that the reader revisits Section 4.1 to familiarize themselves in the terminologies and definitions.

---

[1] Laviron interaction model provides a simple way to estimate the interaction coefficients between redox centres and predict the randomness of the distribution of electroactive sites within the SAM layer. The absence of redox peak splitting in $\mathrm{TEMP\dot{O}}$ modified electrodes is attributed to molecular homogeneity of electroactive sites, more precisely, phase segregation of $\mathrm{TEMP\dot{O}}$ moieties. According to this model, strong attractive interactions between redox centres leads to sharp CV curves and weak repulsive interaction broadens the CV curves

7.2 Experimental details

All the chemicals including 4-amino-TEMPȮ, N-(3-Dimethylamino propyl)-N'-ethylcarbodiimide hydrochloride (EDC), N-Hydroxysuccinimide (NHS) and the various mercapto alkanoic acids (6-mercapto hexanoic acid (MHA) , 8-mercapto octanoic acid (MOA), 11-mercaptoundecanoic acid (MUA), 12-mercapto dodecanoic acid (MDA), and 16-mercaptohexadecanoic acid (MHDA)) were purchased from Sigma Aldrich. The polycrystalline gold electrode was made by melting a 0.5 mm gold wire (99.99%) in a propane flame. The surface impurities from the Au bead were removed by immersing in aqua regia and repeated melting. The electrode was allowed to cool slowly in air after the final melt. Electrodes formed in this fashion were cleaned with freshly prepared piranha solution (3:1 H_2SO_4 and 30% H_2O_2) and gently flame annealed prior to every experiment. The Au electrode surface was modified with acid-terminated SAMs by immersing the cleaned gold bead electrodes in 5 mM solutions (solvent was 95% ethanol) of the alkanoic acid thiols for four hours. Then, the electrodes were rinsed thoroughly with 95% ethanol and deionized water. The SAM layers were treated overnight ($\sim$ 12 hr) with a reaction mixture containing 1 mM aqueous solutions of 4-amino-TEMPȮ and equimolar concentration (5 mM) of EDC and NHS. After the reaction, electrodes were rinsed and stored in deionized water prior to electrochemical analysis. Electrochemical measurement were done with a computer-controlled system, consisting of a HEKA PG590 potentiostat and custom software written in the LabVIEW environment. A home-made Ag/AgCl in saturated KCl was used as the reference electrode and a flame-annealed, coiled gold wire served as the counter electrode. The electrolyte was 0.1 M $HClO_4$. Potentials are reported either with respect to the reference electrode, E, or as overpotentials, ($\eta = E_p - E^{0'}$), where $E^{0'}$ is the formal potential of the TEMPȮ redox couple.

7.3 Result and discussions

7.3.1 CV analysis of TEMPȮ coupled alkanethiol SAM

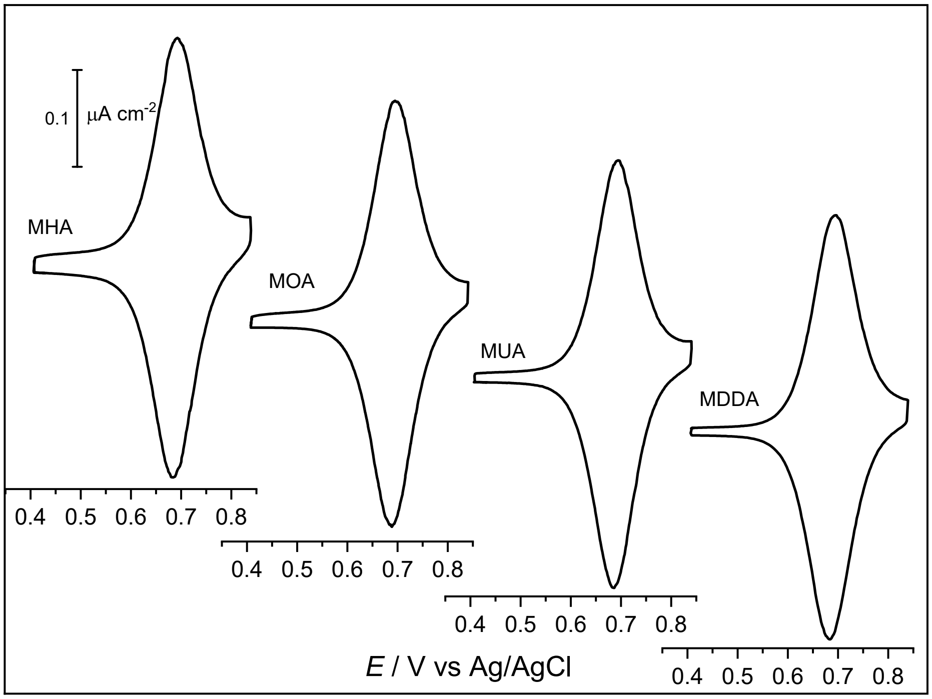

Figure 7.2: Cyclic voltammograms at 2 mV/s for C_n-TEMPȮ monolayers derived from a) mercaptohexanoic acid (C_6-TEMPȮ, MHA), b) mercapotoctanoic acid (C_8-TEMPȮ, MOA), c) mercaptoundecanoic acid (C_{11}-TEMPȮ, MUA) and d) mercaptododecanoic acid (C_{12}-TEMPȮ, MDDA)

The CVs of TEMPȮ molecules covalently attached to various alkyl length (C= 6 to 12)thiol SAM modified Au electrodes are given in Figure 7.2. Irrespective of the alkyl chain length, all CVs shows symmetric curve shapes, indicating the reversible character of the redox systems. The absence of any shoulders in the voltammogram of TEMPȮ/TEMPO$^+$ redox couples indicates homogeneity and the absence of intermolecular interactions between adjacent TEMPȮ moieties. The anodic sweep from the open circuit potential oxidizes the neutral radical TEMPȮ to form the nitrosonium cation. TEMPȮ in the neutral radical form can also undergo a proton coupled reduction to generate hydroxylamine species at negative enough potentials. However, this second charge transfer process cannot be observed here due to the poor stability of thiol SAM at the negative potentials, below -400mV vs Ag/AgCl. This observation correlates with previous reports of slow kinetics for the reduction of TEMPȮ.(138; 139) Detailed analysis of all the CV plots in Figure 7.2 are summarized in Table 7.1.

SAM (CH$_2$ units)	**Anodic (cathodic) peak potential / V**	$\mathbf{i}_{p,a}$ **/** $\mathbf{i}_{p,c}$	**Anodic (cathodic) peak FWHM / mV**	$E^{0/}$ **/ V**	**TEMPȮ coverage (x 10^{-10} moles cm^{-2})**
MHA (5)	0.692 (0.684)	0.93	92 (95)	0.688	1.52
MOA (7)	0.691 (0.685)	0.93	92 (94)	0.692	1.44
MUA (10)	0.693 (0.687)	0.93	91 (92)	0.690	0.68
MDDA (11)	0.695 (0.685)	0.94	94 (95)	0.690	1.43
MHDA (15)	0.751 (0.648)	0.91	178 (178)	0.699	0.30

Table 7.1: Data summary of TEMPȮ SAM cyclic voltammograms measured at 2 mV/s

The double-layer capacitance is significantly different for the reduced and oxidized forms of the TEMPȮ derivatives. Larger capacitance at the oxidative end of the cyclic voltammetry is due to the adsorption of electrolyte species (ClO_4^-) to the TEMPO$^+$ (nitrosonium cations). Long-chain alkanethiols form highly ordered and stable SAM layers compared to shorter-chain counterparts, since attractive van der Waal interaction enhances with the increasing number of alkyl units.(140) Highly ordered SAMs result in lower double-layer capacitance, as shown in the case of TEMPȮ tethered to MDDA and MUA compared to MDA and MHA layers. Full-width half maxima (FWHM) values were obtained after correcting an estimate of the double-layer charging current. The short-chain systems ($n \leq 12$) show FWHM values very close to the theoretical values for ideal, non-interacting redox monolayers (90.6 mV).(27) A significant increase in the FWHM for C$_{16}$-TEMPȮ indicates very sluggish ET kinetics for that particular system.

The surface coverage of TEMPȮ on each alkyl system was estimated by integrating the baseline corrected oxidative peak of respective CVs. The trend showing lower TEMPȮ coverage for longer carbon chain length is due to the effect of increasing crystallinity in C$_{16}$ SAM. As discussed in Chapter 3, long-chain alkyl SAM ($\geq$ C$_{16}$) shows crystalline character, whereas shorter-chain alkyl thiol SAM is more liquid-like (least organized). Hence, the terminal functionality in the latter group is easily accessible for surface activation. Schönherr et al.(141) reported NHS esters at the termini of C$_{11}$ SAM hydrolyzed more rapidly than those of C$_{16}$ SAM.

The results indicate that the terminal functional groups of highly ordered interfacial structures show poor reactivity due to conformational and steric effects. The calculated values are about five-fold smaller than the theoretical maximum surface coverage of TEMPȮ SAM ($4.8 \pm 0.2 \times 10^{-10}$ moles cm^{-2}) which is in the agreeable range with previously reported values.(142) The low surface density of TEMPȮ promotes ideal ET homogeneity since it mitigates intermolecular interactions.(143) Electron transfer theories such as Butler-Volmer and Marcus-Hush-Chidsey assume all the redox centres occupy an identical environment. Densely packed TEMPȮ monolayers can result in clustering and phase separation, and consequently an inhomogeneous distribution of redox centres,(144; 145) which leads to kinetic heterogeneity and the observation of multiple ET rate constants at a given overpotential.(75).

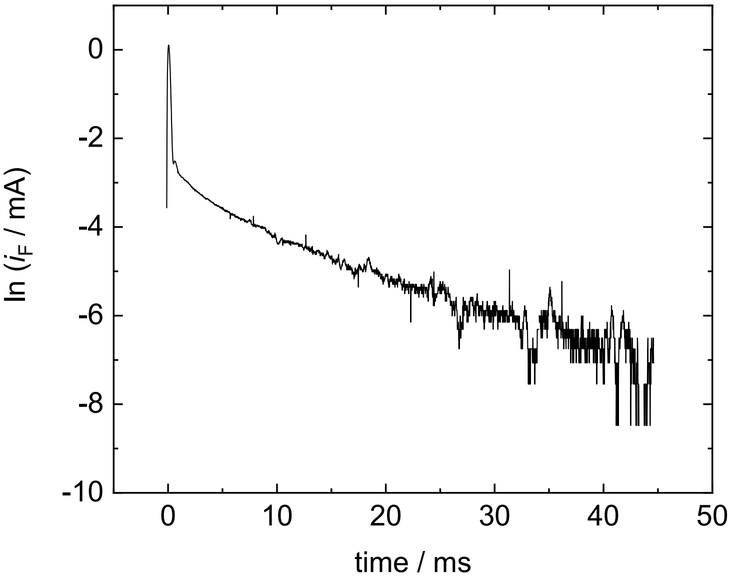

Figure 7.3: The current transient of C$_8$-TEMPȮ SAM on a gold bead electrode

The level of heterogeneity in TEMPȮ SAM systems prepared for kinetic analysis are discussed as follows. Equation 7.3 shows the linear relation between the faradaic current (i_F) in logarithmic scale with time, in which a single apparent rate constant ($k_{app} = k_f + k_b$) describes the overall electron transfer to all the redox centres upon a potential step.

$$i_F = k_b q_{F,max} \exp(-k_{app} t) \tag{7.3}$$

In equation 7.3, $q_{F,max}$ is the Faradaic charge associated with the conversion of all the redox centres in the monolayers. The chronoamperogram of MOA-TEMPȮ SAM system, collected for a potential step from base potential(0.40 V) to the formal potential ($\eta = 0.190$ V), is shown in Figure 7.3. The linear nature of the plot after the initial current spike (which corresponds to double-layer charging) confirms the kinetic homogeneity of ET at the TEMPȮ/TEMPO$^+$ redox centres coupled to the alkane chain terminals.

7.3.2 Laviron analysis of TEMPȮ coupled alkanethiol SAM

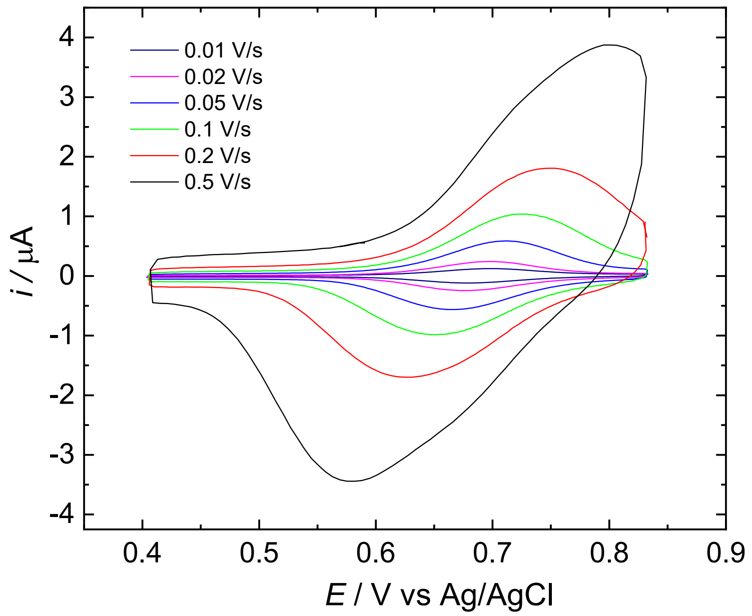

Figure 7.4: Cyclic voltammetry of C_{12}-TEMPȮ SAM on Au electrode at various scan rate

Kinetic parameters related to ET processes can be extracted by analyzing the CVs collected at different scan rates. Laviron established a mathematical formulation that relates the peak potentials with the potential sweep rates for electrochemical systems where diffusion control is absent, redox species are strongly adsorbed and the Langmuir isotherm is obeyed.(106) From this mathematical approach (which is discussed in detail below), kinetic parameters such as the transfer coefficient and the rate constant of the electrochemical reaction can be deduced. The C_{12}-TEMPȮ system shows symmetrical redox peaks, without any peak separation at slower sweep rates ($\upsilon \leq 0.1V/s$) which indicates its reversible nature. However, at fast enough sweep rates, the electron transfer during the redox process becomes irreversible and separation between the oxidation peak potential ($E_{p,Ox}$) and the reduction peak potential ($E_{p,Red}$) increases as a function of scan rate (Figure 7.4). The specific expression that relates the applied potential with the sweep rate (υ) at irreversible conditions is:

$$E_{p,Ox} = E^{0'} + \frac{RT}{(1-\alpha)nF} \ln\left[\frac{(1-\alpha)nF\upsilon}{RTk_0}\right] \tag{7.4}$$

$$E_{p,Red} = E^{0'} - \frac{RT}{\alpha nF} \ln\left[\frac{\alpha nF\upsilon}{RTk_0}\right] \tag{7.5}$$

where α is the transfer coefficient and k_0 is the standard heterogeneous ET rate constant and n is the number of electrons transferred during the redox reaction. Equations 7.4 and 7.5 show the linear relation between overpotential ($\eta = E_{p,Red/Ox} - E^{0'}$) and the logarithm of the scan rate. The value of α can be obtained by plotting η vs $\ln \upsilon$ and equating the slope to ($\frac{RT}{(1-\alpha)nF}$).

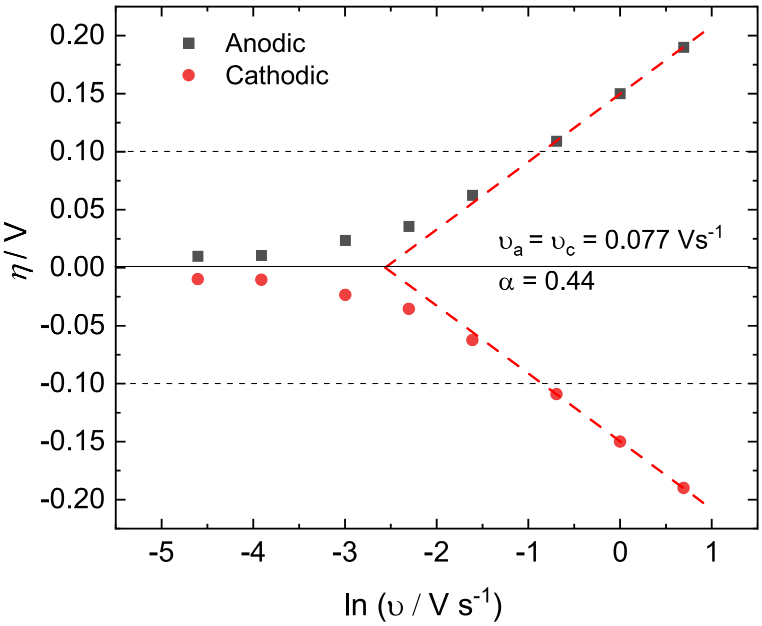

Figure 7.5: The plot showing Laviron analysis of C_{12}-TEMPȮ SAM on Au bead.

Experimentally, as shown in the Figure 7.5, the redox systems show a linear relation between η and $\ln \upsilon$ when the potential peak separation is greater than 200mV$/n$. The x-intercept obtained by extrapolating the slope of the linear region provides the value of critical sweep rates (υ_a and υ_c) for the anodic and cathodic branches, from which k_0 can be obtained as shown below:

$$k_0 = \frac{\alpha n F}{RT}\upsilon_c = \frac{(1-\alpha)nF}{RT}\upsilon_a \tag{7.6}$$

The value of k_{app} obtained from this analysis for the C_{12}-TEMPȮ SAM system is 1.3 s^{-1} and the transfer coefficient α is 0.44. The value of α is indicative of the symmetry of the redox reaction energy barrier and is expected to be 0.5 for a completely reversible system.(27) Laviron analysis is built on the Butler-Volmer formulation, which predicts a linear plot for $\ln k_f(E)$ versus E with a slope $-\alpha F/RT$. However, a significant deviation from linearity has been reported for surface-bound electroactive species like TEMPȮ tethered alkyl thiol SAMs which indicates a dependency of α on electrode potential. The slope $-\alpha F/RT$ will be linear when ET rate constants for TEMPȮ/TEMPO$^+$ systems are measured at relatively larger overpotentials using fast scan rates. Adversely, interference of iR drop on current measurement gets to worse at larger overpotentials. In addition, faster scan rates widen the redox peak separation and the potential extreme must be extended further from the formal potential of the TEMPȮ/TEMPO$^+$ redox couple. Since the formal potential of TEMPȮ/TEMPO$^+$ redox couple (c.a 0.70 V) is very close to the anodic potential stability limit of alkanethiol SAM, exceedingly larger overpotentials at the anodic limit oxidatively desorb the SAM layers.

7.3.3 Chronocoulometric analysis of TEMPȮ coupled alkanethiol SAM

According to Equation 7.3, the heterogeneous rate constant of a redox process at a given overpotential can be obtained by analyzing the chronoamperogram collected at that potential. Both, the chronoamperometric and chronocoulometric methods are developed on the same formalism that relates the faradaic current to electron transfer rate constants, however the later method offers some experimental advantages. The instrument settings such as bandwidth and the potentiostat rise time distort the shape of a chronoamperogram. The chronocoulomteric analysis described below is independent of such artifacts, since the method relies on the total charge obtained by integrating the current transients. In addition, numeric integration mitigates noise associated with small current transients.

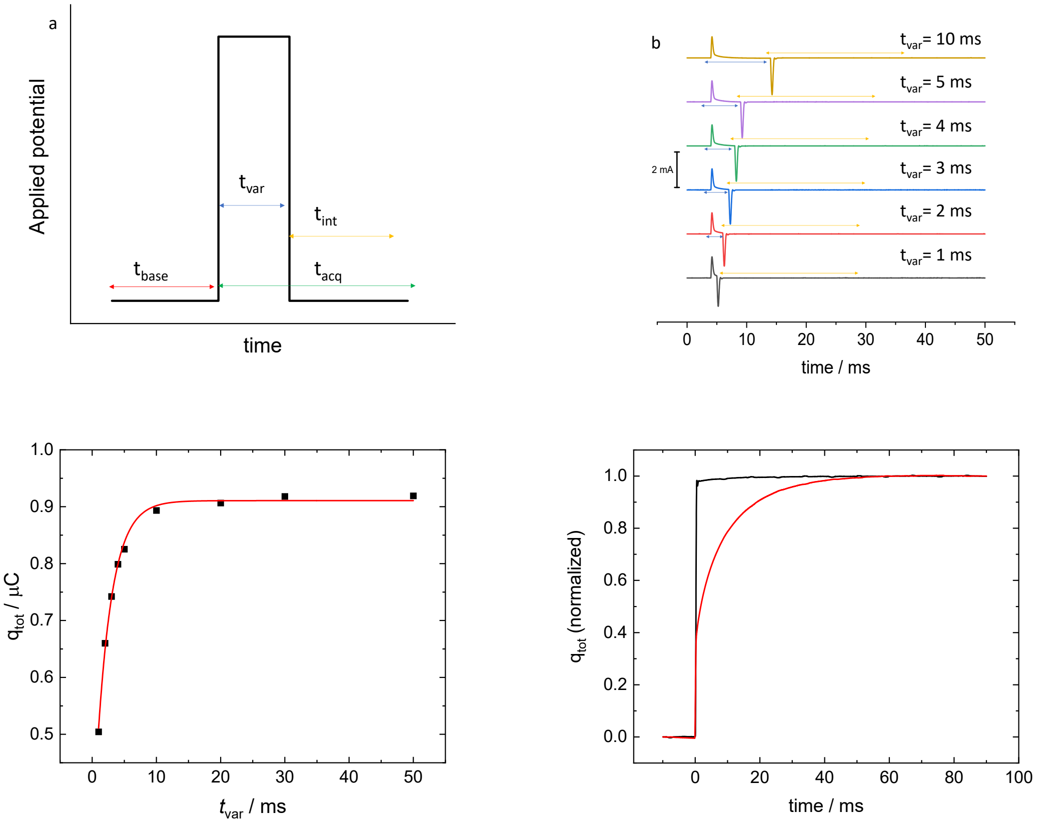

Figure 7.6: (a) Potential step sequence used in chronocoulometry experiments (b) Current transients collected at each potential steps (c) Plot of total measured charge obtained from integrating the current transients as a function of t_{var} (d) integrated and normalized charge transients for the same potential step for the C_8 TEMPȮ monolayer (red line) and MOA SAM (black line).

Double-step chronocoulometry An overview of chronocoulometric analysis to study electrochemical kinetics is discussed in Chapter 2. This section describes chronocoulometry analysis of TEMP$\dot{\text{O}}$-SAM redox system based on previous work from the Burgess group (146) which is a subset of the multistep method and the analytical solutions reported by Gonzlez et al.(147) Figure 7.6(a)-(d) depicts the multistep chronocoulometry method described in this section to extract the ET kinetic parameters. $\Gamma_{Red}, \Gamma_{Ox}$ and θ are the surface concentrations of TEMP$\dot{\text{O}}$, TEMPO$^+$ and the fractional coverage of the oxidized species, respectively. During the measurements, the initial potential applied to the working electrode is set to E_{base} at which the fractional coverage of the oxidized species, $\theta \rightarrow 0$ and subsequently stepped to a variable overpotential, E_{var} for a variable amount of time t_{var}. Then the electrode potential is stepped back to E_{base}. The current transients are collected during the potential steps, but it is the transient back to E$_{base}$ that is analysed. The integral of the second transient provides q_{tot} where q_{tot} is the total change consisting of the double layer charging and the charge required to re-reduce the TEMP$\dot{\text{O}}$ species oxidized at E_{var}. As the electrode stays at E_{var} for longer t_{var}, a dynamic equilibrium is established for the redox process and q_{tot} reaches saturation (Figure 7.6(c)).

In the case of surface-bound redox species as represented in Equation 7.1, the forward and backward reactions have characteristic first-order rate constants k_f and k_b, respectively. The total coverage of the redox-active species is the sum of the surface concentrations of oxidized and reduced moieties, i.e. $\Gamma_{Ox} + \Gamma_{Red} = \Gamma_{tot}$. The time-dependent change in the fractional coverage of the oxidized species ($\theta = \Gamma_{Ox}/\Gamma_{tot}$), due to a potential step is

$$\theta(t) = \frac{k_b}{k_{app}} \left[1 - \exp(-k_{app} t)\right] \tag{7.7}$$

where $k_{app} = k_f + k_b$. The derivative of Equation 7.7 gives the Fardaic current during the potential step, which is represented by Equation 7.3.

The Faradaic charge, $q_F = nF\Gamma_{Ox}$ (Faraday's law), likewise, the total charge associated with the reduction/oxidation of all the redox species is $q_{F,max} = nF\Gamma_{tot}$. Hence, Equation 7.7 can be written as

$$q_F(t) = \frac{k_b}{k_{app}} q_{F,max} \left[1 - \exp(-k_{app} t)\right] \tag{7.8}$$

The double layer charge, q_{DL} must also be added to Equation 7.8.

$$q_{tot} = \frac{k_b}{k_{app}} q_{F,max} \left[1 - \exp(-k_{app} t)\right] + q_{DL} \tag{7.9}$$

Experimental charge data fits to Equation 7.9 for total charge, as shown in Figure 7.6(c). Since q_{DL} holds no kinetic information about the ET process. It needs to be removed from total charge measured ($q_{tot} = q_F + q_{DL}$) during the potential step. It is evident from Figure 7.6(d) that the double layer charging occurs faster compared to the electron transfer process. The transient of MOA SAM, in the absence of redox centres, reaches maximum charge within 400 μs. Therefore, the value of q_{DL} can be determined from the fitting exponential function (Figure 7.6(d)) at t= 0.

The time, t_{var}, required for the faradaic charging to reach equilibrium depends on the reaction rate constant at E_{var}. However, at equilibrium, $q_{F,eq} = \frac{k_b}{k_{app}} q_{F,max}$, and as the $t \to \infty$, equation 7.9 becomes

$$q_{tot,t\to\infty} = \frac{k_b}{k_{app}} q_{F,max} + q_{tot,t=0} \tag{7.10}$$

The values of $q_{tot,t\to\infty}$ and $q_{tot,t=0}$ in the above equation can be obtained by fitting the experimental data to equation 7.9. However, isolation of k_f and k_b (i.e. the backward and forward rate constants) requires the charge associated with the reduction/oxidation of all the redox species, $q_{F,max}$. By definition, at the formal potential, $E^{0'}$ of a redox reaction, $k_f = k_b = k_0$ (heterogeneous rate constant) and equation 7.7 leads to a linear relationship between $ln(1-2\theta)$ and t_{var} with a slope of $-2k_0$.

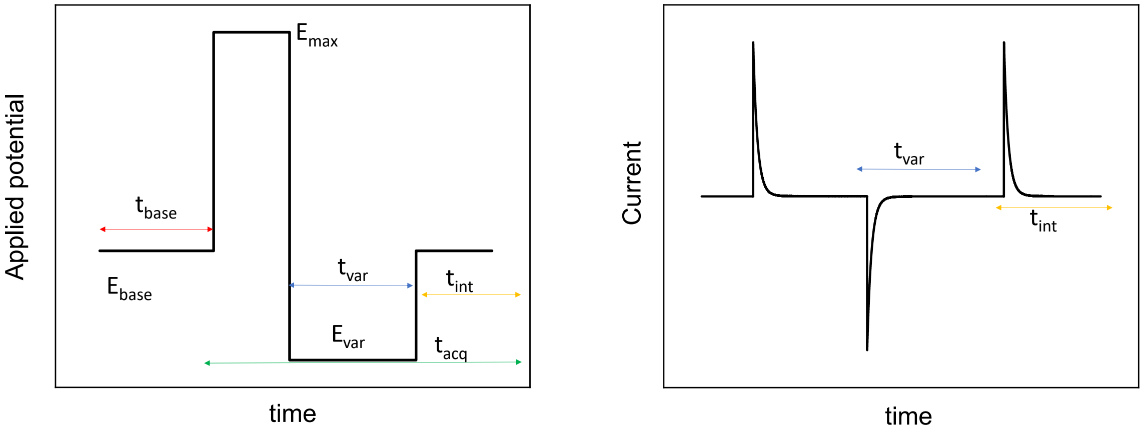

Figure 7.7: (a) Potential steps modified with intermediate step applied with variable time (b) Current transients collected at modified potential steps

Modified double-step chronocoulometry The double-step chronocoulometry method described above works well for the potential steps were $E_{var} > E^{0'} - 50mV$. The potential steps with higher overpotentials, η, result in the current transients with faradaic contributions that are separable from double layer charging. Conversely, for smaller current transients recorded at potential steps with $\eta < -50mV$, reliable measurement with required bandwidth settings of the potentiostat is not possible. In this case, a modified chronocoulometry procedure is required. This is achieved by introducing an intermediate potential step $E_{max}(\eta = +150mV)$ prior to the step to, E_{var} as shown in Figure 7.7(a). The electrode potential is maintained at E_{max} for a duration sufficient to complete the conversion of TEMPȮ to TEMPO$^+$. Subsequently, the potential is stepped to $E_{var}(\eta < -50mV)$ for a variable amount of time before stepping to E_{base} (Figure 7.7(b)). The kinetic information at $\eta < -50mV$ is obtained by analyzing the transients recorded between the potential step E_{var} to E_{base}. A similar mathematical treatment discussed above applies to the modified double chronocoulometry experiment. The modified integrated equation describing the time-dependent change in θ is

$$\theta(t) = \frac{k_b}{k_{app}} + C\exp(-k_{app}t) \tag{7.11}$$

where C is an integration constant. In this scenario, unlike the double-step method where $\theta_{t=0} = 0$, the initial condition here is $\theta_{t=0} = 1$. Therefore, the modified form of Equation 7.7 becomes,

$$\theta(t) = \frac{k_b}{k_{app}} + \left[1 - \frac{k_b}{k_{app}}\right]\exp(-k_{app}t) \tag{7.12}$$

When a dynamic equilibrium condition is established (i.e $t \to \infty$), the above equation becomes,

$$\theta_{t\to\infty} = \frac{k_b}{k_{app}} \tag{7.13}$$

Expressing Equation 7.12 in terms of charges gives

$$q_F(t) = q_{F,max}\left\{\frac{k_b}{k_{app}} + \left[1 - \frac{k_b}{k_{app}}\right]\exp(-k_{app}t)\right\} \tag{7.14}$$

As described before, the experimentally obtained charge, q_{tot} is the sum of faradaic charge associated with the reduction of oxidized species and the double layer charging associated with potential step, therefore

$$q_{tot}(t) = q_F + q_{DL} = q_{F,max}\left\{\frac{k_b}{k_{app}} + \left[1 - \frac{k_b}{k_{app}}\right]\exp(-k_{app}t)\right\} + q_{DL} \tag{7.15}$$

Once again, the various kinetic parameters of interest k_f, k_b and q_{DL} are extracted by fitting the experimental data to equation 7.15 and solving the following equations,

$$k_{app} = k_f + k_b \tag{7.16}$$

$$q_{tot,t\to\infty} = \left[\frac{k_b}{k_{app}} - 1\right]q_{F,max} + q_{tot,t=0} \tag{7.17}$$

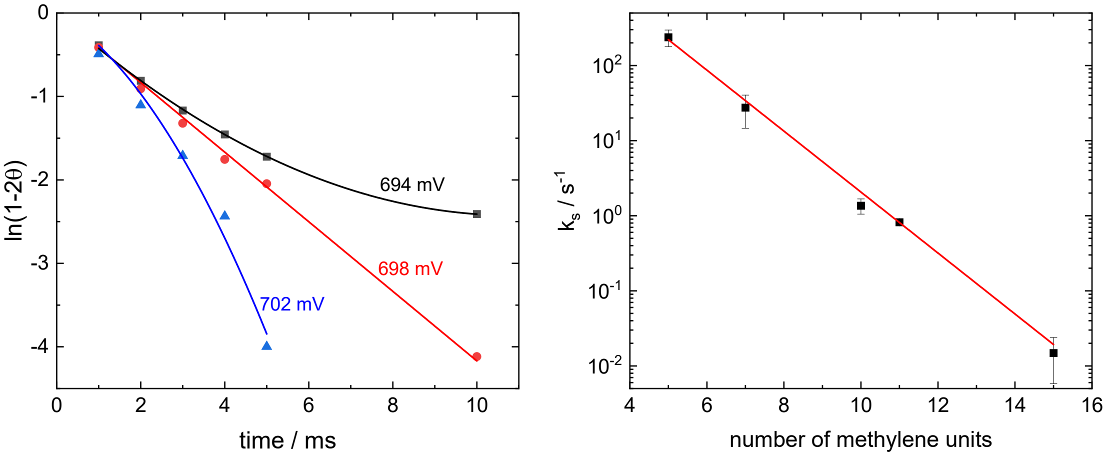

Figure 7.8: (a) Plots of the natural logarithm of the fraction of TEMPO$^+$ remaining on a C_{11}-TEMPȮ modified gold bead electrode as a function of t_{var} for different step potentials near the formal potential (b) influence of the SAM chain length on the standard rate constant. Each point is the average of a minimum of four measurements on unique SAMs.

Accurate elucidation of kinetic parameters using the above mathematical treatment requires determination of the exact values of $E^{0'}$ for each TEMPȮ SAM system. Approximate values of $E^{0'}$ for the TEMPȮ/TEMPO$^+$ redox system are obtained from cyclic voltammetry. The double-step chronocoulometry is quite effective in determining the true formal potential. Potential step E_{var} is set at various potentials close to the expected $E^{0'}$ of TEMPȮ SAM systems. Figure7.8(a) shows the sensitivity of plots constructed from charge measurements at three potentials close to the formal potential for the C_{11}-TEMPȮ SAM system. The slope of $ln(1-2\theta)$ verses t_{var} in Figure7.8(a) shows linearity only at the true formal potential, and a clear deviation from linearity is evident for all other potentials (even at 4 mV difference from $E^{0'}$). The standard rate constants are determined from the slope and measurements are repeated for various chain length, C_6 to C_{16} of TEMPȮ SAMs (Figure 7.8(b)).

The electron tunnelling decay constant, β, along the molecular chain can be obtained from the logarithmic plot (Figure 7.8(b)) since $k_0 \propto \exp\left[-\beta x\right]$, where x is the number of methylene units. The calculated value of β is 0.96 ± 0.04 per methylene units or 0.74 ± 0.03 per $\mathring{A}$, which is in agreement with the reported tunnelling decay constants for pendant ruthenium redox centres and about $10 - 15\%$ smaller than the values reported for ferrocene terminated SAMs.(43; 86) Detailed inspection of Figure 7.8(b) indicates that the one TEMPȮ SAM system with an even number of methylene units (MUA) has a k_0 value below the best fit line within the error bars. This observation indicates the possibility of the well established odd-even (parity) effect in TEMPȮ SAM systems, which arises from differences in the plane of electron transfer caused by configurational differences in SAMs with odd and even number of methylene units. According to Amara et al.(148), odd-even effects also influence the dielectric permittivity of SAM termini, which would change the electronic coupling and the outer-electronic reorganization energy. However, the data here is not sufficient to provide conclusive evidence about the existence of an odd-even effect in TEMPȮ SAM.

7.3.4 Tafel analysis and reorganization energy of TEMPȮ coupled alkanethiol SAM

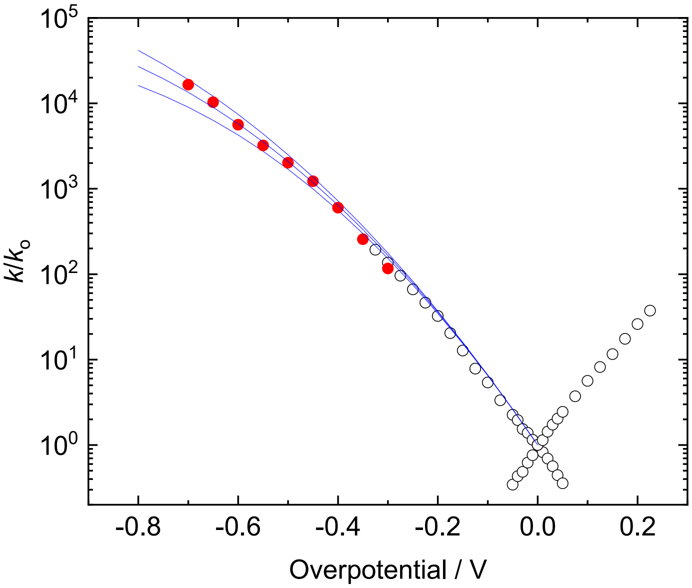

Figure 7.9: Tafel plots for C_{12}-TEMPȮ (open black circles) and C_{16}-TEMPȮ (solid red circles) on a gold bead electrode. Blue lines are calculated Tafel plots assuming a reorganization energy (from bottom to top) of 0.9 eV, 1.0 eV and 1.1 eV

Electron transfer kinetics gets faster with increasing overpotentials (except for the inverted region, refer to Section 2.2 for details). In the case of short chain TEMPȮ SAM systems C_6 to C_{11}, the kinetic separation between double layer charging and fardaic processes becomes indistinguishable even at smaller overpotentials. However, for the long chain systems like C_{12} TEMPȮ SAM, the potential step method described above could be employed for $|\eta| <\sim 0.3V$ (with the potential risk of oxidative desorption of thiol SAM above +0.225 V). The k_f and k_b of the C_{12}-TEMPȮ system, elucidated at different overpotentials are normalized with the standard rate constant $(0.9 \pm 0.2s^{-1})$ and shown in the Tafel plot (open black circles in Figure 7.9). Tafel analysis is a useful method for evaluating kinetic parameters. Based on the Butler-Volmer formalism, the rate constant values are linearly related to η in a narrow potential range near $E^{0/}$. The slope of the anodic branch between $-0.05V \leq \eta \leq 0.10V$ and cathodic branch between $-0.10V \leq \eta \leq 0.05V$ gives the transfer coefficient (α) of 0.531± 0.01 and 0.45 ± 0.01, respectively. The value of α at zero overpotential is 0.49±0.01 V which underlines the Nernstian behaviour of TEMPȮ SAM system.

Closer inspection of Figure 7.9 reveals that the anodic rate constant values are consistently lower than the cathodic values at equivalent overpotentials. According to Finklea and Madhiri (83), this trend is due to the smaller reorganizational energy of oxidized moieties compared to that of reduced moieties. The above authors assessed transfer coefficients at relatively larger overpotentials, using cyclic voltammetry. The $\alpha_{\eta=0}$ (reported as greater than 0.5) is obtained by data extrapolation along larger overpotentials, hence the method is less accurate. Meanwhile, the kinetic data in the present study measures rate constants closer to the formal potentials and calculates $\alpha_{\eta=0}$ from the average Tafel slope as $\eta \to 0$.

The ET rate constant values at larger range of overpotentials are required to obtain reorganizational energy of the redox termini. As mentioned before, inherently faster (shorter alkyl chain) TEMPȮ SAM systems shows experimental limitations for measurements at larger overpotentials. Therefore, a Tafel plot over a wide range of overpotential is created by combining the rate constants of C_{16}-TEMPȮ and C_{12}-TEMPȮ SAMs, normalized with their respective standard rate constants. Figure 7.9 shows a good overlap of C_{16}-TEMPȮ (solid red circles) and C_{12}-TEMPȮ datasets and three simulated Tafel slopes (blue solid lines) using the Marcus-Hush-Chidsey equation (given in Appendix A) using reorganizational energies, λ, of 0.9, 1.0 and 1.1 eV. Based on this evaluation, the λ for C_{16}-TEMPȮ is between 0.9 and 1.1 eV. Previously reported λ for free radial and nitrosonium form in C_{11}-TEMPȮ SAM system is 1.45 ± 0.15 eV and 1.30 ± 0.15 eV, respectively. The observation of smaller λ for C_{16}-TEMPȮ compared to C_{11}-TEMPȮ could be attributed to chain length dependencies as previously reported for both ruthenium pentaammine and ferrocene SAMs.

7.4 Conclusion

The ET kinetics of TEMPȮ coupled to various chain-length alkanoic acid SAMs grafted on polycrystalline Au surfaces were studied using cyclic voltammetry and chronocoulmetric techniques. Low-density TEMPȮ coverage exhibits very little kinetic heterogeneity. The standard ET rate constants follow the expected exponential dependence on the chain length of the SAM spacer layer. The forward and backward ET rate constants, obtained from the double-step chronocoulometric method, reveal asymmetry in the reversible free radical/nitrosonium redox couple. At low overpotentials, the Tafel plot has a smaller slope for the cathodic branch compared to the anodic branch, and the interpolation leads to a transfer coefficient at zero overpotential of 0.49 ± 0.01. At moderate overpotentials, the anodic rate constants are consistently lower than the equivalent overpotential on the cathodic branch. This indicates lower reorganization energy for the oxidation half-reaction compared to the reduction half-reaction. The reorganization energy of TEMPȮ is obtained from experimental data collected at large negative overpotentials and simulated Tafel plots from the MHC formalism. The estimated reorganization energy of $TEMPO^+$ attached to C_{16} SAM is 1.0 ± 0.1 eV.

Ghosh and Hammes-Schiffer reported a computational study for calculating the reorganization energy of redox-active SAM.(149) That study highlights a feature of $TEMPO^+$ exhibiting larger inner and solvent reorganization energy (0.50 and 0.93 eV respectively) compared to other redox molecules. Inner reorganization energy is attributed to the degree of structural changes the redox molecules undergoes upon reduction. Due to larger deviation in the calculated solvent reorganization energies compared to experimental values, the authors suspected that the anionic form of redox species may locate further from the SAM-solvent interface than cationic species of TEMP$\dot{\mathrm{O}}$. Structural information of electroactive SAM obtained from electrochemical measurements are limited, hence not enough experimental evidence are available. As described in Chapter 1, surface enhanced IR spectroelectrochemistry is capable of monitoring surface confined electroactive species *in-situ* conditions. Details about the ET kinetic parameters and the structural changes associated with the ET process in redox-active monolayers can be obtained from conventional electrochemical analysis and the surface enhanced IR spectroelectrochemistry, respectively. Complementary information can be put together to generate a bigger picture of the electron transfer processes occurring at the SAM-electrode interface.

8 IR spectroelectrochemical analysis of the TEMPȮ coupled alkanethiol monolayers

Contributions All the experiments and result analysis, discussed in this chapter are solely conducted by Bipinlal Unni, under the supervision of Dr. Ian Burgess. Some of the results discussed in this chapter are published in Electrochimica Acta 2021, 381, 138263. Methodologies used for the time-resolved spectroelectrochemical measurements are developed by Dr. Kaiyang Tu.

8.1 Introduction

Electrochemical surface enhanced infrared absorption spectroscopy (EC-SEIRAS) is a powerful tool to obtain structural information from the electrochemical interface, without interference from the electrolyte.(14) A comparison of spectral and electrochemical data is necessary for obtaining a deeper understanding of electrochemical processes. Performing time-resolved EC-SEIRAS studies in tandem with electrochemical measurements such as chronocoulometry can provide a wealth of information on electrode kinetics and associated structural reconfiguration. In the case of conventional electrochemical methods, interference from the double-layer charging complicates the study of electrode kinetics of fast reactions (with time constants equal to or smaller than that of double-layer charging). EC-SEIRAS has been successfully employed to study the adsorption/desorption of molecules at the electrode surface within the time domain of double-layer charging.(150) The high surface sensitivity of ATR-SEIRAS has been utilized to monitor various electrochemical features, including the double-layer structure, potential induced adsorption/desorption of molecules, characterization of self assembled monolayers (SAMs) and real-time monitoring of electrochemical surface reactions.(96; 151) Adsorption of water on the electrode is of special interest in electrochemical systems since it reflects the status of the molecular environment and the order of monolayers on a metal surface.

The redox moieties with IR active vibrational modes during the potential dependent structural changes are favoured for IR spectroelectrochemical analysis. TEMPȮ (2,2,6,6-tetramethylpiperidine-1-oxyl), a redox-active free radical, is expected to show IR absorption bands such as υ(N=O) that corresponds to its oxidation, in addition to other IR spectral features. Even though TEMPȮ-tethered SAM has been a subject to electrochemical analysis (83), time-resolved IR spectroelectrochemical analysis of TEMPȮ based redox system is first reported by Unni and Burgess (152) and part of the results (electrochemical kinetic analysis using cyclic voltammetry and chronocoulometry) are discussed in Chapter 7. Using EC-SEIRAS, a detailed structural study of the redox process of TEMPȮ molecules surface confined to a SAM-modified Au film is included in this chapter. A complementary analysis of EC-SEIRAS results with the chronocoulometric measurements of TEMPȮ provides comprehensive details of the redox behaviour of TEMPȮ coupled monolayers on Au. Time-resolved EC-SEIRA spectra are measured in rapid scan mode, to demonstrate an advanced method to study electrode dynamics. The kinetic results are combined and contrasted with electrochemical data.

8.2 Experimental details

The reagents 4-amino-TEMPȮ (free radical), N-(3-Dimethylaminopropyl)-N'-ethyl carbodiimide hydrochloride (EDC), N-Hydroxysuccinimide (NHS) and 12-mercapto dodecanoic acid (MDA) were purchased from Sigma Aldrich and used as received.

SEIRAS substrate preparation A 60° face-angled Si crystal (PIKE technologies) was used as the internal reflection element (IRE) for ATR-SEIRAS experiments. The principal reflecting plane of the IRE was polished with 3 microns and 0.5 microns diamond polishing solutions, rinsed with copious amount of deionized water and air dried. Approximately 20 nm thickness of indium tin oxide (ITO) was sputter coated on the IRE surface using a home-built RF magnetron sputtering unit using a power of 30 W and a base vacuum of 4×10^{-5} Torr. The ITO sputtered IRE was annealed under vacuum at 300 ^{o}C for an hour and was assembled in a Jackfish SEC J1 cell (Jackfish JEC). The ITO-coated Si IRE served as the working electrode for in situ spectroelectrochemical experiments. SEIRAS active gold layers on the ITO surfaces were prepared by electrodepositing gold islands from an electrolyte containing 0.25 mM $KAuCl_4$, 0.1 mM 4-methoxypyridine and 50 mM $KClO_4$. After the electrodeposition, the gold layer on ITO was rinsed thoroughly with deionized water, before TEMPȮ coupled SAMs were formed on the Au island film using the protocol described in the previous chapter.

FT-IR measurements IR measurements were performed using a Bruker Vertex 70 FT-IR spectrometer with a liquid nitrogen cooled, MCT detector. An in-house developed Labview program was used to control both the IR spectrometer and potentiostat. The IRE assembled Jackfish SEC cell was mounted on a VeeMax III optic box (PIKE technologies) and the angle of incidence was set to 60°. The IR spectra were collected between 800 and 4000 cm^{-1} at 8 cm^{-1} resolution and 2 mm aperture. The scanning velocity was 40 kHz for ATR-SEIRAS measurements and 160 kHz for the time-resolved ATR-SEIRAS measurements.

8.3 Result and Discussion

8.3.1 IR spectral peak analysis of TEMPȮ and TEMPO$^+$

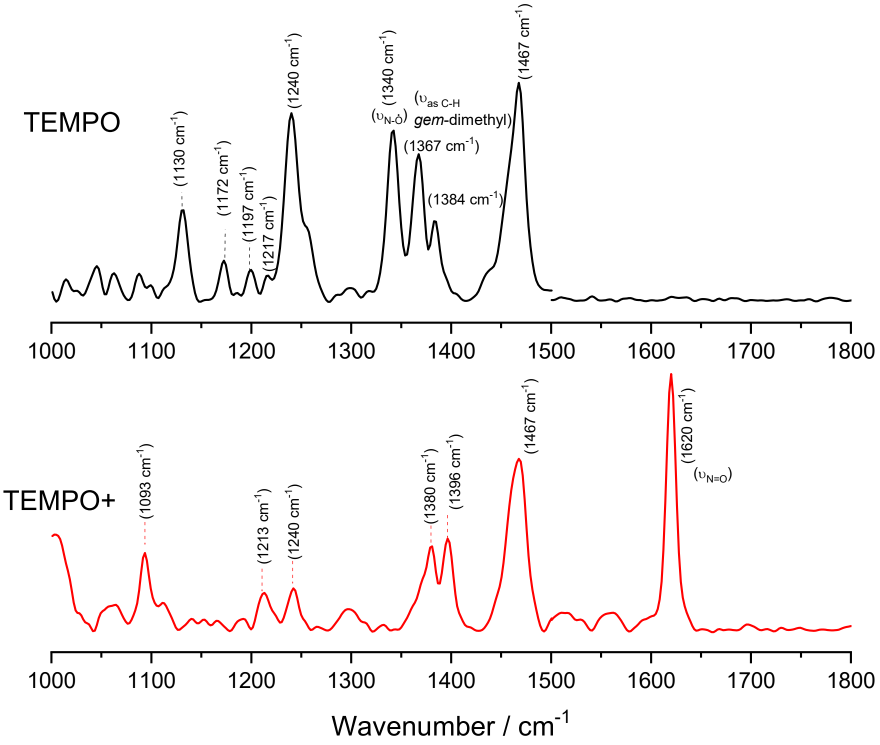

Figure 8.1: IR transmittance spectra of TEMP$\dot{\mathrm{O}}$ and TEMPO$^+$

Figure 8.1 shows the IR transmission spectra of TEMPȮ and TEMPO$^+$. The synthesis and characterization of the oxidized form of TEMPȮ are provided in Appendix B. Peak assignments are carried out based on the IR spectra of TEMPȮ reported by Kotorlenko et al.(153) Earlier literature shows ambiguity in assigning the IR peak for υ(N–O). Rintoul et al.(154) compared their DFT calculations for υ (N–O) of nitroxide stable free radicals to the experimentally determined υ(N–O) band positions. In the case of cyclic nitroxides, the frequency of υ(N–O) is influenced by the ring substituent functional groups. Experimentally determined position of υ(N–O) for 6-membered cyclic nitroxides are reported in the range of 1395-1339 cm^{-1}.(154) Isotopic substitution experiments show TEMPȮ, an unsubstituted cyclic nitroxide free radical has υ(N–O) peak at 1339 cm^{-1} whereas DFT calculations predict 1344 cm^{-1} (Reference (14) with in the Reference (154). The spectroscopic studies by Symons et al.(155) on the solvation of nitroxide radicals (R$_2$NȮ) reported υ(N–O) in water at 1337 cm^{-1}. Our transmission spectra of TEMPȮ shows υ(N–O) peak at 1340 cm^{-1} which disappears when TEMPȮ is oxidised to form N=O. Grampp et al.(137) reported υ(N=O) at 1596 cm^{-1} in the case of TEMPO$^+$ meanwhile a detailed investigation on TEMPȮ-SiCl$_3$ by Pietschnig et al.(156) reports υ(N=O) at 1614 cm^{-1}. A strong peak at 1620 cm^{-1} is observed in the transmission spectrum of TEMPO$^+$, and is assigned to υ(N=O). The peak at 1467 cm^{-1} is reported as υ(N–O) (but it could also due to (C–H) bending from methyl group). The fact that the peak at 1467 cm^{-1} is unchanged after oxidation implies it is the CH bend. The peaks at 1367 cm^{-1} and 1384 cm^{-1} are assigned to *gem*-dimethyl group at the 2, 5 position of piperidine ring in TEMPȮ. It is also reported that a strong coupling exists between nearby substituent moieties, such as the *gem*-dimethyl group and N–O. The shift in the IR band position of *gem*-dimethyl group to 1380 and 1396 cm^{-1} upon TEMPȮ oxidation supports the above observation.

8.3.2 ATR-SEIRAS of TEMPȮ coupled monolayer

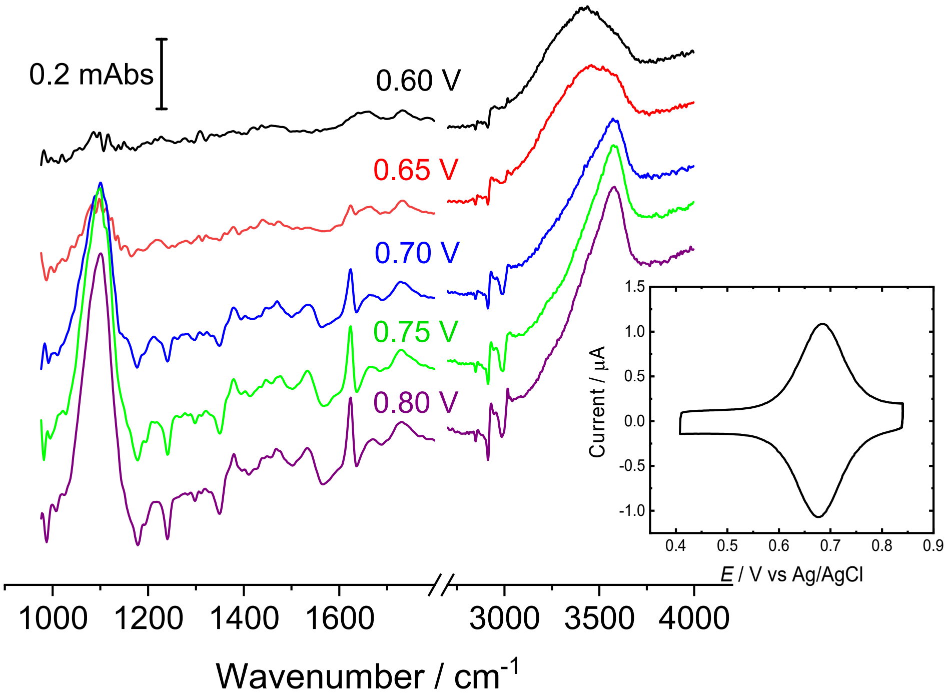

Figure 8.2: Potential dependant SEIRA spectra of TEMPȮ coupled C_{12}-SAM with respect to the reference spectra collected at $E = +0.4$ V; inset showing the cyclic voltammetry of TEMPȮ-C_{12}-SAM modified SEIRA film in the spectroelectrochemical cell.

Structural changes during the redox process of TEMPȮ coupled C_{11}-alkyl thiol SAM were measured using EC-SEIRAS (Figure 8.2). The SEIRAS experiments were conducted using electrochemically deposited Au on an ITO modified Si prism which serves as both the internal reflection element and the working electrode. The cyclic voltammetry (CV) in the inset of Figure 8.2 ensures the redox features of TEMPȮ-C_{12} alkyl thiol SAM on SEIRA layer is comparable to that of Au bead electrode used for electrochemical investigations reported in the previous chapter. The potential range for EC-SEIRAS measurements of TEMPȮ-C_{12} alkyl thiol SAM was chosen based on the CV. Higher capacitive currents for the SEIRA substrate, compared to Au bead electrode, arises from the bare ITO layer. Potential difference spectra shown in Figure 8.2 were obtained with respect to the single beam spectrum at $E = +0.4$ V (based on the CV features, all redox moieties are in a reduced form at +0.4 V). A potential dependent change in the reflectivity of the Au-ITO hybrid layer gives rise to the baseline tilt of the absorption spectra.

Major peaks emerge below 1800 cm^{-1} with increasing positive potential, including two upward absorbance features at 1100 and 1624 cm^{-1}, and three negative absorbance peaks at 1179, 1240 and 1349 cm^{-1}. Broad positive peaks at higher frequencies are seen between 3100 and 3700 cm^{-1}, and several upward and downward pointing features are identified between 2850 and 3000 cm^{-1}. Provided the coverage of TEMP$\dot{O}$ is about half the magnitude of the typical coverage of an alkyl thiol monolayer on Au, the overall quality of IR spectra is remarkable. The estimated coverage of TEMP$\dot{O}$ monolayers on Au bead was 0.68 × 10^{10} moles cm^{-2}. SEIRAS data is interpreted based on the vibrational peak assignment made on TEMP$\dot{O}$/TEMPO^{+} in the previous section. The peak at 1349 cm^{-1} is the N–O stretch of the nitroxyl radical,(154) which is also part of a complicated vibration involving a C–C stretch and a C–C–H bend that gives rise to the band at 1240 cm^{-1}. The upward band at 1624 cm^{-1} appearing at potentials positive of the onset of redox feature in the CV is assigned to the N–O stretch of the nitrosonium cation. Shift in the N–O stretch to the higher frequencies is consistent with an increased bond order from the N=O^{+} resonance contribution. The generation of the N=O^{+} cation also leads to the appearance of a strong upward band at 1100 cm^{-1} corresponding to the Cl–O stretching vibration of charge balancing perchlorate counterions.(157) Even though amide I and II vibrations are arguably present between 1800 and 1400 cm^{-1}, definitive assignments of these peaks are challenging due to the weak amplitudes and relatively larger widths of these minor peaks, coupled with the sloping baseline.

The C–H stretching bands in the high frequency region includes contributions from the methylene asymmetric and symmetric stretches of the spacer thiol and the methyl stretches of the TEMP$\dot{O}$ group. The weak band at 2848 cm^{-1} is likely to be the symmetric C–H stretch of the methylene units in the SAM. The decrease in absorbance of this peak indicates the tilting of the hydrocarbon backbone toward the surface normal.(158) As the molecules adopt an upright orientation, the transition dipole moment of the methylene stretching modes becomes parallel to the surface and gives less enhancement as per the SEIRAS surface selection rule.(14) This is similar to the IR studies of Fc-SH SAMs as discussed in Chapter 5. The two features at 2912 and 2928 cm^{-1} are attributed to a single bimodal feature arising from the methylene asymmetric stretching vibration, the position of which is known to depend on the organization of the hydrocarbon domain. The peak shift above 2918 cm^{-1} asserts a net increase in the disorder of the hydrocarbon chains.(159; 160). The downward peak at $\sim$ 2985 cm^{-1} in this region belongs to the C–H stretch of the methyl substituents on the piperidinyl ring. Computational studies on 4-methoxy TEMP$\dot{O}$ reported that the free radical and the nitrosonium cation differ in the lowest energy conformation of their piperidine ring.(161; 162) TEMP$\dot{O}$ exists in a chair conformation, with the substituent at the 4 position residing in an axial position for the preferred radical conformer and in an equatorial position in the preferred cation conformer.(163)

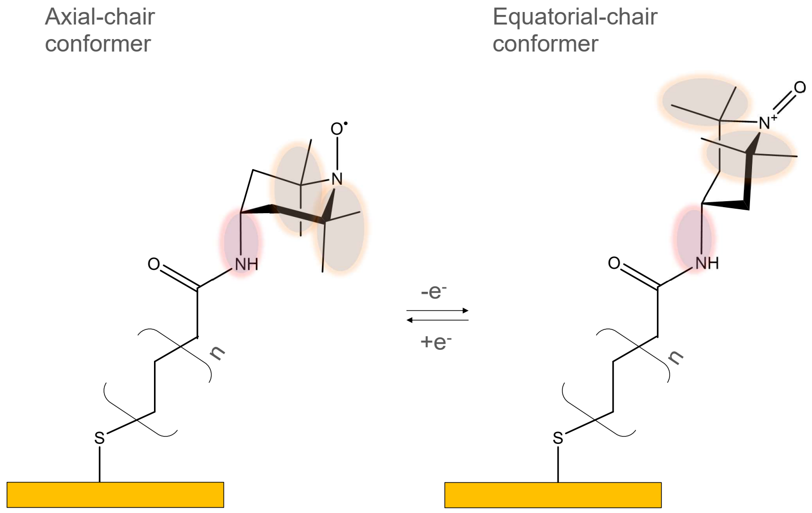
Axial-chair conformer
Equatorial-chair conformer
O•
N
NH
O
n
S
-e-
+e-
N+
O
NH
O
n
S

Figure 8.3: Proposed redox-induced conformational change in TEMPȮ SAMs

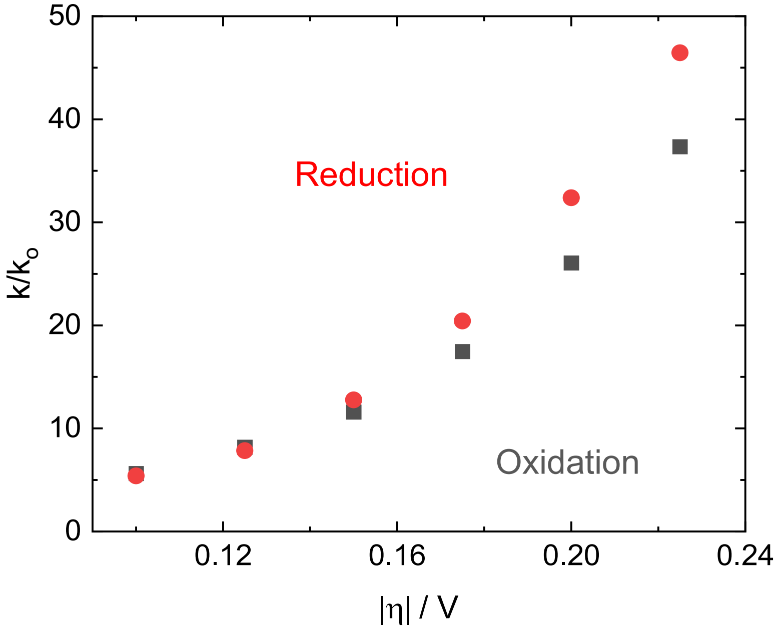

Figure 8.4: Tafel plot showing normalized rate constants of the anodic and cathodic branches of TEMPȮ-C_{12}-alkane thiol SAM redox system

Considering the SEIRAS band interpretation and previous computational studies, Figure 8.3 shows a proposed model depicting a redox induced conformational chair flip for a TEMPȮ-coupled SAM. The conformation changes associated with the chair flip pushes the N–O redox centre further away from the metal surface. This leads to a larger tunneling gap for electron transfer during the conversion of TEMPO^+ to the free radical. Finkela et al.(80) observed in one of their earlier studies on the effect of relative positions of the redox centres buried in different alkyl length diluent on ET kinetics, that the nature of the local environment around the redox centres influence the ET rates. The authors state that the apparent rate constant is partially dependent on the accessibility of the counterions to the redox centres. In the case of TEMPȮ/TEMPO^+ SAM system, the proposed conformational change deduced from SEIRAS study shows that the methyl substituents at the 2 and 5 positions on the piperdinyl ring are, on average, more parallel to the metal surface compared to the radical conformer. Hence, upon TEMPȮ oxidation, the conformational changes make the counterions less accessible to the N–O moieties of the redox centre. The result of the SEIRAS study prompted a re-evaluation of the rate constants obtained from the double-step chronocoulometric analysis. The lower rate constant values for the anodic branch compared to the cathodic branch shown in Figure 8.4 supports the above inference. The faster reduction rate also implies that the chair-chair conformational change occurs prior to the transfer of electrons to the TEMPȮ redox centres.

The positive absorbance feature at 3300 cm^{-1} corresponds to υ(O–H), is consistent with the ingress of water into the SAM layer during oxidation. The O–H stretch from water is broad and centred at ~3425 cm^{-1} below the formal potential, whereas the peak is narrower and shifted to higher frequency at more positive potentials. According to the ATR-SEIRAS studies on behaviour of water on bare and lipid modified metal surface, disruption of the hydrogen bonding network in water manifests as a higher frequency shift of υ(O–H).(164; 18; 165) The upward υ(O–H) band at relatively low frequencies prior to TEMPȮ oxidation is exemplified as water permeation through the defects in SAM as the Au surface becomes more hydrophillic upon accumulation of electronic charge. During the TEMPȮ oxidation, the water is dispersed into the SAM layer to associate with charge-balancing perchlorate anions. This observation is consistent with the report of Gautier et al.(166) on electrochemical quartz crystal microbalance studies of the oxidation of low-density TEMPȮ SAMs, where the mass change per electrical charge of the interface equated to the addition of one anion from the electrolyte per TEMPȮ molecule with sub stoichiometric amounts of accompanying solvent.

8.3.3 Time-resolved ATR-SEIRAS

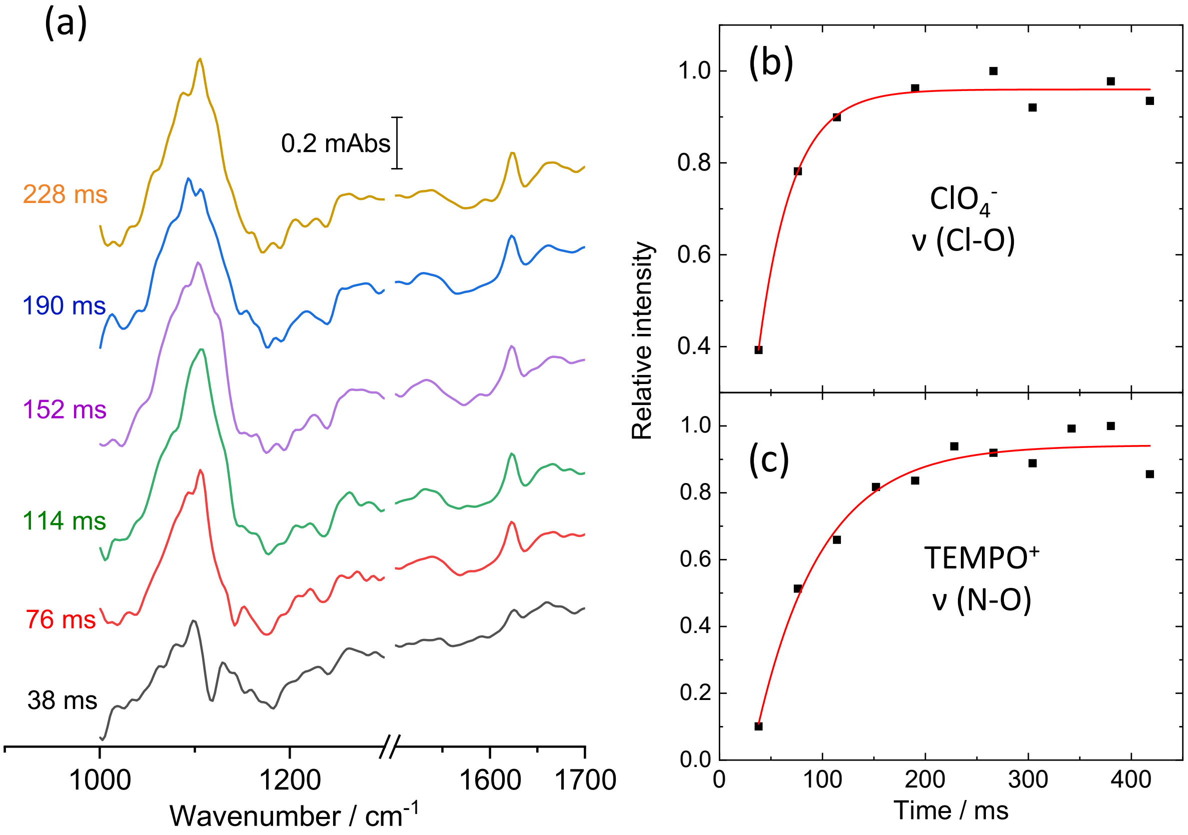

Figure 8.5: (a) Time-resolved ATR-SEIRAS spectra of TEMPȮ coupled to C_{12}-alkane thiol SAM on Au-ITO measured using rapid scan method, collected from +0.40 V (base potential) to 0.69 V vs Ag/AgCl (formal potential of TEMPȮ/TEMPO$^+$) (b) and (c) are the relative signal intensity plotted as a function of time at 1100 and 1624 cm^{-1}, respectively. The red trace shows the exponential fit to the data

Figure 8.5(a) shows the time-resolved SEIRA spectra from the rapid scan measurements collected during the oxidation of C_{12}-TEMPȮ SAM on Au-ITO. The rapid scan was performed upon the potential step from +0.40 V (base potential) to 0.69 V vs Ag/AgCl (formal potential of TEMPȮ/TEMPO$^+$). And the time-resolved spectra were created by co-adding 512 rapid scans. As discussed in the TEMPȮ/TEMPO$^+$ spectral analysis, the peaks at 1100 cm^{-1} is due to the υ(Cl–O) from the ClO_4^- counter-ions and the 1624 cm^{-1} belongs to the υ(N–O) of TEMPO$^+$. The plots shown in the Figure 8.5(b) and (c) are obtained from the relative signal intensities of peaks at 1100 cm^{-1} and 1624 cm^{-1} in the time-resolved TEMPȮ SAM spectra. The data were fit to a single exponential function, $Abs = A + exp(\frac{-t}{k})$ (the red traces in Figure 8.5 b and c). And the value of k is taken as the inverse of the measured rate constant. The apparent rate constant (equal to twice the standard rate constant, k_0) for the ingress of perchlorate into the redox monolayer is 30.3 ± 0.4 s^{-1} and the υ(N–O) is 15.8 ± 0.4 s^{-1}. In addition to the proposed model of conformational change in TEMPȮ-SAM, more details of the molecular events associated with ET of TEMPȮ SAM layer can be elucidated from the time-resolved SEIRAS and electrochemical evaluation. The k_0 for the TEMPȮ C_{12}-alkane thiol SAM on the same Au-ITO SEIRAS substrate, obtained from the double-step chronocoulometric analysis, was ~7 s^{-1}. The higher rate constant value for the perchlorate, compared to υ(N–O) and the electron transfer, implies that the ingress of counter-ions to the TEMPȮ redox centre occurs as the initial event of the ET process. Comparable values of the rate constant for the υ(N–O) peak and k_0 for the SEIRAS layer indicates conversion of N–Ȯ to N=O as the rate limiting step of the overall ET event.

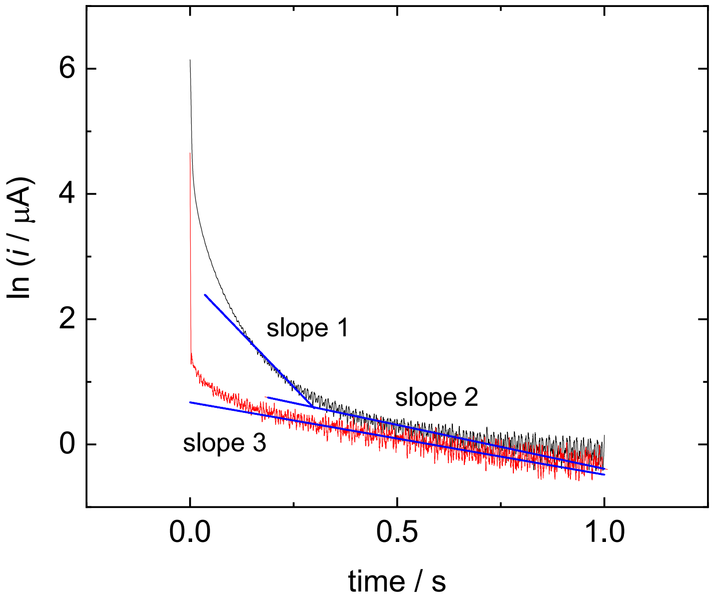

Figure 8.6: The current transients on semi-logarithmic scale, measured for TEMPȮ C_{12}-alkane thiol SAM on Au bead (red trace) and on Au islands electrodeposited on ITO as SEIRAS substrate (black trace)

A noticeable difference is found for the k_0 value of TEMPȮ SAM on SEIRAS layer (Au-ITO) and the Au bead. Therefore, further investigation are carried out to find the influence of substrate on the ET kinetics of the TEMPȮ/TEMPO$^+$ redox system. The SEC cell allows electrochemical as well as SEIRAS data to be collected. Figure 8.6 shows a comparison of the current transient for the potential step from the base potential (at which all the TEMPȮ species are in free radical form) to the formal potential of the TEMPȮ/TEMPO$^+$ redox couple. The same experiment was performed for a Au bead (red trace) and the Au-ITO SEIRAS substrate (black trace of Figure 8.6). It is notable that whereas the red trace reached a constant slope in the semi-logarithmic plot within ∼100 ms, the first ∼500 ms of the trace for Au-ITO is non-linear. The slower decay for Au-ITO is not entirely caused by RC charging. The RC time constant for the Au-ITO electrode in the spectroelectrochemical cell was measured independently and found to be ∼2 ms. Therefore, only the first 10 ms (equal to 5RC) of the black transient in Figure 8.6 is dominated by double layer charging. Figure 8.6 reveals a consistent slope (~ 1.5 s^{-1}) for the Au bead for the entire duration of the transient after the double layer charging, whereas the Au-ITO effectively has two slopes. At early times (20 ms $< t < 150$ ms) the slope is 15 s^{-1} and later times the slope is ∼0.5 s^{-1} (which is within a factor of 3 of the Au bead). The former value is very close to the apparent rate constant determined from the spectroscopic time-resolved ATR-SEIRAS experiments. These observations imply that there is a greater kinetic heterogeneity in the TEMPȮ SAMs formed on Au islands in the SEIRAS layer. The effect of kinetically heterogeneous redox sites on ET kinetics are extensively studied and is well known to give rise to fast sub-populations of redox centres.(167) Apparently, the dominant fraction of the SEIRAS substrate is occupied by these faster populations and are most likely related to the increased disorder in the TEMPȮ SAMs caused by the rougher surface texture of Au islands.(168; 169) SEM images in previous reports confirms about 50% greater roughness for the electrodeposited Au layer on ITO compared to that of Au bead electrode.(170)

8.3.4 Conclusions

This chapter primarily demonstrates the advantages of *in-situ* surface sensitive infrared studies to gather new information about molecular processes associated with ET reactions. This chapter provides a detailed IR spectral analysis of TEMPȮ and TEMPO$^+$, and unambiguously assigns the peak at 1624 cm^{-1} to N=O. ATR-SEIRAS were successfully employed to study the molecular reorientation associated with the redox reaction of TEMPȮ tethered monolayers. SEIRAS spectra reveals that the TEMPȮ centre undergoes a conformational change upon oxidation. The infrared response is consistent with a redox induced chair flip of the piperidinyl ring, such that the N=O group is projected further away from the electrode surface as compared to the radical. The above structural feature is associated with an increased absorbance from perchlorate counterions and non-hydrogen bonded water molecules. More details about the molecular events at the TEMPȮ-SAM redox layers were evident with the SEIRAS evaluation in combination with the electrochemical analysis. Lower rate constant values for the TEMPȮ oxidation (in the Tafel analysis) were attributed to the shift in the position of di-methyl substituents in the piperidinyl ring, during the chair-flip conformational change. Time-resolved

SEIRAS measurements indicated that the ingress of perchlorate ions into the redox centres as the initial molecular event and the conversion of N–O to N=O as the rate determining step of the over all ET process in the above studied TEMPȮ SAM system. Kinetic heterogeneity among the TEMPȮ redox centres on the rougher Au islands of SEIRAS film is also observed, which needs to be considered when extracting the ET rate constants solely from the basis of SEIRAS measurements.

9 Conclusions and outlook

9.1 Introduction

This chapter will summarize the overall research findings discussed in the chapters five to eight, in relation to the research objectives of this thesis. To reiterate, the primary objective of the thesis is the application of the EC-SEIRAS techniques, to complement conventional electrochemical techniques for time-resolved studies of various electrode-electrolyte interfaces. In doing so the thesis objective was to create a deeper knowledge of the structure and dynamics of well-organized molecular layers during ET processes. This chapter will discuss the key findings of electrochemical and SEIRAS studies of ferrocene SAM and $\text{TEMP}\dot{\text{O}}$ SAM systems and the contributions thereof, to the knowledge gap existing in this research area. It will also review the shortcomings of these studies and proposes opportunities for future research.

9.2 Key findings of the thesis

The CV features of the ferrocene SAM with various fractions of diluents shows that kinetic heterogeneity begins to become pronounced when the ferrocene coverage exceeds 1.44×10^{-10} mole cm^{-2}, which is $\sim 10\%$ of the self assembled monolayers (SAMs) of alkanethiol on the Au surface. Application of the deuterated diluents are reported here for the first time in literature, to track the fate of neighbouring alkane chain diluents with respect to the redox effect of ferrocene moieties. The EC-SEIRAS studies of ferrocene SAM with deuterated diluents provides a detailed picture of the molecular events during the oxidation reaction. The molecular model predicted using SEIRAS spectra supports many of the proposed features of ferrocene SAM found in literature. The predicated molecular model shows atleast four different (sub)molecular events occurring at the oxidation of ferrocene SAM. The first process is the conversion of ferrocene to ferrocenium ion as the result of electron transfer. The other processes include ion-pairing of Fc with counter ions along with the ingress of water molecules, tilting of the alkyl chain and the adjacent diluent molecules to an upright position. There is a clear spectral evidence for the rotation of cyclopentadiene rings along the Fc–C bond. Time-resolved EC-SEIRAS of the Fc-SAM system shows that ferrocene oxidation and ion pairing occurs first, followed by the alkyl chain tilt and the rotation of the ferrocene moieties.

The redox induced molecular behaviour of mixed monolayers of ferrocene SAM ($\text{FcC}_{11}\text{SH} + \text{C}_{10}\text{SH}$) in various electrolytes of increasing hydrophilicity ($\text{ClO}_4^- < \text{NO}_3^-$) was also studied. A clear positive shift in the redox formal potentials of ferrocene SAM is observed with NO_3^- counter ions. The faster ingress of perchlorate revealed in the time-resolved spectra is attributed to rapid accumulation of these hydrophobic counter ions during the double layer charging. Meanwhile, strongly solvated NO_3^- reaches only into the diffuse part of the double layer. Finally, the molecular reorientation of the ferrocene SAM occurred in similar fashion, irrespective of the nature of the electrolytes.

Apparently, the irregular packing density of the ferrocene units in the mixed monolayers on the Au surface significantly influences its electrochemical behaviour. BV and MHC theories for electron transfer processes are built under the assumption that all the redox centres at the electrochemical interface occupy identical environments, therefore, extracting kinetic parameters from kinetically heterogeneous redox-active SAMs leads to erroneous conclusions. To minimize kinetic heterogeneity, amino-ferrocenes are coupled with well-defined monolayers of alkanethiols with -COOH terminals, via EDC/NHS coupling reaction. Poor amide coupling lead to low loading of ferrocene on the alkanethiol monolayers. Therefore, ATR-SEIRAS technique was utilized to gain more insight about the EDC/NHS reaction, and thereby improve the amide coupling efficiency for fabricating well-ordered monolayers.

Multiple reaction pathways are proposed in the literature regarding the EDC/NHS reaction for the surface activation of acid-functionalized SAM terminals. However, the current literature lacked experimental evidence tracing the reaction intermediates to assert the proposed reaction pathways. In this thesis, the ATR-SEIRAS investigation of EDC/NHS surface activation reaction provided conclusive evidence for the existence of direct and indirect reaction pathways for the formation of NHS-ester. The reaction proceeds through the conversion of acid terminals to *O*-acylurea, an unstable intermediate, upon reaction with EDC. Direct conversion of *O*-acylurea to NHS-ester, in the presence of NHS, is pathway 1. Indirect conversion of *O*-acylurea to NHS-ester, by the formation of anhydride, is pathway 2. Even though, the hydrolysis of *O*-acylurea can form anhydride, the experimental evidence for the anhydride formation is not found in the literature survey. Presumably, for the first time, this study reports the existence of the short-lived anhydride (a peak at 1745 cm^{-1}) during the initial period of the reaction. It is a key evidence for reaction pathway 2 (indirect transformation of the *O*-acylurea to the NHS-ester). Potential dependent SEIRAS studies of EDC/NHS reaction reveals pathway 1 is preferred at negative potentials, whereas the reaction proceeds through pathway 2 at OCP and positive potentials. However, this study gives no compelling evidence to prove that altering the electrode potentials can increase the efficacy of the EDC/NHS reaction even though there is a potential dependency on the dominant pathway. It is interesting to note that even though the ferrocene loading via EDC/NHS reaction was not sufficient to carry out the SEIRAS measurements, the reaction with amino-TEMP$\dot{O}$ resulted in substantial coverage of the redox moieties with less kinetic heterogeneity.

With the knowledge acquired from the EDC/NHS reaction studies, an efficient protocol for the amide-coupling reaction was applied to covalently bond 4-amino TEMP$\dot{O}$ moieties to preformed acid terminated alkanethiol SAMs on Au surfaces. Based on the TEMP$\dot{O}$ coverage estimated from CV, approximately 20% of the undiluted carboxylic acid termini formed the amide linkage. The well-dispersed TEMP$\dot{O}$ SAM had non-interacting redox centres, hence these electroactive SAMs exhibited very little kinetic heterogeneity. The ET kinetics of TEMPȮ SAMs with varying alkanethiol chain length were studied with CV and chronocoulometric analysis. This study showcases the practical limitations of the CV based analysis (Laviron method) to extract the kinetic parameters for the redox SAM with fast electron transfer. The double-step chronocoulometric method applied to the TEMPȮ SAM system allows the accurate measurement of the standard ET rate constant as well as an estimation of the transfer coefficient at zero overpotential ($\alpha = 0.49 \pm 0.01$).

The SEIRAS studies of the TEMPȮ/TEMPO$^+$ couple presented here resolves the ambiguity in the assignment of TEMPO$^+$ peaks, especially the IR absorption peak that corresponds to the formation of N=O$^+$ during the oxidation of TEMPȮ SAM. Another notable finding in the TEMPȮ studies, is the slight asymmetry of the Tafel plot. The rate constant for the anodic reaction are consistently lower than the equivalent overpotential on the cathodic branch. Even though this observation is in tandem with the previous reports on ET analysis of TEMPȮ SAM, no justification for the asymmetric Tafel feature is found in the literature. Apparently, the conventional EC techniques are not suitable to provide insights about the interfacial molecular events leading to the asymmetric Tafel plot of TEMPȮ SAM. The EC-SEIRAS and time-resolved ATR-SEIRAS provided a molecular model in which TEMPȮ moieties undergoes a chair-flip conformational change during oxidation. This structural change expose the methyl groups of di-methyl substituents in the piperidinyl ring, to the redox plane and makes the N–O moieties less accessible to the counter ions. It could be the plausible reason for lower rate constant values for the anodic branch compared to the cathodic branch.

The double-step chronocoulometric analysis establishes an exponential decrease in the standard ET rate constants with increase in the chain length in the TEMPȮ SAM systems ($\beta = 0.96 \pm 0.04$ per methylene unit). The reorganization energy, estimated by fitting an exponential function, for the oxidized TEMPȮ moieties in C_{16}SH system is 1.1 ± 0.1 eV. With the same mathematical treatment, the reorganization energy of the oxidized TEMPȮ reported in literature for the C_{11}SH linkage is 1.45 ± 0.15 eV.(83)

9.3 Contributions to the scientific research

Cyclic voltammetry based techniques have been widely used to extract kinetic parameters for electron transfer processes. However, this thesis showcases the limitations of CV based kinetic analyses and provides a detailed mathematical framework for the double-step chronocoulometry analysis for the accurate extraction of kinetic parameters.

Even though the EDC/NHS amide coupling is a popular crosslinking method for biochemical conjugates and is widely reported for immobilizing electroactive species onto electrode surfaces, the literature lacks convincing evidence for multiple reaction pathways. This thesis used the EC-SEIRAS technique to monitor the EDC/NHS reaction *in-situ* and presents the first ever evidence of a potential dependency of the reaction pathways. The information about tunable reaction pathways of EDC/NHS reaction can be advantageous for selective immobilization of target analytes on a sensing platform.

The ET kinetic analysis of TEMPȮ provides experimental proof of the theoretical predictions of MHC with respect to the reorganization energy. The model predicts that, as the reorganization energy is made smaller, the rate constants reach limiting value sooner with increasing overpotentials and the plateau value is smaller. And it is experimentally observed that, long alkane chain TEMPȮ SAM with sluggish ET kinetics has lower reorganization energy compared to the the short alkane chain TEMPȮ SAM (reported in literature).

In situ studies at the electrochemical interface provide a static picture of the electrode processes. An in-depth knowledge of both the structure and dynamics of the electrochemical interface provides kinetic information of the electron transfer reactions, which is critical for improving electrochemical technologies. This thesis successfully demonstrates the application of time-resolved EC-SEIRAS studies to obtain both the structural and dynamics of the electrochemical interface. The static and time-resolved spectral information are combined with conventional electrochemical analysis to obtain a more dynamic description of the processes during the ET. It is evident that models that assume that the spacer region of the SAM are static during ET are inaccurate and that ET is followed by molecular reorganization of both the redox-active and inactive components of the monolayer.

9.4 Limitations of the study

Extracting kinetic information from experimental studies of redox-active SAMs typically relies on application of Butler-Volmer or Marcus-Hush-Chidsey theories with the assumption that all redox centres occupy identical environments. Even though less kinetic heterogeneity was observed with low ferrocene loading ($>$ 10% of SAM coverage), low ferrocene coverage resulted in poor SEIRAS spectral quality. Meanwhile, the EDC/NHS reaction between amino-ferrocene and COOH substituted alkanethiol monolayers were not effective to achieve high enough ferrocene loading levels required for a high quality SEIRAS spectra.

The ATR optical set-up required Au films of larger area (~ 0.25 cm^2), which resulted in the RC time constant of the electrochemical cell in the range of milliseconds. Therefore, studying redox-active SAM with shorter alkane chains were limited by the double layer charging current.

Desorption of the redox-active SAM layers at larger potential windows was another limitation of the ET studies. The SAM stability was compromised at larger overpotentials ($>$ 200 mV) around the formal potentials of the redox couple. In addition, a significant drop in the redox currents were observed with longer duration (over 5 hours) of potential cycling indicating SAM instability through oxidative desorption.

Even though Au films prepared on ITO layers showed superior mechanical stability over other SEIRAS film preparation methods including electroless deposition and sputtering, the ITO layers contribute to a higher capacitance (or larger RC charging time) to the electrochemical measurements. Moreover, SAM with defects in the packing are likely to form on the randomly deposited metallic islands. This leads to greater kinetic heterogeneity. Hence, a discrepancy was found in the standard rate constant of C_{12}SH-TEMPȮ SAM prepared on Au-ITO film and Au bead electrodes.

9.5 Future research

The position of the functional group in the molecular linkage between the redox centres and electrode can influence the ET process. This is due to the interaction between the neighbouring functional groups as well as the resultant orientation of the redox centres. Therefore, it will be interesting to study the similar TEMPȮ SAM system reported here, by altering the functional groups: amino-terminal alkanethiol SAM and the acid-substituted TEMPȮ. The influence of altered terminal groups in the monolayers, to the efficiency of amide coupling, will also be an interesting system for ATR-SEIRAS studies.

The ET kinetics become faster (on the order of microseconds) when the alkane chain length becomes shorter, and the molecular dynamics associated with faster ET process is not well-explored using EC-SEIRAS. These studies are mostly limited by the double layer charging of the larger area electrodes, in which the electrochemical cell holds larger RC time constant (in the order of milliseconds) than the time regime for the faster ET process. Morhart et al.(171) from the Burgess group, has reported the application of micro-band electrodes to study the electrochemical desorption of 4-methoxypyridine using time-resolved SEIRAS. Such a system can be well-adapted to study the faster ET processes, by modifying the micro-band electrode surface with short chain alkanethiol SAM and covalently link the TEMPȮ moieties.

Examining the TEMPȮ and ferrocene SAM systems reported here, in microsecond resolutions, can provide information about the elementary processes that could not be resolved in these studies. Time-resolved SEIRAS measurements using step-scan interferometry with good signal intensity requires larger data acquisition time (over 48 hours). Consistent electrochemical performance of these redox-active SAM on the SEIRAS film for a longer duration is challenging. Lins et al.(172) from the Burgess group has reported, for the first time, the application of dual-frequency comb IR spectroscopy in combination with ATR-SEIRAS to monitor the electrochemical interface for a simpler adsorption/desorption process. The measurement time required for dual-frequency comb IR spectroscopy is within 1-2 hours, and can achieve microsecond resolution. The major limitation is, the studies are possible only in the narrow spectral window of the frequency-comb lasers. Based on the spectroelectrochemical behaviour of TEMPȮ and ferrocene SAM reported in this thesis, meaningful measurements of aforesaid systems are possible with dual-frequency comb IR spectroscopy.

References

[1] K. Tu, *Developing Time-Resolved Synchrotron Infrared Spectroscopy for Spectroelectrochemical Measurements*. PhD thesis, University of Saskatchewan, College of Graduate Studies Research, 2020.

[2] F. Palazon, C. Montenegro Benavides, D. Léonard, Souteyrand, Y. Chevolot, and J.-P. Cloarec, "Carbodiimide/NHS derivatization of COOH-terminated SAMs: Activation or byproduct formation?," *Langmuir*, vol. 30, no. 16, pp. 4545–4550, 2014.

[3] S. Prabhulkar, H. Tian, X. Wang, J.-J. Zhu, and C.-Z. Li, "Engineered proteins: Redox properties and their applications," *Antioxidants & Redox Signaling*, vol. 17, no. 12, pp. 1796–1822, 2012.

[4] R. Marcus and N. Sutin, "Electron transfers in chemistry and biology," *Biochimica et Biophysica Acta (BBA) - Reviews on Bioenergetics*, vol. 811, no. 3, pp. 265–322, 1985.

[5] Molina and J. González, "Some fundamental concepts," in *Pulse Voltammetry in Physical Electrochemistry and Electroanalysis: Theory and Applications*, pp. 1–66, Springer International Publishing, 2016.

[6] S. Borgmann, G. Hartwich, A. Schulte, and W. Schuhmann, "Amperometric enzyme sensors based on direct and mediated electron transfer," in *Electrochemistry of Nucleic Acids and Proteins – Towards Electrochemical Sensors for Genomics and Proteomics* (E. Paleček, F. Scheller, and J. Wang, eds.), vol. 1 of *Perspectives in Bioanalysis*, pp. 599–655, Elsevier, 2005.

[7] Y. Zhai, Z. Zhu, S. Zhou, C. Zhu, and S. Dong, "Recent advances in spectroelectrochemistry," *Nanoscale*, vol. 10, pp. 3089–3111, 2018.

[8] A. J. Wain and M. A. O'Connell, "Advances in surface-enhanced vibrational spectroscopy at electrochemical interfaces," *Advances in Physics: X*, vol. 2, no. 1, pp. 188–209, 2017.

[9] D.-Y. Wu, J.-F. Li, B. Ren, and Z.-Q. Tian, "Electrochemical surface-enhanced raman spectroscopy of nanostructures," *Chemical Society Reviews*, vol. 37, no. 5, pp. 1025–1041, 2008.

[10] M. Fleischmann, P. Hendra, and A. McQuillan, "Raman spectra of pyridine adsorbed at a silver electrode," *Chemical Physics Letters*, vol. 26, no. 2, pp. 163–166, 1974.

[11] A. Hartstein, J. R. Kirtley, and J. C. Tsang, "Enhancement of the infrared absorption from molecular monolayers with thin metal overlayers," *Phys. Rev. Lett.*, vol. 45, pp. 201–204, 1980.

[12] M. Osawa and K.-i. Ataka, "Electromagnetic mechanism of enhanced infrared absorption of molecules adsorbed on metal island films," *Surface Science*, vol. 262, no. 3, pp. L118–L122, 1992.

[13] M. Osawa, K.-I. Ataka, K. Yoshii, and Y. Nishikawa, "Surface-enhanced infrared spectroscopy: The origin of the absorption enhancement and band selection rule in the infrared spectra of molecules adsorbed on fine metal particles," *Applied Spectroscopy*, vol. 47, no. 9, pp. 1497–1502, 1993.

[14] R. F. Aroca, D. J. Ross, and C. Domingo, "Surface-enhanced infrared spectroscopy," *Applied spectroscopy*, vol. 58, no. 11, pp. 324A–338A, 2004.

[15] R. G. Greenler, D. Snider, D. Witt, and R. Sorbello, "The metal-surface selection rule for infrared spectra of molecules adsorbed on small metal particles," *Surface Science*, vol. 118, no. 3, pp. 415–428, 1982.

[16] E. Kretschmann and H. Raether, "Notizen: Radiative decay of non radiative surface plasmons excited by light," *A Journal of Physical Sciences*, vol. 23, no. 12, pp. 2135–2136, 1968.

[17] A. Otto, "Excitation of nonradiative surface plasma waves in silver by the method of frustrated total reflection," *Zeitschrift für Physik A Hadrons and nuclei*, vol. 216, no. 4, pp. 398–410, 1968.

[18] N. Garcia-Araez, P. Rodriguez, V. Navarro, H. J. Bakker, and M. T. M. Koper, “Structural Effects on Water Adsorption on Gold Electrodes,” *The Journal of Physical Chemistry C*, vol. 115, no. 43, pp. 21249–21257, 2011.

[19] K.-i. Ataka and M. Osawa, “In situ infrared study of watersulfate coadsorption on gold(111) in sulfuric acid solutions,” *Langmuir*, vol. 14, no. 4, pp. 951–959, 1998.

[20] M. Osawa, M. Tsushima, H. Mogami, G. Samjeské, and A. Yamakata, “Structure of water at the electrified platinumwater interface: a study by surface-enhanced infrared absorption spectroscopy,” *The Journal of Physical Chemistry C*, vol. 112, no. 11, pp. 4248–4256, 2008.

[21] Y.-G. Yan, Y.-Y. Yang, B. Peng, S. Malkhandi, A. Bund, U. Stimming, and W.-B. Cai, “Study of co oxidation on polycrystalline pt electrodes in acidic solution by atr-seiras,” *The Journal of Physical Chemistry C*, vol. 115, no. 33, pp. 16378–16388, 2011.

[22] M. Shao and R. Adzic, “Electrooxidation of ethanol on a pt electrode in acid solutions: in situ atr-seiras study,” *Electrochimica Acta*, vol. 50, no. 12, pp. 2415–2422, 2005.

[23] M. Yoshida, A. Yamakata, K. Takanabe, J. Kubota, M. Osawa, and K. Domen, “Atr-seiras investigation of the fermi level of pt cocatalyst on a gan photocatalyst for hydrogen evolution under irradiation,” *Journal of the American Chemical Society*, vol. 131, no. 37, pp. 13218–13219, 2009.

[24] K. Ataka and J. Heberle, “Biochemical applications of surface-enhanced infrared absorption spectroscopy,” *Analytical and Bioanalytical Chemistry*, vol. 388, no. 1, pp. 47–54, 2007.

[25] K. Ataka, F. Giess, W. Knoll, R. Naumann, S. Haber-Pohlmeier, B. Richter, and J. Heberle, “Oriented attachment and membrane reconstitution of his-tagged cytochrome c oxidase to a gold electrode: in situ monitoring by surface-enhanced infrared absorption spectroscopy,” *Journal of the American Chemical Society*, vol. 126, no. 49, pp. 16199–16206, 2004.

[26] K. Ataka, B. Richter, and J. Heberle, “Orientational control of the physiological reaction of cytochrome c oxidase tethered to a gold electrode,” *The Journal of Physical Chemistry B*, vol. 110, no. 18, pp. 9339–9347, 2006.

[27] A. J. Bard and L. R. Faulkner, “Fundamentals and applications,” *Electrochemical Methods*, vol. 2, no. 482, pp. 580–632, 2001.

[28] E. T. Nibbering, H. Fidder, and E. Pines, “ULTRAFAST CHEMISTRY: Using time-resolved vibrational spectroscopy for interrogation of structural dynamics,” *Annual Review of Physical Chemistry*, vol. 56, no. 1, pp. 337–367, 2005.

[29] J. A. V. Butler, “Studies in heterogeneous equilibria. part II.—the kinetic interpretation of the nernst theory of electromotive force,” *Transactions of the Faraday Society*, vol. 19, pp. 729–733, 1924.

[30] T. Erdey-Grúz and M. Volmer, “On the theory of hydrogen surge,” *Journal of Physical Chemistry*, vol. 150, no. 1, pp. 203–213, 1930.

[31] S. W. Feldberg, “Implications of marcushush theory for steady-state heterogeneous electron transfer at an inlaid disk electrode,” *Analytical Chemistry*, vol. 82, no. 12, pp. 5176–5183, 2010.

[32] J. Savéant and D. Tessier, “Convolution potential sweep voltammetry v. determination of charge transfer kinetics deviating from the butler-volmer behaviour,” *Journal of Electroanalytical Chemistry and Interfacial Electrochemistry*, vol. 65, no. 1, pp. 57–66, 1975.

[33] R. A. Marcus, “On the theory of oxidation-reduction reactions involving electron transfer. i,” *The Journal of Chemical Physics*, vol. 24, no. 5, pp. 966–978, 1956.

[34] N. S. Hush, “Adiabatic rate processes at electrodes. i. energy-charge relationships,” *The Journal of Chemical Physics*, vol. 28, no. 5, pp. 962–972, 1958.

[35] B. S. Brunschwig and N. Sutin, “Energy surfaces, reorganization energies, and coupling elements in electron transfer,” *Coordination Chemistry Reviews*, vol. 187, no. 1, pp. 233–254, 1999.

[36] P. F. Barbara, T. J. Meyer, and M. A. Ratner, “Contemporary issues in electron transfer research,” *The Journal of Physical Chemistry*, vol. 100, no. 31, pp. 13148–13168, 1996.

[37] R. A. Marcus, “Electron transfer reactions in chemistry. theory and experiment,” *Rev. Mod. Phys.*, vol. 65, pp. 599–610, 1993.

[38] J. R. Miller, L. T. Calcaterra, and G. L. Closs, “Intramolecular long-distance electron transfer in radical anions. the effects of free energy and solvent on the reaction rates,” *Journal of the American Chemical Society*, vol. 106, no. 10, pp. 3047–3049, 1984.

[39] C. E. D. Chidsey, “Free energy and temperature dependence of electron transfer at the metal-electrolyte interface,” *Science*, vol. 251, no. 4996, pp. 919–922, 1991.

[40] B. J. Hales, “Temperature dependency of the rate of electron transport as a monitor of protein motion,” *Biophysical journal*, vol. 16, no. 5, pp. 471–480, 1976.

[41] H. B. Gray and J. R. Winkler, “Long-range electron transfer,” *Proceedings of the National Academy of Sciences of the United States of America*, vol. 102, no. 10, p. 3534, 2005.

[42] J. F. Smalley, H. O. Finklea, C. E. D. Chidsey, M. R. Linford, S. E. Creager, J. P. Ferraris, K. Chalfant, T. Zawodzinsk, S. W. Feldberg, and M. D. Newton, “Heterogeneous electron-transfer kinetics for ruthenium and ferrocene redox moieties through alkanethiol monolayers on gold,” *Journal of the American Chemical Society*, vol. 125, no. 7, pp. 2004–2013, 2003.

[43] H. O. Finklea and D. D. Hanshew, “Electron-transfer kinetics in organized thiol monolayers with attached pentaammine(pyridine)ruthenium redox centers,” *Journal of the American Chemical Society*, vol. 114, no. 9, pp. 3173–3181, 1992.

[44] W. B. Davis, W. A. Svec, M. A. Ratner, and M. R. Wasielewski, “Molecular-wire behaviour in p -phenylenevinylene oligomers,” *Nature*, vol. 396, no. 6706, pp. 60–63, 1998.

[45] C. D. Bain, H. A. Biebuyck, and G. M. Whitesides, “Comparison of self-assembled monolayers on gold: coadsorption of thiols and disulfides,” *Langmuir*, vol. 5, no. 3, pp. 723–727, 1989.

[46] R. G. Nuzzo, B. R. Zegarski, and L. H. Dubois, “Fundamental studies of the chemisorption of organosulfur compounds on gold(111). implications for molecular self-assembly on gold surfaces,” *Journal of the American Chemical Society*, vol. 109, no. 3, pp. 733–740, 1987.

[47] W. Schmickler and E. Santos, “Electrochemical surface processes,” in *Interfacial Electrochemistry* (W. Schmickler and E. Santos, eds.), pp. 195–206, Springer Berlin Heidelberg, 2010.

[48] J. C. Love, L. A. Estroff, J. K. Kriebel, R. G. Nuzzo, and G. M. Whitesides, “Self-assembled monolayers of thiolates on metals as a form of nanotechnology,” *Chemical Reviews*, vol. 105, no. 4, pp. 1103–1170, 2005.

[49] A. Ulman, “Formation and structure of self-assembled monolayers,” *Chemical Reviews*, vol. 96, no. 4, pp. 1533–1554, 1996.

[50] F. Schreiber, “Structure and growth of self-assembling monolayers,” *Progress in Surface Science*, vol. 65, no. 5, pp. 151–257, 2000.

[51] M. Himmelhaus, F. Eisert, M. Buck, and M. Grunze, “Self assembly of n alkanethiol monolayers a study by ir visible sum frequency spectroscopy (sfg),” *The Journal of Physical Chemistry B*, vol. 104, no. 3, pp. 576–584, 2000.

[52] O. Dannenberger, M. Buck, and M. Grunze, “Self-assembly of n-alkanethiols a kinetic study by second harmonic generation,” *The Journal of Physical Chemistry B*, vol. 103, no. 12, pp. 2202–2213, 1999.

[53] J. B. Schlenoff, M. Li, and H. Ly, "Stability and self-exchange in alkanethiol monolayers," *Journal of the American Chemical Society*, vol. 117, no. 50, pp. 12528–12536, 1995.

[54] R. G. Nuzzo and D. L. Allara, "Adsorption of bifunctional organic disulfides on gold surfaces," *Journal of the American Chemical Society*, vol. 105, no. 13, pp. 4481–4483, 1983.

[55] M. Twardowski and R. G. Nuzzo, "Chemically mediated grain growth in nanotextured au, novel substrates for the formation of self-assembled monolayers," *Langmuir*, vol. 18, no. 14, pp. 5529–5538, 2002.

[56] J. Hautman and M. L. Klein, "Simulation of a monolayer of alkyl thiol chains," *The Journal of Chemical Physics*, vol. 91, no. 8, pp. 4994–5001, 1989.

[57] N. Camillone, C. E. D. Chidsey, G. Liu, and G. Scoles, "Substrate dependence of the surface structure and chain packing of docosyl mercaptan self-assembled on the (111), (110), and (100) faces of single crystal gold," *The Journal of Chemical Physics*, vol. 98, no. 5, pp. 4234–4245, 1993.

[58] H. Sellers, A. Ulman, Y. Shnidman, and J. E. Eilers, "Structure and binding of alkanethiolates on gold and silver surfaces: implications for self-assembled monolayers," *Journal of the American Chemical Society*, vol. 115, no. 21, pp. 9389–9401, 1993.

[59] C. A. Widrig, C. A. Alves, and M. D. Porter, "Scanning tunneling microscopy of ethanethiolate and n-octadecanethiolate monolayers spontaneously absorbed at gold surfaces," *Journal of the American Chemical Society*, vol. 113, no. 8, pp. 2805–2810, 1991.

[60] A. Ulman, J. E. Eilers, and N. Tillman, "Packing and molecular orientation of alkanethiol monolayers on gold surfaces," *Langmuir*, vol. 5, no. 5, pp. 1147–1152, 1989.

[61] L. H. Dubois and R. G. Nuzzo, "Synthesis, structure, and properties of model organic surfaces," *Annual Review of Physical Chemistry*, vol. 43, no. 1, pp. 437–463, 1992.

[62] M. D. Porter, T. B. Bright, D. L. Allara, and C. E. D. Chidsey, "Spontaneously organized molecular assemblies. 4. structural characterization of n-alkyl thiol monolayers on gold by optical ellipsometry, infrared spectroscopy, and electrochemistry," *Journal of the American Chemical Society*, vol. 109, no. 12, pp. 3559–3568, 1987.

[63] G. Liu, P. Fenter, C. E. D. Chidsey, D. F. Ogletree, P. Eisenberger, and M. Salmeron, "An unexpected packing of fluorinated n-alkane thiols on au(111): A combined atomic force microscopy and x-ray diffraction study," *The Journal of Chemical Physics*, vol. 101, no. 5, pp. 4301–4306, 1994.

[64] L. H. Dubois, B. R. Zegarski, and R. G. Nuzzo, "Molecular ordering of organosulfur compounds on au(111) and au(100) adsorption from solution and in ultrahigh vacuum," *The Journal of Chemical Physics*, vol. 98, no. 1, pp. 678–688, 1993.

[65] R. G. Nuzzo, E. M. Korenic, and L. H. Dubois, "Studies of the temperature-dependent phase behavior of long chain n-alkyl thiol monolayers on gold," *The Journal of Chemical Physics*, vol. 93, no. 1, pp. 767–773, 1990.

[66] N. Camillone, C. E. D. Chidsey, G. Liu, T. M. Putvinski, and G. Scoles, "Surface structure and thermal motion of n-alkane thiols self-assembled on au(111) studied by low energy helium diffraction," *The Journal of Chemical Physics*, vol. 94, no. 12, pp. 8493–8502, 1991.

[67] F. Tao and S. L. Bernasek, "Understanding odd even effects in organic self-assembled monolayers," *Chemical Reviews*, vol. 107, no. 5, pp. 1408–1453, 2007.

[68] G. Yang and G.-y. Liu, "New insights for self-assembled monolayers of organothiols on au(111) revealed by scanning tunneling microscopy," *The Journal of Physical Chemistry B*, vol. 107, no. 34, pp. 8746–8759, 2003.

[69] P. Häberle, P. Fenter, and T. Gustafsson, “Structure of the cs-induced (1×3) reconstruction of au(110),” *Phys. Rev. B*, vol. 39, pp. 5810–5818, 1989.

[70] R. G. Nuzzo, L. H. Dubois, and D. L. Allara, “Fundamental studies of microscopic wetting on organic surfaces. 1. formation and structural characterization of a self-consistent series of polyfunctional organic monolayers,” *Journal of the American Chemical Society*, vol. 112, no. 2, pp. 558–569, 1990.

[71] T. P. Sullivan and W. T. S. Huck, “Reactions on monolayers: Organic synthesis in two dimensions,” *European Journal of Organic Chemistry*, vol. 2003, no. 1, pp. 17–29, 2003.

[72] M. C. Henstridge, E. Laborda, N. V. Rees, and R. G. Compton, “Marcus–hush–chidsey theory of electron transfer applied to voltammetry: A review,” *Electrochimica Acta*, vol. 84, pp. 12–20, 2012.

[73] E. Laborda, M. C. Henstridge, C. Batchelor-McAuley, and R. G. Compton, “Asymmetric marcus–hush theory for voltammetry,” *Chemical Society Reviews*, vol. 42, no. 12, pp. 4894–4905, 2013.

[74] J. F. Smalley, S. W. Feldberg, C. E. D. Chidsey, M. R. Linford, M. D. Newton, and Y.-P. Liu, “The Kinetics of Electron Transfer Through Ferrocene-Terminated Alkanethiol Monolayers on Gold,” *The Journal of Physical Chemistry*, vol. 99, no. 35, pp. 13141–13149, 1995.

[75] G. K. Rowe, M. T. Carter, J. N. Richardson, and R. W. Murray, “Consequences of kinetic dispersion on the electrochemistry of an adsorbed redox-active monolayer,” *Langmuir*, vol. 11, no. 5, pp. 1797–1806, 1995.

[76] S. B. Sachs, S. P. Dudek, R. P. Hsung, L. R. Sita, J. F. Smalley, M. D. Newton, S. W. Feldberg, and C. E. D. Chidsey, “Rates of Interfacial Electron Transfer through Conjugated Spacers,” *Journal of the American Chemical Society*, vol. 119, no. 43, pp. 10563–10564, 1997.

[77] J. J. Sumner, K. S. Weber, L. A. Hockett, and S. E. Creager, “Long-Range Heterogeneous Electron Transfer Between Ferrocene and Gold Mediated By n-Alkane and N-Alkyl-Carboxamide Bridges,” *The Journal of Physical Chemistry B*, vol. 104, no. 31, pp. 7449–7454, 2000.

[78] J. J. Sumner and S. E. Creager, “Redox kinetics in monolayers on electrodes: electron transfer is sluggish for ferrocene groups buried within the monolayer interior,” *The Journal of Physical Chemistry B*, vol. 105, no. 37, pp. 8739–8745, 2001.

[79] M. S. Ravenscroft and H. O. Finklea, “Kinetics of electron transfer to attached redox centers on gold electrodes in nonaqueous electrolytes,” *The Journal of Physical Chemistry*, vol. 98, no. 14, pp. 3843–3850, 1994.

[80] H. O. Finklea, L. Liu, M. S. Ravenscroft, and S. Punturi, “Multiple electron tunneling paths across self-assembled monolayers of alkanethiols with attached ruthenium(II/III) redox centers,” *The Journal of Physical Chemistry*, vol. 100, no. 48, pp. 18852–18858, 1996.

[81] Liu, M. N. Paddon-Row, and J. J. Gooding, “Heterogeneous electron-transfer kinetics for flavin adenine dinucleotide and ferrocene through alkanethiol mixed monolayers on gold electrodes,” *The Journal of Physical Chemistry B*, vol. 108, no. 24, pp. 8460–8466, 2004.

[82] S. E. Creager and G. K. Rowe, “Solvent and double-layer effects on redox reactions in self-assembled monolayers of ferrocenyl—alkanethiolates on gold,” *Journal of Electroanalytical Chemistry*, vol. 420, no. 1, pp. 291–299, 1997.

[83] H. O. Finklea and N. Madhiri, “Reorganization energies of TEMPO/TEMPO+ in water,” *Journal of Electroanalytical Chemistry*, vol. 621, no. 2, pp. 129–133, 2008.

[84] N. Elgrishi, K. J. Rountree, B. D. McCarthy, E. S. Rountree, T. T. Eisenhart, and J. L. Dempsey, “A practical beginner’s guide to cyclic voltammetry,” *Journal of Chemical Education*, vol. 95, no. 2, pp. 197–206, 2018.

[85] K. Tokuda, T. Gueshi, and H. Matsuda, “Voltammetry at partially covered electrodes: Part III. faradaic impedance measurements at model electrodes,” *Journal of Electroanalytical Chemistry and Interfacial Electrochemistry*, vol. 102, no. 1, pp. 41–48, 1979.

[86] K. Weber, L. Hockett, and S. Creager, “Long-Range Electronic Coupling between Ferrocene and Gold in Alkanethiolate-based Monolayers on Electrodes,” *The Journal of Physical Chemistry B*, vol. 101, no. 41, pp. 8286–8291, 1997.

[87] J. H. Christie, R. A. Osteryoung, and F. C. Amson, “Application of double potential-step chronocoulometry to the study of reactant adsorption. theory,” *Journal of Electroanalytical Chemistry and Interfacial Electrochemistry*, vol. 13, no. 3, pp. 236–244, 1967.

[88] K. Ashley and S. Pons, “Infrared spectroelectrochemistry,” *Chemical Reviews*, vol. 88, no. 4, pp. 673–695, 1988.

[89] P. Su, V. Prabhakaran, G. E. Johnson, and J. Laskin, “In situ infrared spectroelectrochemistry for understanding structural transformations of precisely defined ions at electrochemical interfaces,” *Analytical Chemistry*, vol. 90, no. 18, pp. 10935–10942, 2018.

[90] M. Osawa, K. ichi Ataka, K. Yoshii, and T. Yotsuyanagi, “Surface-enhanced infrared atr spectroscopy for in situ studies of electrode/electrolyte interfaces,” *Journal of Electron Spectroscopy and Related Phenomena*, vol. 64-65, pp. 371–379, 1993.

[91] J. R. Sambles, G. W. Bradbery, and F. Yang, “Optical excitation of surface plasmons: An introduction,” *Contemporary Physics*, vol. 32, no. 3, pp. 173–183, 1991.

[92] M. Osawa and M. Ikeda, “Surface-enhanced infrared absorption of p-nitrobenzoic acid deposited on silver island films: contributions of electromagnetic and chemical mechanisms,” *The Journal of Physical Chemistry*, vol. 95, no. 24, pp. 9914–9919, 1991.

[93] B. N. J. Persson and R. Ryberg, “Vibrational interaction between molecules adsorbed on a metal surface: The dipole-dipole interaction,” *Phys. Rev. B*, vol. 24, pp. 6954–6970, 1981.

[94] H. Pearce and N. Sheppard, “Possible importance of a “metal-surface selection rule” in the interpretation of the infrared spectra of molecules adsorbed on particulate metals; infrared spectra from ethylene chemisorbed on silica-supported metal catalysts,” *Surface Science*, vol. 59, no. 1, pp. 205–217, 1976.

[95] M. Moskovits, “Surface-enhanced spectroscopy,” *Rev. Mod. Phys.*, vol. 57, pp. 783–826, 1985.

[96] A. Quirk, B. Unni, and I. J. Burgess, “Surface enhanced infrared studies of 4-methoxypyridine adsorption on gold film electrodes,” *Langmuir*, vol. 32, no. 9, pp. 2184–2191, 2016.

[97] J. M. Delgado, J. M. Orts, J. M. Pérez, and A. Rodes, “Sputtered thin-film gold electrodes for in situ atr-seiras and sers studies,” *Journal of Electroanalytical Chemistry*, vol. 617, no. 2, pp. 130–140, 2008.

[98] D.-J. Chen, B. Xu, S.-G. Sun, and Y. J. Tong, “Electroless deposition of ultrathin au film for surface enhanced in situ spectroelectrochemisrty and reaction-driven surface reconstruction for oxygen reduction reaction,” *Catalysis Today*, vol. 182, no. 1, pp. 46–53, 2012.

[99] O. J. R. Clarke and I. J. Burgess, “Electrodeposited gold nanodaggers on conductive metal oxide films provide substrates for dual-modality surface sensitive vibrational spectroscopy,” *The Journal of Physical Chemistry C*, vol. 124, no. 24, pp. 13356–13364, 2020.

[100] I. R. Andvaag, E. Lins, and I. J. Burgess, “An effective medium theory description of surface-enhanced infrared absorption from metal island layers grown on conductive metal oxide films,” *The Journal of Physical Chemistry C*, vol. 125, no. 40, pp. 22301–22311, 2021.

[101] A. Paul, R. Borrelli, H. Bouyanfif, S. Gottis, and F. Sauvage, “Tunable redox potential, optical properties, and enhanced stability of modified ferrocene-based complexes,” *ACS Omega*, vol. 4, no. 12, pp. 14780–14789, 2019.

[102] D. Taherinia, "Investigation of the interfacial electron transfer kinetics in ferrocene-terminated oligophenyleneimine self-assembled monolayers," *Langmuir*, vol. 36, no. 42, pp. 12572–12579, 2020.

[103] S. Chattopadhyay, S. Bandyopadhyay, and A. Dey, "Kinetic isotope effects on electron transfer across self-assembled monolayers on gold," *Inorganic Chemistry*, vol. 60, no. 2, pp. 597–605, 2021.

[104] S. M. Batterjee, M. I. Marzouk, M. E. Aazab, and M. A. El-Hashash, "The electrochemistry of some ferrocene derivatives: redox potential and substituent effects," *Applied Organometallic Chemistry*, vol. 17, no. 5, pp. 291–297, 2003.

[105] C. Fontanesi, E. D. Como, D. Vanossi, M. Montecchi, M. Cannio, P. C. Mondal, W. Giurlani, M. Innocenti, and L. Pasquali, "Redox-active ferrocene grafted on h-terminated si(111): Electrochemical characterization of the charge transport mechanism and dynamics," *Scientific Reports*, vol. 9, no. 1, p. 8735, 2019.

[106] E. Laviron, "General expression of the linear potential sweep voltammogram in the case of diffusionless electrochemical systems," *Journal of Electroanalytical Chemistry and Interfacial Electrochemistry*, vol. 101, no. 1, pp. 19–28, 1979.

[107] C. E. D. Chidsey, C. R. Bertozzi, T. M. Putvinski, and A. M. Mujsce, "Coadsorption of ferrocene-terminated and unsubstituted alkanethiols on gold: electroactive self-assembled monolayers," *Journal of the American Chemical Society*, vol. 112, no. 11, pp. 4301–4306, 1990.

[108] A. V. Rudnev, U. Zhumaev, T. Utsunomiya, C. Fan, Y. Yokota, K.-i. Fukui, and T. Wandlowski, "Ferrocene-terminated alkanethiol self-assembled monolayers: An electrochemical and in situ surface-enhanced infra-red absorption spectroscopy study," *Electrochimica Acta*, vol. 107, pp. 33–44, 2013.

[109] S. Ye, Y. Sato, and K. Uosaki, "Redox-induced orientation change of a self-assembled monolayer of 11-ferrocenyl-1-undecanethiol on a gold electrode studied by in situ FT-IRRAS," *Langmuir*, vol. 13, no. 12, pp. 3157–3161, 1997.

[110] A. Viana, A. Jones, L. Abrantes, and M. Kalaji, "Redox induced orientational changes in a series of short chain ferrocenyl alkyl thiols self-assembled on gold(111) electrodes," *Journal of Electroanalytical Chemistry*, vol. 500, no. 1, pp. 290–298, 2001.

[111] X. Jiang, A. Zuber, J. Heberle, and K. Ataka, "In situ monitoring of the orientated assembly of strep-tagged membrane proteins on the gold surface by surface enhanced infrared absorption spectroscopy," *Phys. Chem. Chem. Phys.*, vol. 10, pp. 6381–6387, 2008.

[112] T. P. Sullivan and W. T. S. Huck, "Reactions on monolayers: Organic synthesis in two dimensions," *European Journal of Organic Chemistry*, vol. 2003, no. 1, pp. 17–29, 2003.

[113] E. Valeur and M. Bradley, "Amide bond formation: beyond the myth of coupling reagents," *Chemical Society Reviews*, vol. 38, no. 2, pp. 606–631, 2009.

[114] L. Yan, C. Marzolin, A. Terfort, and G. M. Whitesides, "Formation and reaction of interchain carboxylic anhydride groups on self-assembled monolayers on gold," *Langmuir*, vol. 13, no. 25, pp. 6704–6712, 1997.

[115] J. W. Lee, S. J. Sim, S. M. Cho, and J. Lee, "Characterization of a self-assembled monolayer of thiol on a gold surface and the fabrication of a biosensor chip based on surface plasmon resonance for detecting anti-GAD antibody," *Biosensors and Bioelectronics*, vol. 20, no. 7, pp. 1422–1427, 2005.

[116] N. Patel, M. C. Davies, M. Hartshorne, R. J. Heaton, C. J. Roberts, S. J. B. Tendler, and P. M. Williams, "Immobilization of protein molecules onto homogeneous and mixed carboxylate-terminated self-assembled monolayers," *Langmuir*, vol. 13, no. 24, pp. 6485–6490, 1997.

[117] L.-S. Jang and H.-K. Keng, "Modified fabrication process of protein chips using a short-chain self-assembled monolayer," *Biomedical Microdevices*, vol. 10, no. 2, pp. 203–211, 2008.

[118] J. V. Staros, R. W. Wright, and D. M. Swingle, “Enhancement by n-hydroxysulfosuccinimide of water-soluble carbodiimide-mediated coupling reactions,” *Analytical Biochemistry*, vol. 156, no. 1, pp. 220–222, 1986.

[119] S. Sam, L. Touahir, J. Salvador Andresa, P. Allongue, J.-N. Chazalviel, A. C. Gouget-Laemmel, C. Henry de Villeneuve, A. Moraillon, F. Ozanam, N. Gabouze, and S. Djebbar, “Semiquantitative study of the EDC/NHS activation of acid terminal groups at modified porous silicon surfaces,” *Langmuir*, vol. 26, no. 2, pp. 809–814, 2010.

[120] T.-C. Tsai, C.-W. Liu, Y.-C. Wu, N. A. P. Ondevilla, M. Osawa, and H.-C. Chang, “In situ study of EDC/NHS immobilization on gold surface based on attenuated total reflection surface-enhanced infrared absorption spectroscopy (ATR-SEIRAS),” *Colloids and Surfaces B: Biointerfaces*, vol. 175, pp. 300–305, 2019.

[121] B. L. Frey and R. M. Corn, “Covalent attachment and derivatization of poly (l-lysine) monolayers on gold surfaces as characterized by polarization modulation FT-IR spectroscopy,” *Analytical Chemistry*, vol. 68, no. 18, pp. 3187–3193, 1996.

[122] V. M. Mirsky, M. Riepl, and O. S. Wolfbeis, “Capacitive monitoring of protein immobilization and antigen–antibody reactions on monomolecular alkylthiol films on gold electrodes,” *Biosensors and Bioelectronics*, vol. 12, no. 9, pp. 977–989, 1997.

[123] A. Faucheux, A. C. Gouget-Laemmel, C. Henry de Villeneuve, R. Boukherroub, F. Ozanam, P. Allongue, and J.-N. Chazalviel, “Well-defined carboxyl-terminated alkyl monolayers grafted onto hsi(111): packing density from a combined AFM and quantitative IR study,” *Langmuir*, vol. 22, no. 1, pp. 153–162, 2006.

[124] N. Nakajima and Y. Ikada, “Mechanism of Amide Formation by Carbodiimide for Bioconjugation in Aqueous Media,” *Bioconjugate Chemistry*, vol. 6, no. 1, pp. 123–130, 1995.

[125] S. M. Rosendahl and I. J. Burgess, “Electrochemical and infrared spectroscopy studies of 4-mercaptobenzoic acid sams on gold surfaces,” *Electrochimica Acta*, vol. 53, no. 23, pp. 6759–6767, 2008.

[126] S. Fukuzumi, Y.-M. Lee, and W. Nam, “Immobilization of molecular catalysts for enhanced redox catalysis,” *ChemCatChem*, vol. 10, no. 8, pp. 1686–1702, 2018.

[127] I. Mazurenko, V. P. Hitaishi, and E. Lojou, “Recent advances in surface chemistry of electrodes to promote direct enzymatic bioelectrocatalysis,” *Current Opinion in Electrochemistry*, vol. 19, pp. 113–121, 2020.

[128] R. M. Bullock, A. K. Das, and A. M. Appel, “Surface immobilization of molecular electrocatalysts for energy conversion,” *Chemistry – A European Journal*, vol. 23, no. 32, pp. 7626–7641, 2017.

[129] D. Gatteschi, A. Cornia, M. Mannini, and R. Sessoli, “Organizing and addressing magnetic molecules,” *Inorganic Chemistry*, vol. 48, no. 8, pp. 3408–3419, 2009.

[130] E. Di Piazza, A. Merhi, L. Norel, S. Choua, P. Turek, and S. Rigaut, “Ruthenium carbon-rich complexes as redox switchable metal coupling units,” *Inorganic Chemistry*, vol. 54, no. 13, pp. 6347–6355, 2015.

[131] S. Goldstein, G. Merenyi, A. Russo, and A. Samuni, “The role of oxoammonium cation in the sod-mimic activity of cyclic nitroxides,” *Journal of the American Chemical Society*, vol. 125, no. 3, pp. 789–795, 2003.

[132] R. A. Sheldon and I. W. C. E. Arends, “Catalytic oxidations mediated by metal ions and nitroxyl radicals,” *Journal of Molecular Catalysis A: Chemical*, vol. 251, no. 1, pp. 200–214, 2006.

[133] Y. Kashiwagi, K. Uchiyama, F. Kurashima, J. ichi Anzai, and T. Osa, “Enantioselective oxidation of amines on a gold electrode modified by a self-assembled monolayer of a chiral nitroxyl radical compound,” *Analytical Sciences*, vol. 15, no. 9, pp. 907–909, 1999.

[134] T. Fuchigami, T. Shintani, A. Konno, S. Higashiya, and T. Nonaka, “Preparation of a stable self-assembled thiol-modified electrode having immobilized 2,2,6,6-tetramethylpiperidinyl-1-oxyl (tempo) and its application to electrocatalysis,” *Electrochemistry and industrial physical chemistry*, vol. 65, no. 6, pp. 506–507, 1997.

[135] O. Alévêque, F. Seladji, C. Gautier, M. Dias, T. Breton, and E. Levillain, “Nitroxyl radical self-assembled monolayers on gold: Versatile electroactive centers in aqueous and organic media,” *ChemPhysChem*, vol. 10, no. 14, pp. 2401–2404, 2009.

[136] O. Alévêque, P.-Y. Blanchard, T. Breton, M. Dias, C. Gautier, E. Levillain, and F. Seladji, “Nitroxyl radical self-assembled monolayers on gold: Experimental data vs. laviron’s interaction model,” *Electrochemistry Communications*, vol. 11, no. 9, pp. 1776–1780, 2009.

[137] G. Grampp and K. Rasmussen, “Solvent dynamical effects on the electron self-exchange rate of the TEMPO$^{\cdot}$/TEMPO+ couple (TEMPO = 2,2,6,6-tetramethyl-1-piperidinyloxy radical) part i. ESR-linebroadening measurements at t = 298 k,” *Phys. Chem. Chem. Phys.*, vol. 4, no. 22, pp. 5546–5549, 2002.

[138] J. R. Fish, S. G. Swarts, M. D. Sevilla, and T. Malinski, “Electrochemistry and spectroelectrochemistry of nitroxyl free radicals,” *The Journal of Physical Chemistry*, vol. 92, no. 13, pp. 3745–3751, 1988.

[139] Y. Kato, Y. Shimizu, L. Yijing, K. Unoura, H. Utsumi, and T. Ogata, “Reversible half-wave potentials of reduction processes on nitroxide radicals,” *Electrochimica Acta*, vol. 40, no. 17, pp. 2799–2802, 1995.

[140] C. D. Bain, E. B. Troughton, Y. T. Tao, J. Evall, G. M. Whitesides, and R. G. Nuzzo, “Formation of monolayer films by the spontaneous assembly of organic thiols from solution onto gold,” *Journal of the American Chemical Society*, vol. 111, no. 1, pp. 321–335, 1989.

[141] B. Dordi, H. Schonherr, and G. J. Vancso, “Reactivity in the confinement of self-assembled monolayers:chain length effects on the hydrolysis of n-hydroxysuccinimide ester disulfides on gold,” *Langmuir*, vol. 19, no. 14, pp. 5780–5786, 2003.

[142] O. Alévêque, P.-Y. Blanchard, T. Breton, M. Dias, C. Gautier, and E. Levillain, “Revisiting the determination of full steady-state coverage of redox centers on self-assembled monolayers,” *Electrochemistry communications*, vol. 16, no. 1, pp. 6–9, 2012.

[143] N. Nerngchamnong, D. Thompson, L. Cao, L. Yuan, L. Jiang, M. Roemer, and C. A. Nijhuis, “Nonideal electrochemical behavior of ferrocenyl–alkanethiolate SAMs maps the microenvironment of the redox unit,” *The Journal of Physical Chemistry C*, vol. 119, no. 38, pp. 21978–21991, 2015.

[144] O. Alévêque, P.-Y. Blanchard, C. Gautier, M. Dias, T. Breton, and E. Levillain, “Electroactive self-assembled monolayers: Laviron’s interaction model extended to non-random distribution of redox centers,” *Electrochemistry communications*, vol. 12, no. 11, pp. 1462–1466, 2010.

[145] O. Alévêque, C. Gautier, M. Dias, T. Breton, and E. Levillain, “Phase segregation on electroactive self-assembled monolayers: a numerical approach for describing lateral interactions between redox centers,” *Physical Chemistry Chemical Physics*, vol. 12, no. 39, pp. 12584–12590, 2010.

[146] W. Zhang, S. M. Rosendahl, and I. J. Burgess, “Coupled Electron/Proton Transfer Studies of Benzoquinone-Modified Monolayers,” *The Journal of Physical Chemistry C*, vol. 114, no. 6, pp. 2738–2745, 2010.

[147] J. Gonzalez and J. Sequí-Castellano, “Electrochemical determination of kinetic parameters of surface confined redox probes in presence of intermolecular interactions by means of Cyclic Voltammetry. Application to TEMPO monolayers in gold and platinum electrodes,” *Electrochimica Acta*, vol. 365, p. 137331, 2021.

[148] F. Ben Amara, E. R. Dionne, S. Kassir, C. Pellerin, and A. Badia, “Molecular Origin of the Odd–Even Effect of Macroscopic Properties of n-Alkanethiolate Self-Assembled Monolayers: Bulk or Interface?,” *Journal of the American Chemical Society*, vol. 142, no. 30, pp. 13051–13061, 2020.

[149] S. Ghosh and S. Hammes-Schiffer, “Calculation of electrochemical reorganization energies for redox molecules at self-assembled monolayer modified electrodes,” *The Journal of Physical Chemistry Letters*, vol. 6, no. 1, pp. 1–5, 2015.

[150] H. Noda, K. Ataka, L.-J. Wan, and M. Osawa, “Time-resolved surface-enhanced infra-red study of molecular adsorption at the electrochemical interface,” *Surface Science*, vol. 427-428, pp. 190–194, 1999.

[151] K. Tu, M. J. Lardner, T. A. Morhart, S. M. Rosendahl, S. Creighton, and I. J. Burgess, “Spatial mapping of methanol oxidation activity on a monolithic variable-composition ptni alloy using synchrotron infrared microspectroscopy,” *The Journal of Physical Chemistry C*, vol. 120, no. 41, pp. 23640–23647, 2016.

[152] B. Unni and I. J. Burgess, “Electrochemical and surface enhanced infrared absorption spectroscopy studies of tempo self-assembled monolayers,” *Electrochimica Acta*, vol. 381, p. 138263, 2021.

[153] L. A. Kotorlenko, V. S. Aleksandrova, and S. A. Samoilenko, “Calculation and interpretation of the vibrational spectrum of 2,2,6,6-tetramethyl-1-oxylpiperidine,” *Journal of Applied Spectroscopy*, vol. 31, no. 5, pp. 1395–1399, 1979.

[154] L. Rintoul, A. Micallef, and S. Bottle, “The vibrational group frequency of the N–O stretching band of nitroxide stable free radicals,” *Spectrochimica Acta Part A: Molecular and Biomolecular Spectroscopy*, vol. 70, no. 4, pp. 713–717, 2008.

[155] M. C. R. Symons and A. S. Pena-Nuñez, “Solvation of nitroxides,” *Journal of the Chemical Society, Faraday Transactions 1: Physical Chemistry in Condensed Phases*, vol. 81, no. 10, pp. 2421–2435, 1985.

[156] S. Stefan, F. Belaj, T. Madl, and R. Pietschnig, “A Radical Approach to Hydroxylaminotrichlorosilanes: Synthesis, Reactivity, and Crystal Structure of TEMPO-SiCl3 (TEMPO = 2,2,6,6-Tetramethylpiperidine-N-oxyl),” *European Journal of Inorganic Chemistry*, vol. 2010, no. 2, pp. 289–297, 2010.

[157] U. Zhumaev, A. Lai, I. Pobelov, A. Kuzume, A. Rudnev, and T. Wandlowski, “Quantifying perchlorate adsorption on au(111) electrodes,” *Electrochimica Acta*, vol. 146, pp. 112–118, 2014.

[158] N. Garcia-Araez, C. L. Brosseau, P. Rodriguez, and J. Lipkowski, “Layer-by-layer PMIRRAS characterization of DMPC bilayers deposited on a Au(111) electrode surface,” *Langmuir*, vol. 22, no. 25, pp. 10365–10371, 2006.

[159] M. R. Anderson, M. N. Evaniak, and M. Zhang, “Influence of solvent on the interfacial structure of self-assembled alkanethiol monolayers,” *Langmuir*, vol. 12, no. 10, pp. 2327–2331, 1996.

[160] R. G. Nuzzo, L. H. Dubois, and D. L. Allara, “Fundamental studies of microscopic wetting on organic surfaces. 1. formation and structural characterization of a self-consistent series of polyfunctional organic monolayers,” *Journal of the American Chemical Society*, vol. 112, no. 2, pp. 558–569, 1990.

[161] N. A. Giffin, M. Makramalla, A. D. Hendsbee, K. N. Robertson, C. Sherren, C. C. Pye, J. D. Masuda, and J. A. Clyburne, “Anhydrous tempo-h: reactions of a good hydrogen atom donor with low-valent carbon centres,” *Organic & biomolecular chemistry*, vol. 9, no. 10, pp. 3672–3680, 2011.

[162] C. Buhrmester, L. Moshurchak, R. Wang, and J. Dahn, “The use of 2, 2, 6, 6-tetramethylpiperinyl-oxides and derivatives for redox shuttle additives in li-ion cells,” *Journal of the Electrochemical Society*, vol. 153, no. 10, p. A1800, 2006.

[163] R. Wang, C. Buhrmester, and J. Dahn, “Calculations of oxidation potentials of redox shuttle additives for Li-ion cells,” *Journal of the Electrochemical Society*, vol. 153, no. 2, p. A445, 2006.

[164] K.-i. Ataka, T. Yotsuyanagi, and M. Osawa, “Potential-dependent reorientation of water molecules at an electrode/electrolyte interface studied by surface-enhanced infrared absorption spectroscopy,” *The Journal of Physical Chemistry*, vol. 100, no. 25, pp. 10664–10672, 1996.

[165] T. Uchida, M. Osawa, and J. Lipkowski, "Seiras studies of water structure at the gold electrode surface in the presence of supported lipid bilayer," *Journal of Electroanalytical Chemistry*, vol. 716, pp. 112–119, 2014.

[166] C. Gautier, O. Alévêque, F. Seladji, M. Dias, T. Breton, and E. Levillain, "Nitroxyl radical self assembled monolayers: Ion pairing investigation in organic and aqueous media," *Electrochemistry communications*, vol. 12, no. 1, pp. 79–82, 2010.

[167] E. Katz and I. Willner, "Kinetic separation of amperometric responses of composite redox-active monolayers assembled onto au electrodes: Implications to the monolayers' structure and composition," *Langmuir*, vol. 13, no. 13, pp. 3364–3373, 1997.

[168] N. Nerngchamnong, D. Thompson, L. Cao, L. Yuan, L. Jiang, M. Roemer, and C. A. Nijhuis, "Nonideal electrochemical behavior of ferrocenyl–alkanethiolate sams maps the microenvironment of the redox unit," *The Journal of Physical Chemistry C*, vol. 119, no. 38, pp. 21978–21991, 2015.

[169] H. Tian, Y. Dai, H. Shao, and H.-Z. Yu, "Modulated intermolecular interactions in ferrocenylalkanethiolate self-assembled monolayers on gold," *The Journal of Physical Chemistry C*, vol. 117, no. 2, pp. 1006–1012, 2013.

[170] I. R. Andvaag, T. A. Morhart, O. J. Clarke, and I. J. Burgess, "Hybrid gold–conductive metal oxide films for attenuated total reflectance surface enhanced infrared absorption spectroscopy," *ACS Applied Nano Materials*, vol. 2, no. 3, pp. 1274–1284, 2019.

[171] T. A. Morhart, K. Tu, S. T. Read, S. M. Rosendahl, G. Wells, S. Achenbach, and I. J. Burgess, "Surface enhanced infrared spectroelectrochemistry using a microband electrode," *Canadian Journal of Chemistry*, vol. 99, no. 999, pp. 1–5, 2022.

[172] E. Lins, S. Read, B. Unni, S. M. Rosendahl, and I. J. Burgess, "Microsecond resolved infrared spectroelectrochemistry using dual frequency comb ir lasers," *Analytical Chemistry*, vol. 92, no. 9, pp. 6241–6244, 2020.

Appendix A

Derivation of the peak potential of cyclic voltammogram

At equilibrium condition, the Nernst equation for electrode potential is

$$E = E^{0'} + \frac{RT}{nF} \ln \frac{\Gamma_{Oxd}}{\Gamma_{Red}} \tag{A.1}$$

where $E^{0'}$ and Γ are formal potential and surface concentration (mol/cm^2) respectively. The measured current with respect to the change in concentration of oxidized species Γ_{Oxd} is:

$$i = -nFA \left[\frac{d\Gamma_{Oxd}(t)}{dt} \right] \tag{A.2}$$

$$\Gamma_{Oxd}(t) = \Gamma^*_{Oxd} \left\{ 1 - \left[1 + \exp\left(\frac{nF}{RT}(E - E^{0'}) \right) \right]^{-1} \right\} \tag{A.3}$$

Substituting the derivative of above equation A.3 in equation A.2, and rewriting $-\left(\frac{dE}{dt}\right)$ as the potential sweep rate υ, the expression for current as :

$$i = \frac{n^2F^2\upsilon A\Gamma^*_{Oxd}}{RT} \frac{\exp\left(\frac{nF}{RT}(E - E^{0'})\right)}{\left\{1 + \exp\left(\frac{nF}{RT}(E - E^{0'})\right)\right\}^2} \tag{A.4}$$

The potential at which current reaches the peak is , $E = E^{0'}$ then the above equation A.4 will be,

$$i_p = \frac{n^2F^2\upsilon A\Gamma^*_{Oxd}}{4RT} \tag{A.5}$$

Appendix B

Synthesis of TEMPO$^+$

Hypochlorous acid oxidizes TEMP$\dot{O}$ to oxoammonium cation (TEMPO$^+$). The pK_a value of hypochlorous acid is 7.5. At pH $>$ pK_a, hypohalous acids exist mostly as hypohalate, which is inactive for the oxidation of TEMP$\dot{O}$. The oxidation reaction is monitored using UV spectra (Figure B.1), with water as baseline. The dotted line shows the absorption by free radical form of TEMPO at 240 nm. As the reaction progress, the peak at 240 nm goes down and absorption peak corresponding to TEMPO$^+$ at 290 nm grows up. The absorption peak of HOCl at around 300 nm overlaps with the TEMPO$^+$ peak.

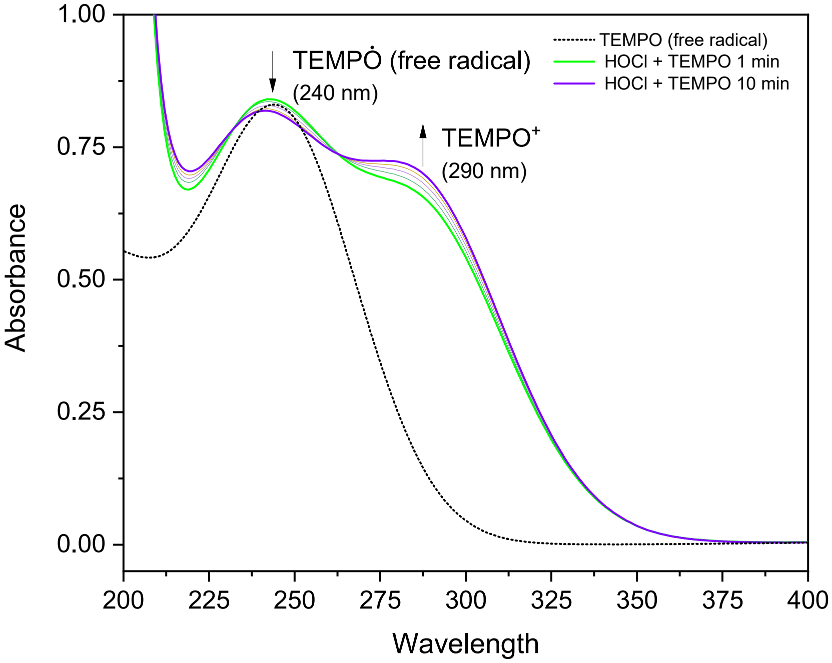

Figure B.1: UV spectra of oxidation of TEMP$\dot{O}$ using hypohalous acids (HOCl)